Three-dimensional convective velocity fields in the solar photosphere

3

Takayoshi OBA

Doctor of Philosophy

Department of Space and Astronautical Science,

School of Physical sciences,

SOKENDAI (The Graduate University for Advanced Studies)

Abstract

The solar photosphere is well-defined as the solar surface layer, covered by enormous number of bright rice-grain-like spot called *granule* and the surrounding dark lane called *intergranular lane*, which is a visible manifestation of convection.

A simple scenario of the granulation is as follows. Hot gas parcel rises to the surface owing to an upward buoyant force and forms a bright granule. The parcel decreases its temperature through the radiation emitted to the space and its density increases to satisfy the pressure balance with the surrounding. The resulting negative buoyant force works on the parcel to return back into the subsurface, forming a dark intergranular lane. The enormous amount of the kinetic energy deposited in the granulation is responsible for various kinds of astrophysical phenomena, e.g., heating the outer atmospheres (*the chromosphere* and *the corona*). To disentangle such granulation-driven phenomena, an essential step is to understand the three-dimensional convective structure by improving our current understanding, such as the above-mentioned simple scenario.

Unfortunately, our current observational access is severely limited and is far from that objective, leaving open questions related to vertical and horizontal flows in the granulation, respectively. The first issue is several discrepancies in the vertical flows derived from the observation and numerical simulation. Past observational studies reported a typical magnitude relation, e.g., stronger upflow and weaker downflow, with typical amplitude of ≈ 1 km/s. This stronger upflow trend is opposite to that in numerical simulations, in which downflow is stronger than upflow imposed by gravitational attraction and gas pressure gradients, with much higher amplitude. The second issue is that, while determining the amplitude of the horizontal flow is a key element on this work, this amplitude is severely hindered. The energy injection from the photosphere into the corona depends strongly on this amplitude. While preexisting numerical models successfully reproduce the hot corona by adopting amplitude of typically 1 km/s, previous observational works reported a few hundred m/s.

For tackling those two questions, attaining high spatial resolution is a key success. Insufficient resolution blends the signals from granules and intergranular lanes each other, which makes preferentially narrow downflow signals canceled with upflow ones. The required spatial resolution is even demanding for a derivation of the horizontal flows. Their Doppler signals can be recorded at the solar limb, where the line-of-sight (LOS) of an observer is aligned with the horizontal direction to the solar surface. Any solar limb observations are subjected grossly to the spatial degradation effect, namely *the foreshortening effect*: an object's length along the LOS direction becomes shorter than the actual length as observer's angle inclines to the plane of the solar surface.

Unfortunately, the resolution performance of the current observational instruments is still insufficient for this purpose, even with the *Hinode* spacecraft, which has the highest spatial resolution among the current space-borne telescopes. The author challenges to improve the image quality by developing a deconvolution technique, which is a compensation method for optical distortion, diffraction, and scattering of light in an imaging instrument. While conventional deconvolution techniques have a problem in amplifying the noise signal, our deconvolution technique adopts a regularization term designated to suppress the noise amplification. Through a verification work with a synthesized granulation image, our deconvolution technique is confirmed to retrieve a non-degraded image by successfully avoiding the noise enhancement. This study uses spectral data provided by the *Hinode* satellite, and its data quality is improved by our deconvolution technique. The examined dataset covers almost all the angles from the solar disk to the limb (e.g., 0°-83° in the solar latitude) so that we reasonably diagnose the horizontal flow with multiple LOS angles to the granulation.

We summarize separately the scientific results of the vertical and horizontal flows.

(i) Vertical flows

Our deconvolution provides a tiny scale of intergranular downflowing distribution. Up-

flows in the edge of each granule transform to downflows. Regarding downflows, we detect two different phenomena: pre-existent intergranular lanes become generally wider, occupying larger areas, but also narrow intergranular lanes, hindered by the scattered light contamination, newly appear. The LOS velocity ranges from -3.0 km/s (upward) to +3.0 km/s (downward) after the deconvolution processing while it does from -2.0 km/s to +1.5 km/s before it. The downflow amplitude is more enhanced than upflow one. This is because the deconvolution processing reasonably corrects for a preferential cancellation of Doppler signals in darker intergranular lanes. Thus, deconvolution changes the magnitude relation from stronger upflow and weaker downflow to almost comparable. These characteristics, i.e., up- and downflow magnitude relation and their amplitude after deconvolution, match closer those derived from numerical simulations. Therefore, correcting the instrumental scattered light contamination produces data that is in agreement with those predicted by numerical simulations.

(ii) Horizontal flows

Our deconvolution technique relaxes the foreshortening degradation, providing accessible solar latitude from the purely vertical (to an observer) of 0° onto an oblique of 53°. In root-mean-squared (RMS) amplitude, the measured LOS velocity monotonically increases from 0.9 km/s to 1.6 km/s along the latitude of 0° to 53°. A horizontal flow of 1.6 - 1.9 km/s in RMS matches the mentioned amplitude variation, which is two or three times larger than those reported before. Our amplitude exceeds theoretically required value in all the preexisting coronal heating models for reaching the typical coronal temperature (e.g., one million degree).

(iii) Three-dimensional convective velocity field

The granulation generally represents a radial divergent flow from a granular center, and small parts of the flow streams along the azimuthal direction. From the three-dimensional

convective flow structure, derived with deconvolution, we discover the fastest horizontal flow in intergranular lane. While our conventional understanding regarded intergranular lanes as simply downflowing region, this study suggests that the horizontal flow, initially accelerated from the center of granular cells, moves outwards until it reaches intergranular lanes.

Our deconvolution technique makes it possible to describe the solar surface convection with unprecedented high data quality. Consequently, this study remarkably pushed forward our understanding of not only the granulation but also the granulation-driven phenomena pervading the sun.

Acknowledgement

partner, NASA and STFC (UK) as international partners. Scientific operation of the *Hinode* mission is conducted by the *Hinode* science team organized at ISAS/JAXA. This team mainly consists of scientists from institutes in the partner countries. Support for the post-launch operation is provided by JAXA and NAOJ (Japan), STFC (U.K.), NASA, ESA, and NSC (Norway).

Contents

Chapter 1

Introduction

The sun is the most prominent astronomical object of the solar system, one that plays a central role in our lives. This object is astronomically unique in its close distance to us, providing a spatially well-resolved feature. The sun contains various kinds of energy transfer mechanisms, which divides the whole structure to several layers. *The photosphere* is defined as the solar surface layer (Fig.1.1), where enormous energy is released with mainly visible light and infrared emission to the space. Its energy source originates from the inner part. The solar core creates the energy through a nuclear fusion consuming hydrogen that is the vast majority of the solar chemical composition. Just outside the solar core is *the radiative zone*, where light carries the energy toward the farther outer layers. The remaining outer part of the sun is *the convection zone*, where the material's movement toward the surface carries the energy. The temperature at the photosphere reaches $\approx 6 \times 10^3$ K. The outer atmospheric layers, called *the chromosphere* and *the corona*, reach $\approx 10^4$ K and $\approx 10^6$ K, respectively. The solar photospheric layer is the scene of energy transition from kinetic energy to other forms toward the outer atmospheric layers and interstellar space.

1.1 Overview of the solar photosphere

The photosphere is the solar surface observed with the visible light. Here the surface is defined as a geometrical height of 0 km, where the optical depth at a visible wavelength of $\lambda = 500$ nm equals unity (Stix 2004). Ones can see the cellular patterns with moderate-size telescopes (more than 20 cm) and a large part of the surface is covered by numerous bright granular features, except in *sunspots* where highly intense magnetic field. These bright cells are called *granules*, which are surrounded by dark channels called *intergranular lanes* (Fig.1.2). The typical size of granules is $1.''0$ (≈ 700 km), and the width of intergranular lanes is $0.''3$ (≈ 200 km). Many of spectral data recording the Doppler shift reveals the rough sense of *upflows in granules and downflows in intergranular lanes* (Nesis et al. 2001; Puschmann et al. 2003).

The convection is responsible for this cellular pattern. The photospheric layer is *con-*
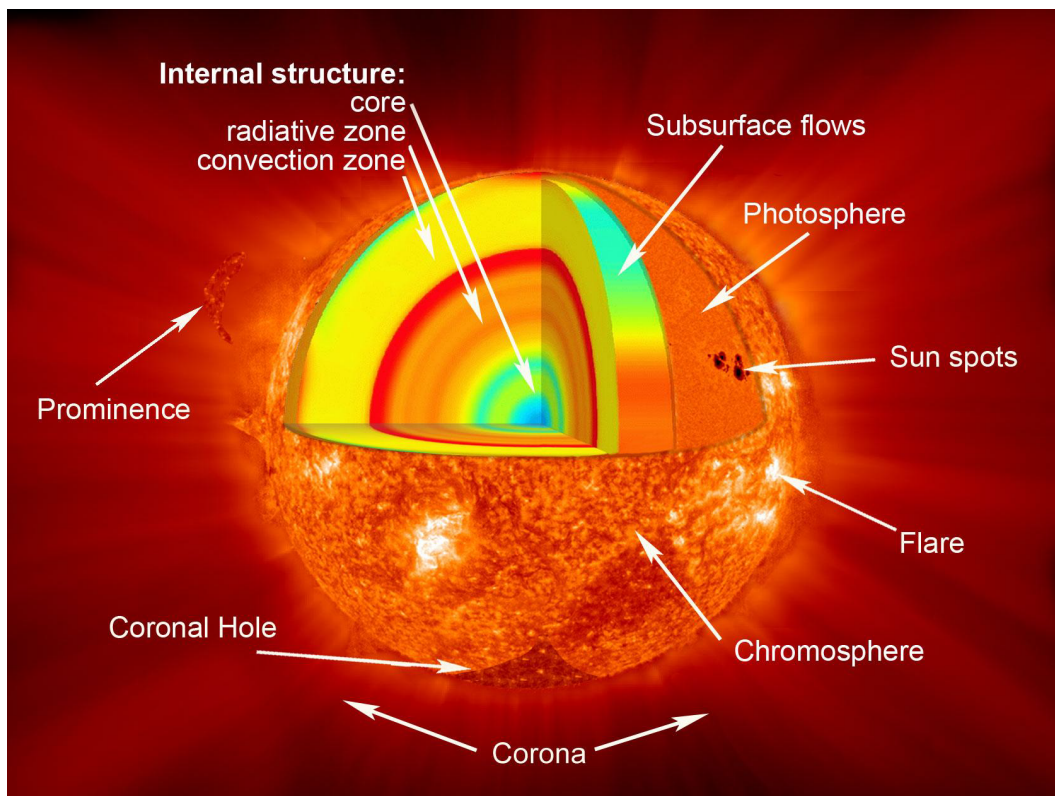
Figure 1.1: Illustration of the solar structure from NASA.

vective stable, whereas the subsurface is *convectively unstable* (Unsöld 1930). A steep atmospheric temperature gradient yields this instability; when perturbed gas parcel is lifted up adiabatically from its equilibrium, its density will be smaller than the new environment, subsequently upward buoyant force works on the parcel (Schwarzschild 1906). The transition of the ionized state is likely to make a convective unstable stratification via its latent heat. One thousand km below the solar surface, a majority of hydrogen transit from ionized to neutral state, causing a vigorous convection with the corresponding scale. Penetrating to the photosphere, the material becomes transparent and releases effectively their internal energy through radiative loss due to a deficient radiative-absorber (H^-) associated with the material's temperature decreasing (Mihalas 1978). This radiative energy loss drops material's temperature and makes high dense state, and subsequently negative buoyant force pulls down the material, turning its traveling direction from upward to downward (Stein & Nordlund 1998). This material continues to experience such a negative buoyant force associated with a radiative energy release, finally submerging into intergranular lanes, as this consecutive scenario is seen in Fig.1.3.

While that simple granulation scenario has been widely accepted, the actual phenomenon cannot be described well by this scenario (Bray et al. 2009). Granules are far from being static because they repeat birth/death as a consequence of three processes, namely fragmentation, disappearance and merging (Hirzberger et al. 1999a; Poetzi et al. 2000; Müller et al. 2001) within a typical lifetime of 6-12 minutes (Title et al. 1986; Dialetis et al. 1986; Del Moro 2004). The size of granule affects their properties of intensity, velocity field and lifetime; these parameters linearly increase with the granular size but only for a size of less than $\approx 1.''4$, while even larger granules violate this relation (Hirzberger et al. 1997; Yu et al. 2011b; Abramenko et al. 2012; Lemmerer et al. 2017). The most dynamical phenomenon in the granulation, *exploding granule*, occasionally pushes their surrounding vigorously by disintegrating themselves into a number of segments (Title et al. 1986; Rieutord et al. 2000; Hirzberger et al. 1999b). Some bright
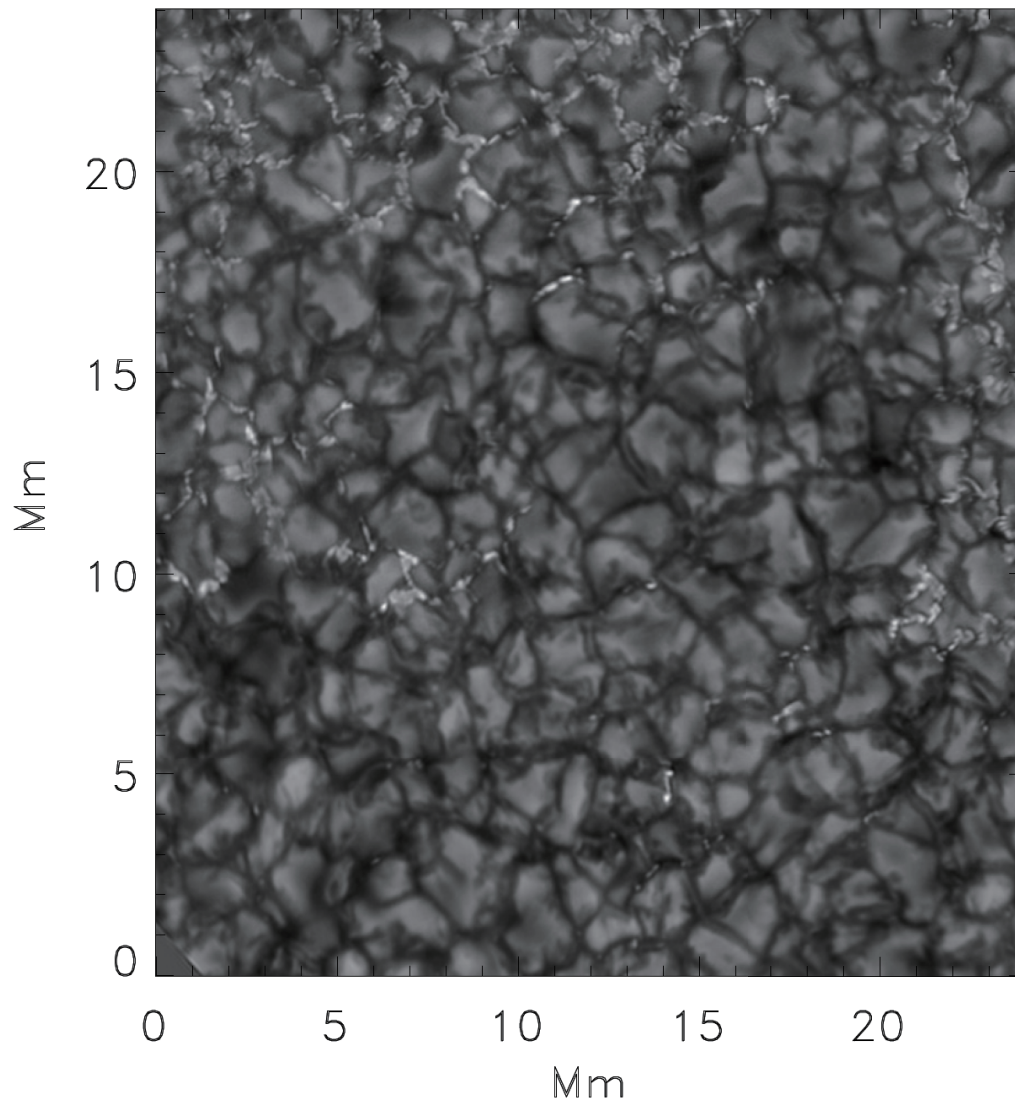
Figure 1.2: Image of granulation in the G-band continuum, showing bright rising fluid surrounded by darker intergranular lanes (image from the Swedish 1m Solar Telescope and Institute of Theoretical Astrophysics, Oslo; Nordlund et al. 2009).

Convective flow

Granule   Intergranular lane
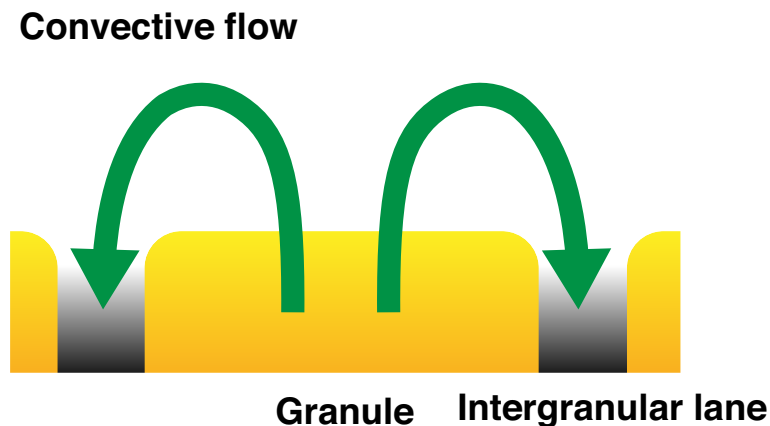
Figure 1.3: Schematic view of the granulation. Hot gas material ascends to the photosphere, making a bright granule as shown in the center. This material temperature decreases through radiative energy loss and its density increases, and the resulting negative buoyant force changes the vertical traveling direction of the gas flowing from upward to downward. It subsequently descents to the subsurface, forming a dark intergranular lanes in the edge.

lanes are seen inside granules, which is a visible signature of vortices (Steiner et al. 2010). The existence of supersonic flows has been reported (Solanki et al. 1996; Nesis et al. 1993; Bellot Rubio 2009; Quintero Noda et al. 2016). The landscape at upper photospheric layers is completely different, with *dark* granules surrounded by *bright* intergranular lanes. This opposite intensity pattern was labeled as *reverse granulation*. This phenomenon requires some sort of energy injection to brighten the upper intergranular lanes (Rutten & Krijger 2003; Rutten et al. 2004; Leenaarts & Wedemeyer-Böhm 2005). While the hydrodynamic process drives such photospheric phenomena, magneto-convective process provides more various types of phenomena. Bellot Rubio et al. (2001) and Fischer et al. (2009) reported that the convective flows intensify the magnetic fields strength. The physical interaction between magnetic and kinetic energy extensively affects the upper layers, i.e., the chromosphere and corona, because some of magnetic flux tubes extend toward those layers. Several numerical simulations put magnetic flux tubes in the reproduced granulation, and they intermittently drove magnetohydrodynamic waves (MHD waves)

propagating upward; the compressible form of the waves is excited by the surrounding convective downward flows (Steiner et al. 1998; Kato et al. 2011, 2016), and incompressible form is done by the surrounding horizontal flow (Vögler et al. 2005; Isobe et al. 2008). Those phenomena have been believed to be a key process of how the corona and chromosphere maintain their high temperature (Withbroe & Noyes 1977). The possibility of the existence of the MHD waves has inspired many solar physicists to directly capture an observational proof; Fujimura & Tsuneta (2009) and Martínez Pillet et al. (2011) reported MHD waves being in the photosphere, and the propagating MHD waves found in the chromosphere (De Pontieu et al. 2007; Okamoto et al. 2007; Jess et al. 2009) and in the corona (Tomczyk et al. 2007).

Beyond the solar physics, the photospheric investigation cultivates our better understanding for the stellar convection (Gray 2008). Any information about the stellar photosphere is highly limited, i.e., it can provide only spatially averaged spectral profiles. Several authors Bellot Rubio et al. 1999; Frutiger et al. 2000; Borrero & Bellot Rubio 2002 have tried to develop a technique to determine the stellar chemical composition, performing a verification work in the solar observation,

As described in this chapter, the granulation drives the energy transfer among the kinetic, radiative and magnetic forms, leading to various kinds of astronomical phenomena. Such phenomena ubiquitously pervade the solar and stellar surface, and extensively even the upper layers, i.e., the chromosphere and the corona.

1.2 Observational understanding about the granulation

Many authors have dedicated their efforts to advance our observational understanding for the granulation. Here we review the convective flows along *vertical* and *horizontal* directions to the solar surface separately, because the observational approaches to derive these quantities are quite different.

1.2.1 Vertical flows of the solar granulation

The vertical flow has been better investigated than horizontal one because the derivation of this quantity is easier. We may calculate the Doppler shifts in spectral profiles observed at the solar disk center, where the line-of-sight (LOS) of an observer is aligned with the vertical direction to the solar surface. Using ground based telescopes, many authors found that the maximum amplitude of the vertical flows are less than or comparable to 1 km/s; they always indicate a typical magnitude relation of faster upflows and slower downflows, as Berrilli et al. (1999), Nesis et al. (2001), Hirzberger (2002), and Janssen & Cauzzi (2006) reported peak-to-peak amplitudes of -0.9 km/s to +0.6 km/s, -1.2 km/s to +0.9 km/s, -1.4 km/s to +1.4 km/s, -1.2 km/s to +0.9 km/s, respectively, from now on sign of velocity fields identifies upward with *negative* and downward with *positive*. On the precise derivation of the Doppler signals, the spectral data should maintain sufficient wavelength sampling with high signal-to-noise by binning its spatial sampling moderately. As the telescope aperture increases, simultaneously providing better wavelength and spatial resolution, faster vertical flow speeds have been reported. Addressing both requirements, the recently launched spacecraft *Hinode* (Kosugi et al. 2007) provides the excellent spectral data with a perfect lack of the atmospheric seeing degradation. The solar optical telescope (SOT) aboard *Hinode* has a 50cm telescope, attaining a diffraction limit of 0.″3 at the wavelength of 630 nm (Tsuneta et al. 2008). Several authors have investigated the Doppler signals using this space-borne telescope, finding much larger amplitude than the previously reported values. Jin et al. (2009) and Yu et al. (2011a) found the peak-to-peak amplitudes of -3.3 km/s to +2.0 km/s, and -2.0 km/s to less than +2.0 km/s, respectively.

One concern, however, exits for their analysis because their reported amplitudes include another-origin (not the convection-origin) velocity fields, namely the 5-min oscillations. This oscillation is an assembly of numerous numbers of eigenmodes made with the solar spherical stratification (Leighton et al. 1962). Their oscillatory velocity fields are found to be 0.3-0.4 km/s in root-mean-square (RMS) (Ulrich 1970), and their amplitude depends

on the spatial distribution, e.g., stronger in intergranular lanes and weaker in granules (Khomenko et al. 2001). The oscillatory motions are amplified with increasing height due to less density in accordance with the kinetic energy of the sound waves preserved (Deubner 1974), even attaining higher amplitude than the convection a few hundred km above the surface. Using a ground based telescope, Kostik & Khomenko (2007) carefully removed the oscillatory component and found average flow speeds of 0.2 km/s for both up- and downflows. Removing the 5-min oscillations, Oba et al. (2017) used the *Hinode*'s spectral data and found the height structure of average flow speed, in which upflows (-0.6 km/s) decelerate toward the higher layer and downflows (+0.4 km/s) accelerate toward the lower layer. Clearly seen from the observational past works, the higher spatial resolution still improves vertical velocity fields, implying that even the resolution of the state-of-the-art instrument *Hinode* would be insufficient.

In summary of the observational review about the vertical flows, several authors have typically shown stronger upflows and weaker downflows with peak-to-peak values of $\approx$ 1 km/s, but higher spatial resolution still improves the amplitudes.

1.2.2   Horizontal flows of the solar granulation

The derivation of the horizontal convective flow is trickier than the vertical one. Their Doppler signals can be observed at the solar limb, where the LOS of an observer is aligned with the horizontal direction to the solar surface (Beckers & Nelson 1978; Balthasar 1985; Baran & Stodilka 2010). Keil & Canfield (1978), Mattig et al. (1981), and Nesis & Mattig (1989) found that amplitude of the horizontal flow is two times larger than that of the vertical one. Ichimoto et al. (1989) and Ruiz Cobo et al. (1996) depicted the height structure of the vertical and horizontal flow fields, the latter value is indirectly derived from the vertical flow amplitude in accordance with mass flux balance held, i.e., div(ρv)=0. It should be emphasized here that, however, any solar limb observations are subjected grossly to

the spatial degradation effect, namely *the foreshortening effect.* This effect causes an image reduction because an object's length along the LOS becomes shorter than the actual length as observer's angle inclines to the plane of the solar surface. Hence, resolving the granular and intergranular spatial pattern is more difficult, because insufficient spatial resolution causes a worse image degradation at the limb than the disk center.

One alternative approach is a *feature tracking technique.* This technique bases on cross-correlation within two or more successive images, i.e., no need to measure a Doppler shift, and computes the relative displacement of granules. In the last decades, this technique has been widely accepted instead of the straightforward Doppler calculation approach, while this technique works well when the traveling fluid does not significantly change its distinctive shape itself. Fortunately, this tracking technique merely requires a constant quality in the successive images, which is largely achieved by the recent observational instruments thanks to the advent of space-borne telescopes, and the ground-based telescopes with an aid of the image correction treatments for atmospheric seeing, e.g., *adaptive optics* (Rimmele 2000) or/and *phase diversity method* (van Noort et al. 2005). The resulting speeds of the apparent motion are found to be 0.8 - 1.3 km/s in RMS (Berger et al. 1998; Matsumoto & Kitai 2010; Keys et al. 2011; Manso Sainz et al. 2011; Chitta et al. 2012).

In summary of the review about the horizontal flows, their derivation is tricky because the limb observation is necessarily although the foreshortening effect causes even worse image degradation. In last decades, the tracking technique has been widely used by measuring proper motions in consecutive granulation images, although it merely tracks apparent movement of granules.

1.3 Theoretical understanding about the granulation

Numerical simulation technique can provide opportunities to reasonably explain the reported mysterious phenomena. Many authors have been developed this profitable tool

remarkably enough to reproduce the granulation without a noticeable departure from the real one in their appearance (see Fig.1.4), actually pushing forward our understanding (Hurlburt et al. 1984; Stein & Nordlund 1998; Gadun et al. 2000). Some of the phenomena introduced in the section 1.1 are interpreted with a help of the numerical simulation's approach. Recent numerical simulations introduce a 3-dimensional scheme of radiative-MHD (RMHD) as gases vigorously exchange their internal energy with its surrounding via radiation.
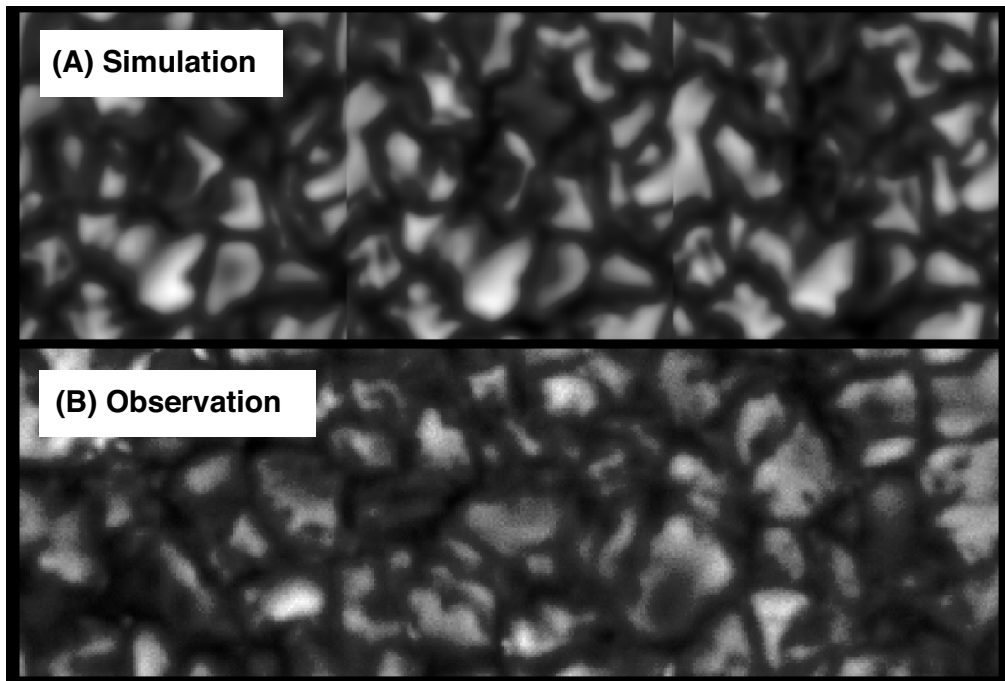
Figure 1.4: Comparison of granulation as seen in the emergent intensity. (A) from the simulations. (B) as observed by the Swedish Vacuum Solar Telescope on La Palma. The top row shows three simulation images at 1-minute intervals (Stein & Nordlund 1998).

Several authors have developed many types of the RMHD simulation codes, e.g., STAG-GER (Galsgaard & Nordlund 1996), MURaM (Vögler et al. 2005), CO^{5}BOLD (Freytag et al. 2002), BIFROST (Gudiksen et al. 2011), and ANTARES (Muthsam et al. 2010). Simulated granulations typically indicate a magnitude relation of slower upflows and faster

downflows, as a peak-to-peak value represents roughly -6.0 km/s to + 8.0 km/s (Stein & Nordlund 1998). This magnitude relation of up- and downflow is opposite to the observational result, and theoretical amplitude remarkably exceeds the observational one. That magnitude relation is naturally governed by pressure excess in centers of granules to break the ascending flow and in intergranular lanes to enforce the descending one (Hurlburt et al. 1984; Bray et al. 2009). Radiative energy loss promotes such a density enhancement and negative buoyancy oriented to downward, leading to faster donwflows. An additional characteristic is that the speed of horizontal flows is larger than that of vertical motions when the radiative energy loss makes a strongly stratified atmosphere (i.e., low density scale height) in granules, which sweeps the upwelling gas into the horizontal directions (Nordlund et al. 2009). Those granulation characteristics are common among the developed simulation codes; Beeck et al. (2012) confirmed the amplitude difference being within ≈10% in STAGGER, MURaM, CO^{5}BOLD codes, e.g., 1.8 - 2.0 km/s for vertical flow and 3.3 - 3.6 km/s for horizontal one in RMS, at a geometrical height of 100 km.

Simulated granulations have been applied to the various kinds of the photospheric phenomena, e.g., supersonic flows by Vitas et al. (2011), reversed granulation by Cheung et al. (2007), exploding granules by Rast (1995), and granular various size-dependent properties (e.g., lifetime and emergent intensity) by Lemmerer et al. (2014). Several authors have attempted to understand the magneto-convective phenomena, e.g., sunspots by Rempel et al. (2009) and the MHD waves by Isobe et al. (2008). These codes are applicable not only to the solar phenomena but also to the stellar photosphere, adopting observationally-known atmospheric parameters of stars to reproduce their own granulations (Asplund et al. 2000; Ramírez et al. 2009; Beeck et al. 2013; Magic et al. 2013; Nieminen 2017).

As clearly seen throughout this section, several studies have developed a number of numerical simulation codes, and progress our comprehension of the granulation. The developed codes represent the almost identical velocity fields, which is good for cross-

validation with respect to each other. This fact supports that numerical simulation has a theoretical consensus view for the granulation, while the synthesized granulations depart from the observation in the flow amplitudes and the magnitude relation of up- and down-flows.

1.4 Issues

The photospheric convection is obviously responsible for many kinds of physical phenomena, as introduced in section 1.1. However, our current knowledge described in section 1.2 is still far from being well proceeded enough to understand the convection. We are largely lack of the spatial distribution of the horizontal flow, in contrast to a better understanding of that of the vertical flow, i.e., upflowing granules and downflowing intergranular lanes. Particular interest is horizontal flow in intergranular lanes, where many of magnetic flux tubes preferentially pervade; the lateral convective flows can input their kinetic energy into magnetic flux tubes, which is widely believed to transfer the stored energy into the upper layers, e.g., the chromosphere and the corona. We may consider therefore that a description work of the three-dimensional flow fields is greatly beneficial to not only comprehend the granulation, but also identify the spatial distribution of kinetic energy input in the granulation.

Unfortunately, the current observational access is severely limited, and insufficient our knowledge leaves open questions. First of all, while the determination of horizontal flow amplitude is an urgently needed work, this value is still severely veiled. The efficiency of the energy dissipation in the corona is highly dependent on the photospheric lateral buffeting flow amplitude; stronger amplitude of MHD waves is expected to cause an efficient non-linearization in the corona, playing a role of dissipation process. Several authors differently propose regimes of dissipation mechanism, namely a mode-coupling process (Kudoh & Shibata 1999; Moriyasu et al. 2004; Suzuki & Inutsuka 2006; Antolin

et al. 2008) and a turbulence process (van Ballegooijen et al. 2011; Asgari-Targhi & van Ballegooijen 2012; Woolsey & Cranmer 2015). Their numerical models set photospheric buffeting motion as a boundary condition, and realize the coronal temperature with amplitude of more than ≈ 1 km/s adopted. Thus, one of the important observational works is to properly determine the amplitude of the horizontal flow.

However, the past observational approaches have not satisfactory determined them. The Doppler calculation approach severely suffers from the foreshortening degradation, showing amplitude of merely a few hundred m/s (see section 1.2.2). Alternatively, to avoid this degradation associated with the limb observation, the feature tracking technique has been widely accepted instead. Rieutord et al. (2001) and Matloch et al. (2010) warned this technique's limitation imposed by its inherent nature; it can characterize intensity fluctuation in consecutive images and trace only net result of the flowing, which is not the same as the underlying gas motions. To estimate the limitation of this technique, several authors (Verma et al. 2013; Yelles Chaouche et al. 2014; Louis et al. 2015) applied the tracking technique to consecutive images of the granulation synthesized by the numerical simulation code for a direct comparison between *real* horizontal velocity fields and output retrieved by the technique. Their deviations particularly occur in intergranular lanes (Louis et al. 2015), since this technique can characterize only distinctive signature (i.e., the rounded shape of granule). Verma et al. (2013) pointed out that the technique is generally not sensitive to a spatial scale being less than 800 km, which makes it almost impossible to track any horizontal flows in narrow intergranular scale of 200 km ($\approx 0.''3$). The resulting flow fields are smaller than the real ones by a factor of three (Verma et al. 2013), and those kinetic energy is grossly underestimated by a factor of five-six (Yelles Chaouche et al. 2014). To make matter worse, many of the retrieved fields are not subjected to a simple linear relation with the real ones, i.e., vector of horizontal flows are different from each other, as seen in Fig.1.5. The feature tracking technique therefore provides a good proxy of horizontal flows in granular scale, but it cannot capture well
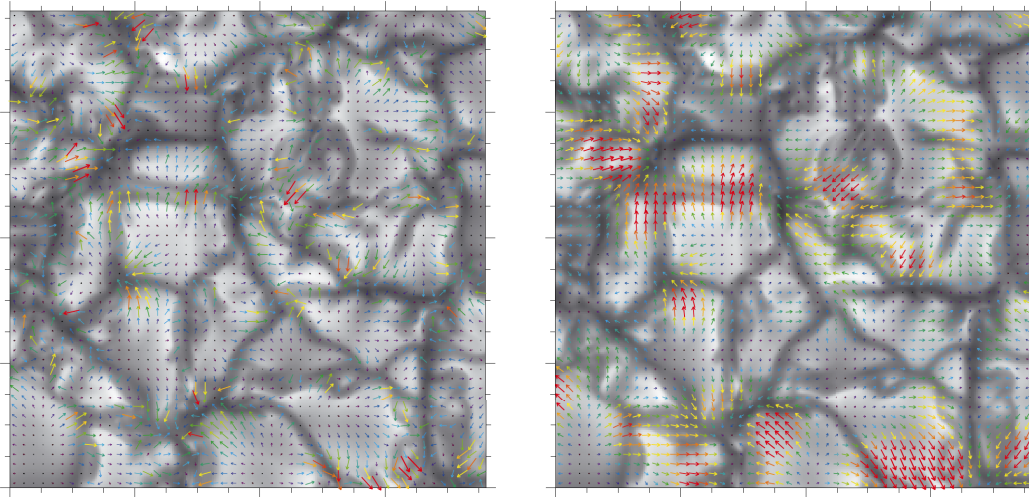
Figure 1.5: Gray-scale intensity image of the time series overploted with the actual flow vectors (left) and the outputs by the technique (right). The speed and direction of the flow field are given by rainbow-colored arrows, where dark blue corresponds to low and red to high velocities within the range of 0.75-7.5 km/s and 0.3-3.0 km/s for the actual and smoothed flow fields, respectively (Verma et al. 2013). This simulated numerical box has an extent of 7.64 Mm for both horizontal directions.

them in intergranular lane scale.

The limitation of the tracking technique prohibits further cultivating our understanding of the granulation. Even in the future with a growing spatial resolution, this limitation would not radically solved owing to its inherent nature, i.e, it is susceptible only to appearance of granule's movements.

The current situation forces us to reconsider an alternative way that is capable of deriving the horizontal flows in intergranular lanes as well as in granules. One possible solution is to return to a straightforward approach of Doppler calculation with spatially well-resolved spectral data. In contrast to the feature tracking technique, the Doppler calculation can diagnose equally granular and intergranular flows if the foreshortening degradation is largely relaxed by high spatial resolution.

Unfortunately, the current observational instruments cannot yet fulfill this demanding spatial resolution. This is a serious problem in studying the granulation even for the disk center observation without the foreshortening degradation. This concern is provoked by

discrepancies seen in vertical flows between the observation and numerical simulation in the past literature. Even with spectral data observed by *Hinode*, ones would find a characteristic magnitude relation of *stronger upflow and weaker downflow with a peak-to-peak amplitude of merely a few km/s*, as previously explained in section 1.2.1. This magnitude relation is opposite to the numerical simulations and the observational amplitudes are much smaller than those in the numerical simulations, as noted in section 1.3. One possible cause of this discrepancy is *an imaging performance* of the employed instrument; any optical instruments (e.g., primary mirror with secondary one's obscuration) scatter the incoming light over several pixels in the camera owing to the light property of diffraction. Aiming to know how the *Hinode*'s instrumental imaging performance degrades the image, Danilovic et al. (2008) carefully modeled its *point-spread function* (PSF) that shows a photon energy distribution on the CCD pixels from a single point source. They artificially blurred the continuum intensity image obtained by running the SPINOR spectral synthesis code (Frutiger et al. 2000) with the synthesized granulation produced by the MURaM code (Vögler et al. 2005), as shown in Fig.1.6. The imaging degradation reduced the intensity contrast in RMS from 14.4% to 7.5%, and the latter value is nearly the same as the observation (7.0%). This contrast difference of a factor of two suggests that the relation of the up- and downflows may also be significantly affected by the PSF of the *Hinode*/SP.

To sum up of this chapter, inadequate spatial resolution of the current observational instruments leaves two open questions related to both directions' flow: regarding the horizontal flow, the foreshortening degradation associated with any limb observations hinders our investigation of the amplitude and its spatial distribution; regarding the vertical flow, even without the foreshortening degradation, there is a large gap between observation and numerical simulations for their magnitude relation of up- and downflow, and also their amplitudes.
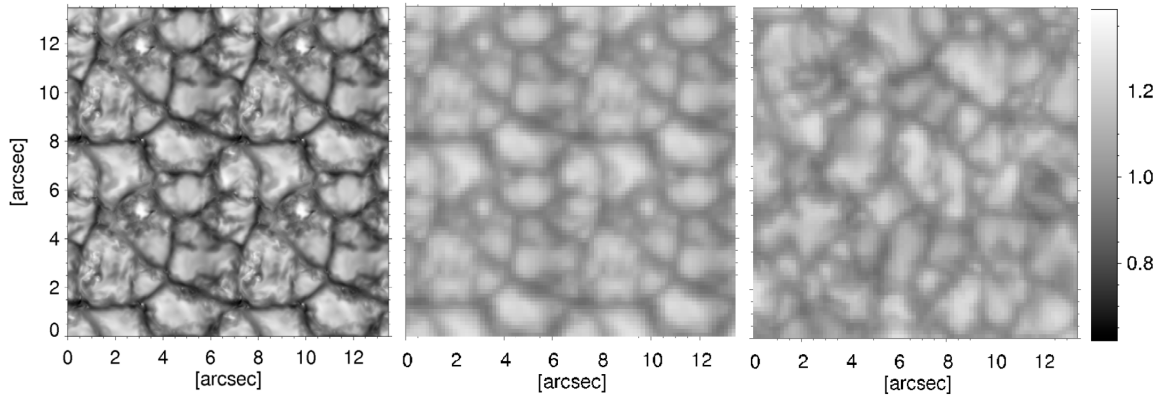
Figure 1.6: Continuum images at a wavelength of 630 nm from a simulated snapshot with original resolution (left) and after degradation (middle), in comparison with a detail of the observed *Hinode*/SP map of the same size (right)(Danilovic et al. 2008).

1.5   Motivation of this study

Observational difficulties for tackling the open questions (see section 1.4) are rooted in inadequate spatial resolution; it demands even beyond the current instrumental performance. We accordingly aim to remove the instrumental scattered light, which is one of the major concern of the image degradation, by performing a *deconvolution processing* that corrects for the instrumental imaging performance in the *Hinode* spectral data.

Recently, some of deconvolution processing have been applied to the *Hinode* data. This instrument is suited for such an image reconstruction technique because its PSF is well-known and almost time-independent. Early works (Mathew et al. 2009; Wedemeyer-Böhm & Rouppe van der Voort 2009) found that the intensity contrast of the granulation in RMS increases by a factor of two for any imaging filters aboard *Hinode* through their own deconvolution processing. A self-consistent approach was developed by van Noort (2012) and van Noort et al. (2013), who extended the SPINOR code to iteratively invert a set of spectropolarimetric profiles by simultaneously taking account of the influence of the PSF (Fig.1.7). This established inversion technique has been applied to investigate sunspot and its surrounding region (cf. Riethmüller et al. 2013; Tiwari et al. 2013; Buehler et al. 2015, etc.) and the other region with relatively low magnetic activity (Danilovic

et al. 2016). In contrast to this simultaneous handling of the inversion and deconvolution processing, Ruiz Cobo & Asensio Ramos (2013) and Quintero Noda et al. (2015, 2016) deconvolved spectropolarimetric data as a preprocessing and subsequently applies the SIR inversion code to the data (Ruiz Cobo & del Toro Iniesta 1992). The authors, in order to avoid the enhancement of noise produced by any deconvolution technique, used a filtering process before the deconvolution. To these established approaches (van Noort 2012; Ruiz Cobo & Asensio Ramos 2013), we try to use a simple alternate deconvolution technique that incorporates a noise suppression process into the conventional deconvolution algorithm.

Here we should emphasize our motivation and scientific goals. Our deconvolution technique is to realize a Doppler diagnostic approach to solve the open questions by correcting the instrumental scattered light. The first object is to reconcile the discrepancies between the observations and numerical simulations for their magnitude relation in up- and downflow, and their amplitudes. The second one is to determine the amplitude of horizontal flows by relaxing the foreshortening degradation. Finally, we aim to describe the three-dimensional structure of the granulation, combining the vertical and horizontal flow fields. Those works would be the first observational indication that Doppler calculation with high spatial resolution is a promising tool to investigate the physical properties of the granulation, replacing the current widespread use of the feature tracking technique.

This dissertation is organized as the following chapters. In chapter 2, we describe the overview of the *Hinode*, examined datasets, and data calibration. In chapter 3, we present the procedure to derive the height structure of the velocity fields, namely how to derive the LOS velocity fields, deconvolution technique, how to remove the 5-min oscillations, and how to estimate the horizontal convective velocity fields. In chapter 4, we show results of our analysis, showing the vertical and horizontal, and their height structure. In chapter 5, we discuss the retrieved velocity fields. In chapter 6, we summarize this study and future works.
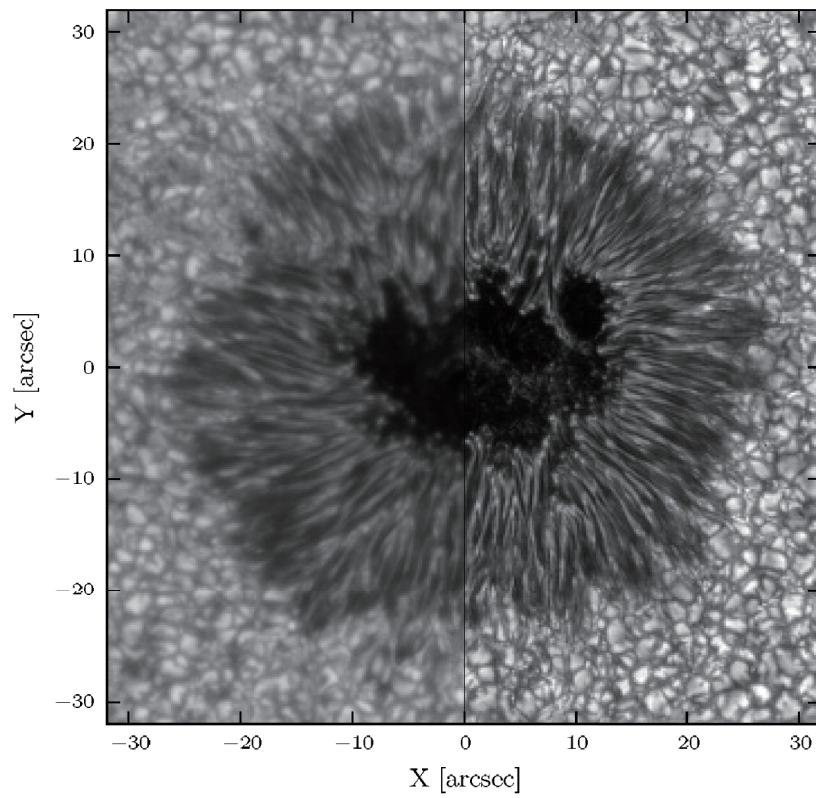
Figure 1.7: Continuum image of sunspot before (left half) and after (right half) deconvolution (van Noort 2012).

Chapter 2

Observations

The data examined in this thesis was acquired with the Solar Optical Telescope (SOT) aboard the *Hinode* spacecraft. In this chapter, the employed observational instruments and the examined dataset with its data calibration are described.

2.1 *Hinode* / Solar Optical Telescope

2.1.1 Overview of the instrument

The *Hinode* satellite (Kosugi et al. 2007) was launched in September 2006. It is equipped with three telescopes: the EUV imaging Spectrometer (EIS; Culhane et al. 2007) and the X-Ray Telescope (XRT; Golub et al. 2007), and the Solar Optical Telescope (SOT; Tsuneta et al. 2008) (Fig. 2.1). The SOT's observing wavelength bands are in the visible light for a diagnosis of photospheric physical conditions, such as magnetic field strength, its three-dimensional orientation, and Doppler velocity.

The SOT includes two components: the Optical Telescope Assembly (OTA) consists of a Gregorian 50-cm aperture, e.g., its diffraction limit at 630 nm is $\approx 0.''3$, which corresponds to ≈ 200 km on the solar surface; the Focal Plane Package (FPP) houses Filtergraphs (FG) and Spectro-Polarimeter (SP), they work together for diagnosing the

photospheric dynamics. The latter instrument is well-suited to our study thanks to its high precision performance with spectral data. The optical schematic view of the SOT is shown in Fig. 2.2, where the SP is painted in magenta. The SP is designed to obtain the four Stokes profiles of two magnetic sensitive spectral lines Fe I lines at 630.15 nm and 630.25 nm, providing magnetic field vector (Ichimoto et al. 2008). The SP is an off-axis Littrow spectrograph: incident light is imaged at the slit plane; the light passing the slit is collimated at the grating by the Littrow mirror and the grating disperses the light in the wavelength direction; finally it is imaged on the CCD by the Littrow mirror (Lites et al. 2013). The SP covers wavelength from 630.08 to 630.32 nm with the spectral resolution of 0.03 nm and the sampling by CCD pixels of 0.0215 nm.

The SP obtains the spectral data at one time for one slit oriented along the solar North-South direction. When we need a 2-D spatial map where each pixel has the spectral data, the folding mirror on the scanning mechanism moves solar image on the slit in the East-West direction. Consequently, the SP records the spectral data at each slit position, which is called *slit scan observation* (Fig.2.3). Note that the slit scan observation takes a long duration (several tens of minutes to a few hours) when we cover a wide field-of-view (FOV), and thus the spectral data at each slit position is recorded at a different time.

2.1.2   Imaging performance of the *Hinode*/SP

Many elaborate designs are considered in the SOT to achieve *the diffraction limit performance.* This performance is defined as that incident energy distribution from a point source, normalized by the peak of the energy distribution without aberration, has greater than 80% (Schroeder 2000). The pointing jitter is a a major concern that degrades the image quality. The causes of the jitter are categorized into two sources, one of which is at lower frequency owing to spacecraft body-pointing excursions, and the other is at higher frequency originating from the OTA pointing-axis fluctuations induced by the moving
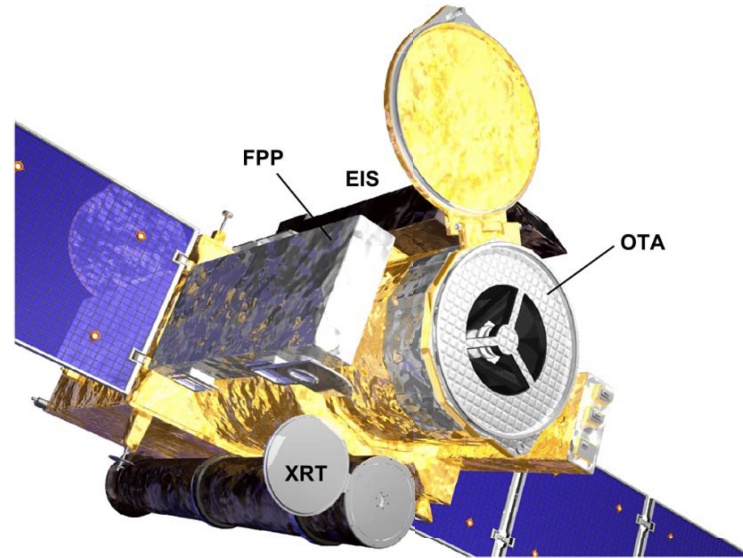
Figure 2.1: *Hinode* outlook in orbit.
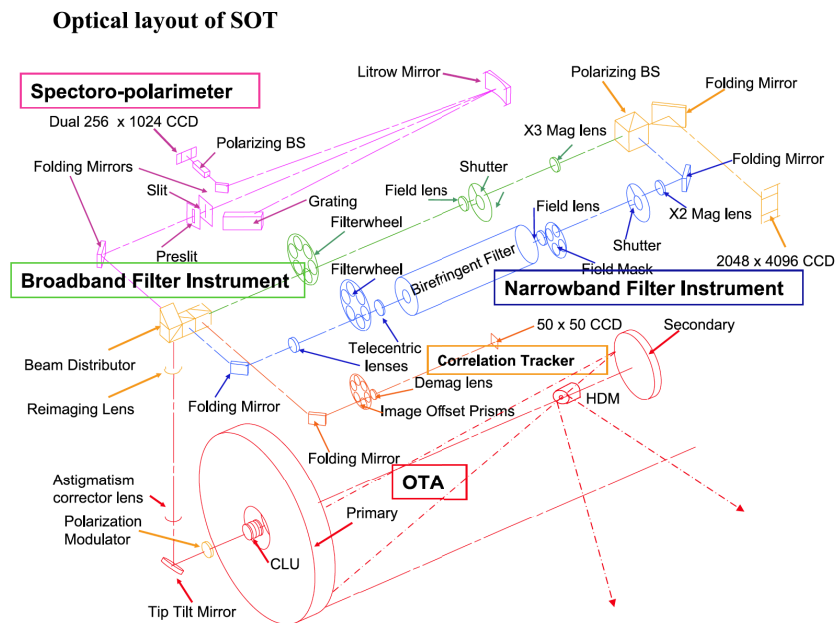
Figure 2.2: Optical layout of the SOT with the OTA and the FPP (Tsuneta et al. 2008).
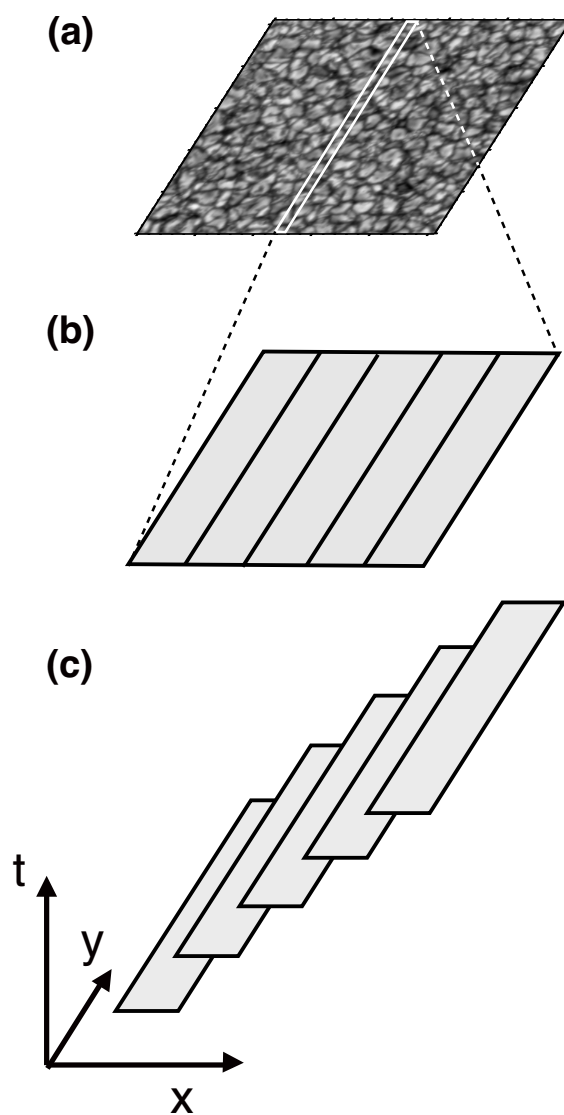
Figure 2.3: Schematic views of the slit scan. (a): Observed solar granulation seen with the continuum intensity. (b): A part of the FOV in schematic view, consisting of consecutive 5 scanning in the direction of solar E-W. (c): Schematic view of the 3-dimensional (x, y, t) information for each scanning, showing the actual time difference happening in the E-W direction. The time interval depends on the exposure time for each observation.

elements in the instrument (Suematsu et al. 2008). The higher-frequency jitter is damped by the structural design of the telescope and spacecraft, while the lower-frequency (< 14 Hz) jitter is successfully reduced by real-time stabilization system (Shimizu et al. 2008). The residual jitter with on orbit data was confirmed to be $0.''03$ (3σ), which is much lower than the original requirement of $0.''09$ (3σ) for the SP observation.

Despite those elaborate fabrications, other degradations unavoidably happen in the instrument, particularly in the OTA. The instrumental PSF data previously obtained from the *Hinode* pupil presented in Suematsu et al. (2008), see Danilovic et al. (2008) for more details. They modeled the optical path of the telescope and transfer optics to the entrance spectrograph slit, based on the commercial optical design software ZEMAX. Their computation included main image degradation factors due to the telescope aperture, central obscuration by the secondary mirror and its attachment spider, defocus, and spatial sampling of the CCD detectors. The resulting PSF is described in Fig.2.4, and has been applied to other studies' deconvolution processing (van Noort 2012; Ruiz Cobo & Asensio Ramos 2013). The OTA has a circular 50cm aperture, and its PSF can be described by the Airy function, which is clearly seen in Fig.2.4 as the rippling distribution extends toward outside. A central part of the telescope is shielded by the secondary mirror, which is simply a linear obscuration of 17.2 cm ($\approx34\%$ of the main mirror), causing an enhancement of the side-lobe of the PSF. Three spiders with 4 cm width to hold the secondary mirror, making non radial-symmetric distribution of the PSF. A slight defocus is occasionally permitted in *Hinode*'s operation so that it avoids frequent activation for the focus adjustment mechanism. Final degradation is integration effects on the CCD detectors, which is represented by powers of sinc function.

We consider those PSF as being independent on each observation, but the optimal focus position is difficult to know precisely. Defocus should be almost constant for all the dataset through an author's careful check when each observation was performed. The author's possible misjudgment causes a small degradation, e.g., the intensity contrast in
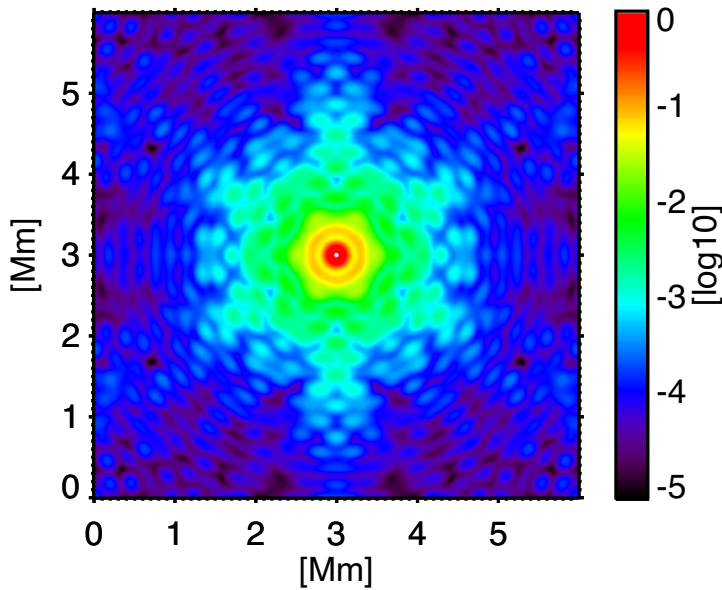
Figure 2.4: PSF of *Hinode*/SP provided by S. Danilovic and obtained from the *Hinode*/SOT pupil noted in Suematsu et al. (2008). The spatial scales correspond to the geometrical distances in the solar surface. Their values are normalized to the peak one located on the center.

RMS is $\approx$0.1% (Danilovic et al. 2008). Another degradation is due to a displacement of imaging formation position, which happens particularly at the edge of the CCD plane. All the dataset were set to use only a central part of the CCD plane so that this degradation should minimally generate the PSF's spatial dependence on the FOV.

2.2 Datasets examined

All the observational dataset analyzed in this study were acquired with the *Hinode*/SP. One of the dataset is observed at the solar disk center, i.e., the angular distance of μ=1.0, so that the LOS is aligned with the purely vertical direction of the solar surface. From now on the angular distance is signified in $\mu = \cos \theta$, where θ is the angle from the solar disk center, e.g., $\mu = 1$ means the solar disk center and $\mu = 0$ does the solar limb. The observation was acquired on August 25, 2009, between 08:01 and 09:59 UT. The setup of this dataset adequately satisfies our requirements, because deconvolution process

needs a moderate spatial coverage over the granulation with a high-cadence data, as later explained. The observed region corresponds to a quiet Sun observation, where the granulation pattern is ubiquitous. The dataset used a spatial pixel sampling of 0.″16. The integration time is 1.6 sec per slit position. The slit has a length of 60.″9 and is oriented in the solar N–S direction. We scanned a small FOV of 4.″5 × 60.″9 with 30 slit positions (each slit-step corresponds to 0.″15) for 117 times with a cadence of approximately 62 s. Fig. 2.5 shows the continuum intensity I_c, normalized by a value averaged over the entire FOV, for the first 11 scans where the granulation pattern and its evolution can be clearly identified.

The other dataset observed at several angular distances are suited to the horizontal flow analysis. The SOT team members including the author have performed a raster scan from the solar disk center to the north limb within one year intermittently. Parts of the μ range are overlapped with respect to each dataset so that the wide coverage of μ from 0.96 to 0.11 is continuous (Table. 2.1). The same observational setup (e.g., pixel sampling and integration time) as the disk center data is employed, except for its slit-length changed to longer one (81.″2). The observation duration of these dataset typically achieves one hour, which are fairly longer than a typical lifetime of the granulation (6 min; Hirzberger et al. 1999a) and the oscillatory motions (5 min; Deubner 1974).

2.3   Data calibration

The SP data were calibrated with the standard calibration routine SP_PREP, which is available in SSW (Solar SoftWare) (Lites & Ichimoto 2013). The SP_PREP routine performs i) dark-field correction, ii) flat-field correction, iii) compensation for residual I,Q, U, and V crosstalk, iv) the correction of curved spectral line, v) the removal of periodic wavelength and spatial shifts in the period of the spacecraft orbit (about 98 minutes), caused by the thermal deformation of the instrument optics, vi) the calibration of intensity variation along the SP slit caused by tiny variation of the slit width, and those
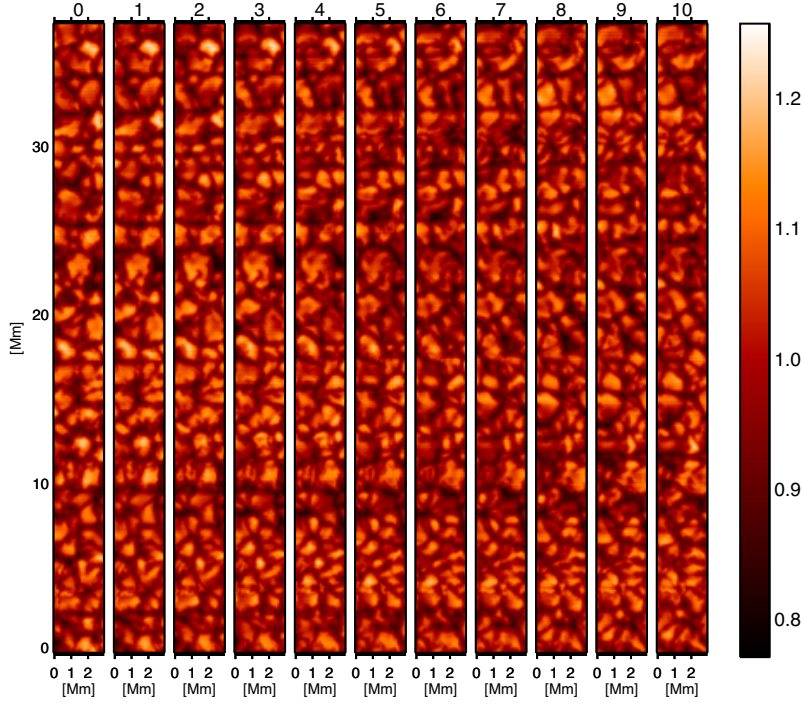
Figure 2.5: Evolution of the granulation with the continuum intensity I_c. The vertical axis corresponds to the slit-direction, and the horizontal axis represents the scanning-direction with a spatial sampling of roughly 100 km. The numbers above each map designate the time sequence with a cadence of 62 s.

Table 2.1: Dataset description from disk center to limb

Heliocentric angle (x, y) [arcsec]	μ	Date	Duration [min]
(0, 309)	0.93-0.96	2017/5/19	58
(0, 379)	0.90-0.93	2017/5/17	48
(0, 449)	0.85-0.90	2017/5/13	71
(1, 521)	0.81-0.86	2017/4/28	98
(4, 587)	0.75-0.82	2017/4/13	68
(0, 658)	0.68-0.76	2017/4/12	66
(6, 729)	0.59-0.69	2017/4/08	69
(23, 799)	0.46-0.59	2016/8/23	141
(0, 859)	0.36-0.53	2017/2/19	53
(2,920)	0.11-0.41	2017/2/22	64

corrections are based on pre-launched sunlight calibration data.

Adding to the above standard calibration, we estimate a wavelength error by using a *mean line profile*, averaged spatially and time over a large number of granules and intergranular lanes in the entire FOV. The resulting profile is slightly blue-shifted, which is called *convective blueshift* (Dravins et al. 1981). According to a well-calibrated catalogue of the convective blueshift (Allende Prieto & Garcia Lopez 1998), the Fe I 630.15 nm shows $\approx$200 m/s with an error of 100 m/s, while our convective blueshift does 140 m/s. This difference is 60 m/s, and hence this is within their error (100 m/s). Accordingly, we judged that the calibration routine SP_PREP performs well on the wavelength offset.

Chapter 3

Analysis methods

To derive the convective velocity fields along the LOS, the *Hinode*/SP dataset has to undergo a series of 4 processes (Fig.3.1). Firstly, dataset is linearly interpolated over the time dimension to have uni-temporal time at all the slit positions for each scanning map, which is necessarily for deconvolution processing and the 5-min oscillation removal (section 3.1). Secondly, our deconvolution technique is processed to correct for the instrumental degradation (section 3.2). Thirdly, *bisector analysis* is applied to derive the velocity fields along the LOS at multiple heights (section 3.3). Fourthly, a filtering process is performed to separate convective motions from 5-min oscillations (section 3.4). Besides, the derivation of horizontal flow requires analysis for the observations at multiple angular distances (section 3.5), while the vertical one simply requires the observation at the solar disk center. This chapter explains the details of those steps one-by-one.

3.1   Making spectral map

Even after the dataset has been successfully calibrated as described in section 2.3, there is still another concern; the dataset has two spatial dimensional information, i.e., slit and scanning directions, but the latter spatial dimension permeates the time dimension since the SP makes spectral map by slit scanning, as already illustrated in Fig.2.3. Conse-
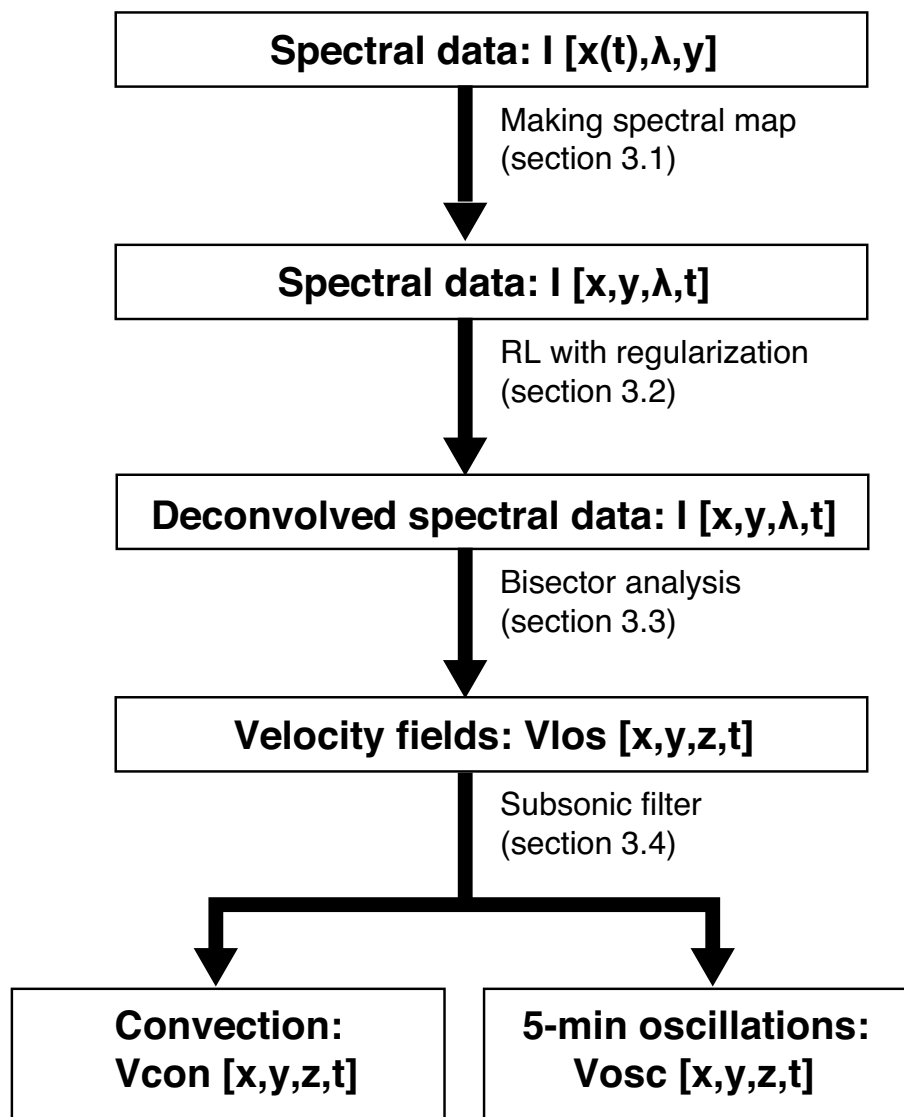
Figure 3.1: The flowchart of the analysis to derive the convective velocity fields along the LOS.

quently, each slit position along the E–W direction is recorded at a different time. Because the deconvolution process needs the information outside the observed slit position *at a certain time*, we need a two-dimensional spectral map where all spatial locations correspond to the same time. Such a uni-temporal image is also needed to remove the 5-min oscillations, which are larger spatial scale phenomena producing fluctuations in the photosphere. To relax the time difference at each slit position, we perform a linear time interpolation from consecutive raster scans and produce a pseudo-instantaneous spatial image (see more details in Fig.3.2 and its caption). Since the time interval of linear interpolation (roughly 1 min for one scan) is fairly shorter than the typical 6-min granulation lifetime (Hirzberger et al. 1999a) and the 5-min period of sound wave's fluctuation, this interpolation should not adversely influence our results.

This approach would extend the availability of two-dimensional slit scan data, providing an opportunity to remove the unwanted effects, e.g., the spatial degradation and the 5-min oscillations. It should be stressed that, however, this processing would be applicable only to short-scan observation, attaining fairly shorter timescale interpolation than the concerned phenomena, e.g., the granulation and 5-min oscillations here.
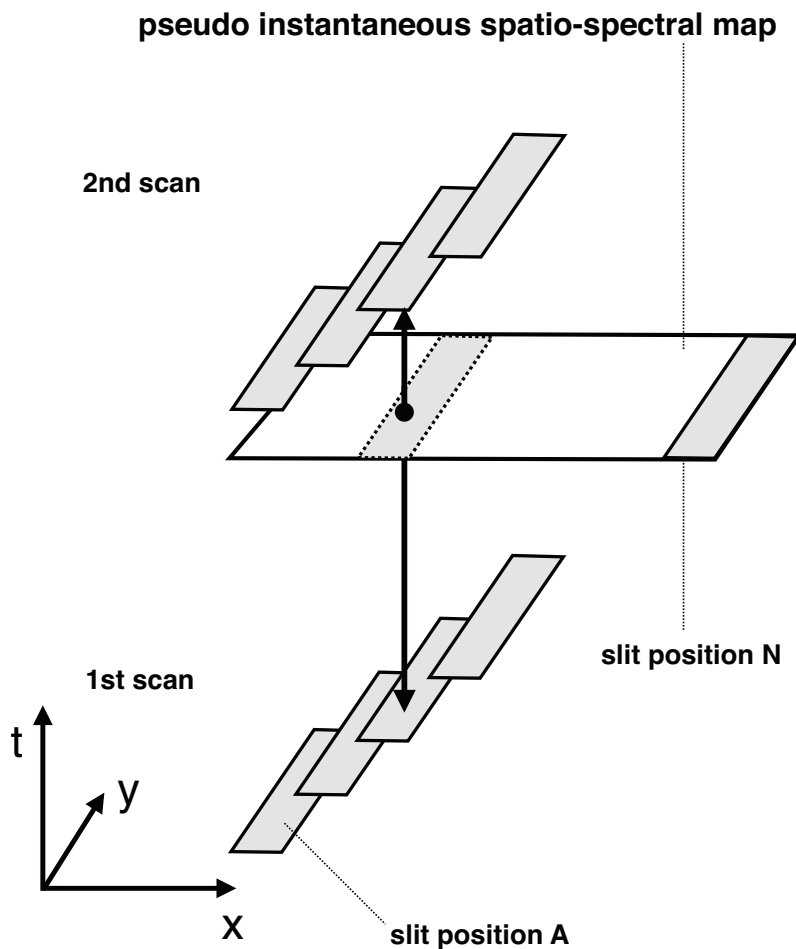
Figure 3.2: Illustration of how to make a pseudo-instantenuous two-dimensional spectral map. Spectra are recorded along the slit at each x-position, starting from the left (at position A) and moving to the right with time, i.e., scanning along the x-direction. After the last slit position (position N) of a scan, the scanning position goes back to the first position (position A) and the process is repeated. To make a pseudo-instantaneous spatio-spectral map at a given time at the end of the first scan (indicated by the larger rectangle), the slit data at each spatial x-position are computed by linearly interpolating between the 1st and 2nd scans as indicated by the vertical double-headed arrow and the dotted rectangle lying in the larger rectangle.

3.2   Deconvolution method

In this section, we explain the basis of the deconvolution technique. The observed image can be expressed as

$$I(x, y) = \int \int_{-\infty}^{\infty} I_0(x', y') \, PSF(x, y : x', y') \, dx' dy' + \epsilon(x, y), \qquad (3.1)$$

where $I(x, y)$ is the observed intensity image, $I_0(x', y')$ is the ideal image, $PSF(x, y : x', y')$ is the point-spread function, and ϵ is a random noise described with a Gaussian distribution and its average being zero. The equation is often abbreviated in the form $I = I_0 * PSF + \epsilon$, where $*$ signifies convolution. This equation signifies that the observed intensity at a given pixel has an intensity leakage from the surrounding pixels in the ideal image. The goal of deconvolution is to obtain the ideal image I_0 by removing out this leakage, using a given PSF and the observed intensity $I(x, y)$. Finally, the images deconvolved at each wavelength are combined to provide deconvolved spectral data.

3.2.1   Richardson-Lucy Algorithm

Several types of spatial deconvolution techniques have been proposed (see for instance Jansson 1997 for an overview). In this study, we adopt the Richardson-Lucy (RL) algorithm (Richardson 1972; Lucy 1974), which is the widespread use for the *Hinode* data's deconvolution (e.g., Mathew et al. 2009; Ruiz Cobo & Asensio Ramos 2013; Quintero Noda et al. 2015). This algorithm is an iterative scheme used to increase the probability of the Poisson distribution. We assumed the following image formation model:

$$i(X) = o * h, \qquad (3.2)$$

where i is the observed image, the variable X is two-dimensionally represents for (x, y), o is the object image we aim to derive, and h is the PSF. Under the influence of Poisson noise, we have to deal with $i = \varphi(o * h)$, φ being a Poisson distribution. The probability of our measurements falling within a Poisson distribution can be expressed as

$$p\left(i|o\right) = \prod_X \left(\frac{\left[h * o\left(X\right)\right]^{i(X)} e^{-(h*o)(X)}}{i\left(X\right)!} \right),$$ (3.3)

where ! is the factorial. Our goal is to find the $o(X)$ that maximized the probability of $p\left(i|o\right)$ to most likely produce the observed value of $i(X)$. To search for the solution, we used the following algorithm in a multiplicative way,

$$o_{k+1}\left(X\right) = \left\{ \left[\frac{i\left(X\right)}{\left(o_k * h\right)\left(X\right)} \right] * h\left(-X\right) \right\} o_k\left(X\right).$$ (3.4)

Equation (3.4) describes an iteration step of the RL algorithm that retrieves the real image through an iterative scheme. We stressed here the weakness of this algorithm; in the case of an observation with noise, the RL algorithm does not always converge to a suitable solution because of the amplification of noise after several iterations. One solution is to preprocess the noisy image, as Ruiz Cobo & Asensio Ramos (2013) and Quintero Noda et al. (2015) reduced the noise on the profiles before deconvolution by performing a filtering process with the Principle Component Analysis (PCA) (Loève 1955).

3.2.2   Richardson-Lucy Algorithm with the regularization term

We follow a different approach on treating the noise: we add a regularization term, so-called Tikhonov-Miller regularization, to reach a suitable solution (Dey et al. 2004). This method searches for a spatially-smoothed solution in the ideal image by allowing non-maximum probability of $p\left(i|o\right)$ in finding the answer, and thereby limits the enhancement of fluctuations at the highest spatial frequency. Instead of the original Richardson-Lucy

algorithm given in Equation (3.4), we obtain a regularized form of the RL algorithm,

$$o_{k+1}\left(X\right) = \left\{\left[\frac{i\left(X\right)}{\left(o_k * h\right)\left(X\right)}\right] * h\left(-X\right)\right\} \frac{o_k\left(X\right)}{1 + 2\lambda_{TM}\Delta o_k\left(X\right)}, \qquad (3.5)$$

where λ_{TM} is the regularization parameter, and Δ is the Laplacian operator. The observed image o_k and the PSF h are known parameter, whereas the regularization parameter λ_{TM} can be chosen freely. It is important to adopt an appropriate value into λ_{TM} because the success of the regularization depends on the amount of the noise to be suppressed. The larger the value of the parameter λ_{TM}, the greater the likelihood of a spatially-smoothed image with a large departure from the observed image. On the other hand, for small value of λ_{TM}, the algorithm assumes that any observed signal, including the noise, has physical meaning. This effect favors the enhancement of noise signals with each iteration. The selection of the best parameter value is explained in section 3.2.4.

We refrained from correcting for the spectral degradation caused by the dispersion in the grating because the deformation of spectral profiles is considered to be negligible. Using a tunable laser, Lites et al. (2013) measured the SP-spectral-response profile prior to launch. On the basis of their degradation profile, the estimated spectral degradation is deviated less than 0.01 of I_c from the non-degraded profile at the intensity range used for our bisector analysis (see section 3.3). Because this residual intensity of 0.01 is smaller than the observed random noise of 0.012 measured in the continuum intensity fluctuation, the compensation of this spectral degradation is difficult to performe. Even if performed correctly, this intensity difference (0.01) affects the velocity fields of 0.045-0.090 km/s, see the section 3.3 for how to estimate the values.

3.2.3   PSF of the telescope

Our spatial deconvolution code requires the PSF (see Eq.3.5). Here we use the modeled PSF data, previously explained in section 2.1 with their spatial pixels rescaled to our
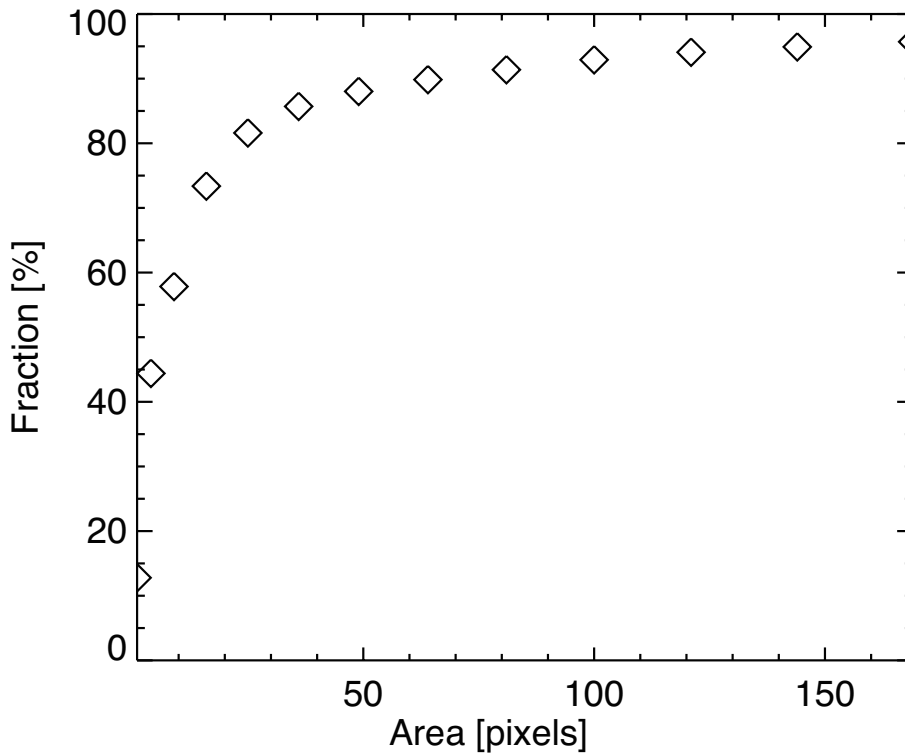
Figure 3.3: Total fraction of the PSF contained within a given square area, expressed in pixels. Diamond symbols correspond to the fraction of the PSF contained within squares with an area of 1, 4, 9, 16, ..., 169 pixels, which are equivalent to a length of one side of the square of 1, 2, 3, 4, ..., 13 pixels.

Hinode's dataset. Since the scanned area is narrow, we need to limit the extent of the PSF. To this end, we calculated the total energy contained within a set of squares of different areas, each corresponding to a square number of detector pixels, 1x1, 2x2, 3x3, etc. The results are plotted in Fig.3.3. In raw data (i.e., without any deconvolution), any given pixel contains only 13% of the observed intensity from the corresponding location, while the remaining 87% originates from outside. The total energy contained in a given area increases rapidly as the area increases. A square of 13×13 pixels contains 96% of the intensity. Considering that the remaining 4% does not contribute significantly to the observed information, we use only the central part of the PSF contained within these 13 $\times$ 13 pixels. Moreover, we also normalized the PSF function, i.e., the total integrated area is unity.

3.2.4 Verification exercise

To estimate how accurately our deconvolution technique correct for the degradation by
the instrument PSF and restore the observed images, we use images synthesized from a
numerical simulation as test images. For this purpose, we synthesize the spectral profile of
the Fe I lines at 630.15 nm, using the numerical code SPINOR (Frutiger et al. 2000; Frutiger
2000), on the basis of the atmospheric parameters simulated by the MURaM code (Vögler
et al. 2005), see the details of both numerical codes in Appendix A. The advantage of the
approach with the numerical simulation is that the object image we aim to derive is priori
known and has a similar morphology and intensity contrast as the real one (Danilovic
et al. 2008). This simulated continuum intensity map is binned to a spatial sampling of
100 km for a direct comparison with the *Hinode*/SP observations. From now on we call
it *the answer-image*. The answer-image is obtained from the snapshot displayed in Panel
(a) of Fig.3.4. To mimic the observed intensity map of the *Hinode*/SP, we convolve the
answer-image with the instrument PSF, and introduce Gaussian random noise. We call
the resulting degraded image *the imitated-image*, shown in Panel (b). The variance of the
introduced random noise is calculated from the observed continuum intensity, and is 0.012.
The retrieved image through the conventional RL algorithm without any regularization
after 50 iterations is shown in Panel (c). The scatter plot of this retrieved image versus
the answer image is drawn in Panel (e) with a standard deviation of 0.0406. An image
retrieved by the regularized RL algorithm is shown in Panel (d), here $\lambda_{TM} = 0.0016$ is
adopted because this is the optimum value as explained later. A scatter plot of the image
retrieved by the regularized RL algorithm versus the answer-image is shown in Panel (f),
and displays a standard deviation of 0.0371. Those standard deviations are much smaller
than those between the answer-image and the imitated-image, 0.145.
 In tested images with substantial noise included, the RL algorithm without regularization
dose not converge to a suitable solution. Fig.3.5 shows the standard deviation between
the answer-image and the deconvolved image as a function of iteration number; the solid
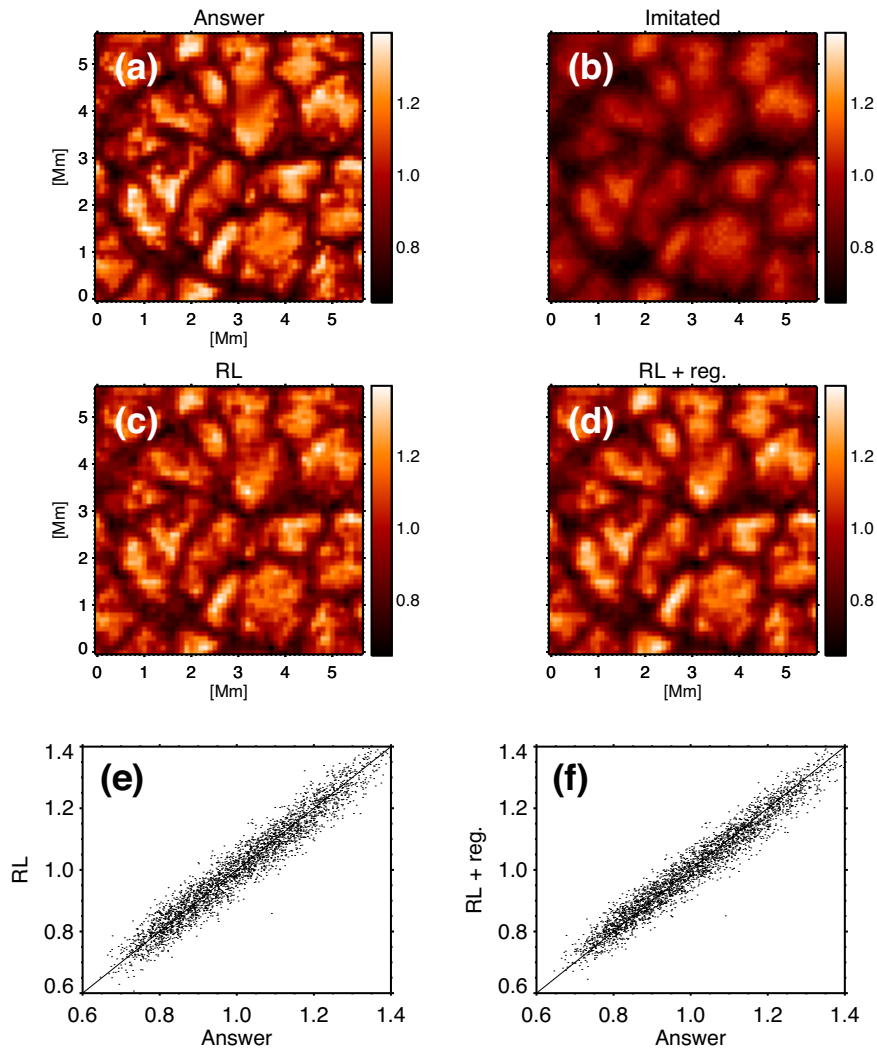
Figure 3.4: Comparison of the original image to the one retrieved through deconvolution. *Panel (a)*: *the answer* image, which is the simulated original continuum intensity with a spatial scale of ≈ 100 km. *Panel (b)*: *the imitated* image, which is produced by convolving the answer-image by the PSF and additionally introducing Gaussian random noise. *Panel (c)*: the intensity map retrieved by the RL algorithm without any regularization at an iteration number of 50. *Panel (d)*: the intensity map retrieved by the extended RL algorithm including the regularization term. *Panel (e)* is a scatter plot between *the answer-image (Panels (a))* and the intensity retrieved through the RL algorithm without regularization (*Panel (c)*). *Panel (f)* indicates a scatter plot between *the answer-image* (*Panel (a)*) and the intensity retrieved through the RL algorithm with regularization (*Panel (d)*).

curve shows the result with the original RL algorithm, and the dashed curve shows that with the regularized RL algorithm using a λ_{TM} of 0.0016. In the RL algorithm without regularization, the minimum standard deviation (the best output) occurs at the 29th iteration. For additional iterations, the standard deviation increases again, i.e. noise component is enhanced. Since the optimal iteration number is a priori unknown, we easily adopt an excess iterating and thereby enhance noise unduly, as seen in Fig.3.4 (c) with 50 iterations. The RL algorithm with regularization behaves better in this respect. Although the standard deviation increases slightly with increasing number of iterations beyond the optimal iteration number (36th), this method still attains high accuracy without excessive noise enhancement. Whereas both the RL algorithm without and with regularization attain almost the same accuracy at their optimal iteration number, the latter algorithm can provide a stable output regardless of the iteration number.

As mentioned previously, while users need to assign a value into the regularization parameter λ_{TM}, it is difficult to find the appropriate one. Accordingly, we check the accuracy of the various deconvolution processes, adopting different values of λ_{TM} to determine which parameter value provides the most reliable image. To visualize the correlations between the answer-image and the retrieved image, we use various $\log_{10}\lambda_{TM}$ from -2 to -5 with a spacing of 0.1. In Fig.3.6, we plot the corresponding standard deviations between the answer-image and the image retrieved by the regularized RL algorithm, and found that the minimum value (i.e., the best correlation between their images) is located around 0.0016, i.e., -2.8 on the logarithmic scale. Therefore, this value of λ_{TM} is adopted because it provides the best estimation of the answer-image. Besides, Figs.3.5 and 3.6 reveal that the best results obtained by the conventional and our RL algorithm are nearly the same quality, although the algorithm in its regularized form leads to slightly lower standard deviations. Fig.3.6 illustrates the main shortcoming of the RL algorithm with regularization; the appropriate value of λ_{TM} for a particular type of data set is not *a priori* known and simulations cannot always be used to fix it as we have done here.
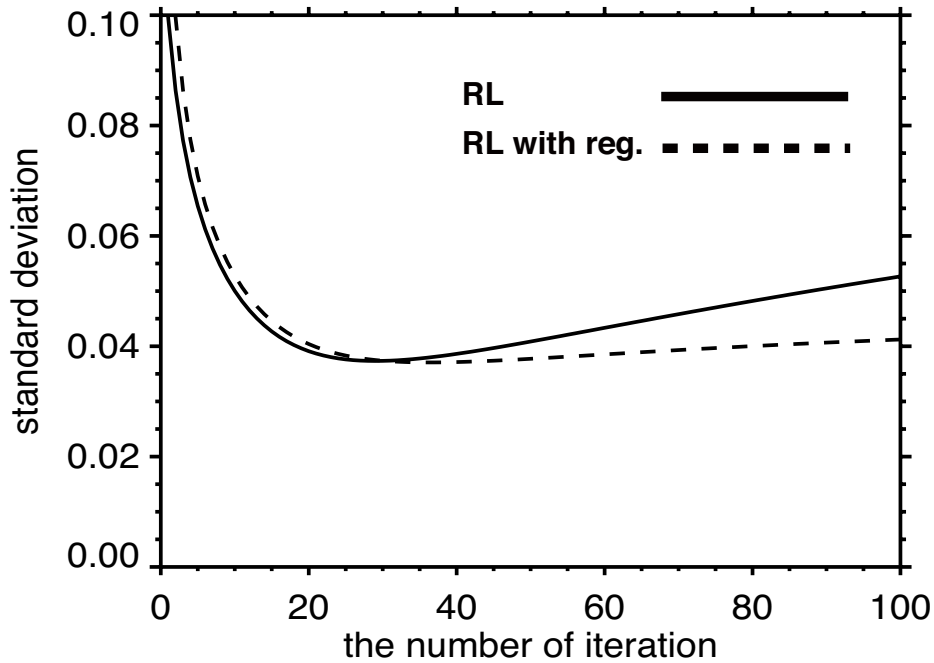
Figure 3.5: Standard deviation between *the answer-image* and the deconvolved image as a function of the iteration number. The solid line represents the standard deviation achieved by the original RL algorithm, and the dashed one that by the RL algorithm with regularization using $\lambda_{TM} = 0.016$ (see main text and Fig.3.6 for the reasons behind this choice).

3.3 Bisector analysis

To derive the velocity field, we apply *bisector analysis* (Dravins et al. 1981) to the observed spectral lines. A bisector divides a spectral profile into two parts having the same equivalent width, and the wavelength offset of the bisector from the original positions can be transformed to Doppler shifts at various intensity levels (Fig.3.7). Consequently, it provides multiple velocity fields at different heights, as each intensity level originates from a different height. Because the absorption coefficient monotonically decreases toward the wings of both sides while it peaks at the line core, indicating that the line core and wings originate from higher and lower layers, respectively. The LTE condition is mostly
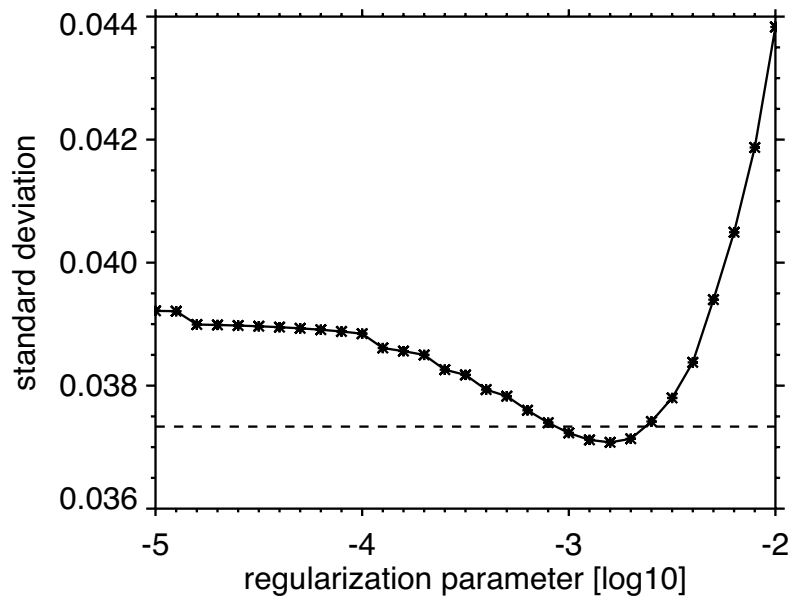
Figure 3.6: Standard deviation between *the answer-image* and the image retrieved by the RL algorithm with regularization as a function of the regularization parameter, λ_{TM}. The horizontal dashed line indicates the minimum standard deviation reached by the RL algorithm without regularization.

satisfied in the photosphere, resulting in that an observed brightness is simply expressed by certain temperature there (i.e., expressed by Planck function). The reason why height structure can be extracted from line profile is supported by the *Milne-Eddington model*, in which in the optically thick regime a certain intensity comes from at a layer of $\tau = 1$ under the temperature gradient with 1st-order under the LTE-condition (Mihalas 1978). Thus, the following expression is well-usable: an emergent intensity is expressed by the corresponding temperature via the Planck function and most part of the intensity originates from there.

The bisector analysis is applied only to the spectral line Fe I at 630.15 nm, while the *Hinode*/SP simultaneously observes the other line Fe I at 630.25 nm. One advantage of this line selection is that the bisector analysis can provide a broader height extent thanks to the relatively higher formation layer of this spectral line. Another advantage is its less sensitivity to magnetic field through the Zeeman effect. Moreover, for safety, we avoid

strong magnetic field concentration in the FOV.

Here we introduce a criteria of which intensity levels to sample via bisector analysis. The highest bisector level is defined to be 0.10-0.15 of I/I_0 below the continuum intensity, and the lowest level is 0.05 of I/I_0 higher than the line core intensity, with a grid spacing of 0.05. Note that I is intensity level at each spatial pixel, and I_0 is the estimated continuum intensity on average in the disk center, as later explained. Line profiles originating from granular regions have typically higher continuum intensity and lower line core intensity. One example of such a profile in granule with a calculated bisector is shown in Fig. 3.7 (a), and a zoom-up view of the bisector in Fig. 3.7 (b); its continuum intensity is 1.13 with a line core intensity of 0.26. Consequently, our criterion for bisector analysis covers the intensity range between 0.30 and 1.00, consisting of 15 sampling. In contrast to granules, line profiles in intergranular lanes typically have a lower continuum intensity and higher line core intensity, making the number of the bisector sampling smaller. This example is illustrated in Fig. 3.7 (c) and (d); the continuum intensity is 0.92 with a line core intensity of 0.42. Hence, the bisector sampling consists of 8 intensity levels covering from 0.45 to 0.80.

We computed the bisectors on the intensity range 0.45-0.70, with a step of 0.05. Outside those intensity levels we do not trust the bisector results, i.e., the spectral lines in intergranular lanes are shallow in comparison with those of granular regions. These bisector levels can be assigned to have respective corresponding heights. Based on the 1D photospheric model (Vernazza et al. 1981), those six bisector levels correspond to geometrical heights of 49, 62, 77, 92, 112, and 135 km, respectively, through the Planck function. We stress, however, that as the solar atmosphere is highly structured, the actual height at which radiation is emitted changes strongly from one horizontal position to another. Stein & Nordlund (1998) estimated that this geometrical height corrugation of the surface ($\tau = 1$) is $\approx$30 km in RMS, as the layer goes up the corrugation decreases. While such a corrugation decreases as a geometrical height rises up, those estimated geometrical

heights should be referred with extreme caution.

Our bisector analysis is to sample the identical geometrical heights even among the different angular distances, by normalizing the observed spectral profiles with I_0 which is defined as the estimated continuum intensity (DN) in the disk center. Any observed light with certain intensity originates from the corresponding temperature height under the LTE assumption. Since the solar temperature stratification is almost invariant with respect to angular distance (e.g., a slight enhancement of 2-3 K at the pole reported by Rast et al. 2008), the velocity fields sampled at the absolute DN with our bisector analysis would reflect the same temperature layer, irrespective of angular distance. Note that all the dataset are set to adopt the same exposure time (1.6 sec). One noticeable concern is the time-dependent instrumental throughput, because one of the dataset was acquired in 2009 while the others done in 2016-2017, as Lites et al. (2013) reported a decreasing trend of the throughput year by year (about 17 % in five years). Referring to scan dataset executed every month from the beginning of the *Hinode* operation, we normalize I_0 in each dataset to be identical with the reference data at the closest timing of the dataset.

The bisector is converted to the Doppler velocity v at each bisector level according to

$$v = c \frac{\Delta \lambda}{\lambda_0}, \tag{3.6}$$

where c is the speed of light (3.0×10^5 km/s), λ_0 is the wavelength of the absorption line (630.15 nm) without any motion, and $\Delta \lambda$ is the wavelength offset of the bisector from λ_0.

According to Gray (2008), we estimate the error of the velocity fields retrieved by the bisector analysis, caused by the intensity fluctuation. The error δv has a linear dependence on the intensity fluctuation δI, as denoted by $\delta v = C \, \delta I$ [km/s], here the unit of δI is the normalized value. C depends on the wavelength sampling against an intensity gradient along the spectral profile, e.g., C=4.5-9.0 for the six bisector levels in our deconvolved spectrum. At the highest accuracy of the image restoration with the deconvolution (i.e., $\delta I = 0.037$, see Fig.3.4), the retrieved velocity field has an error of 0.17-0.33 km/s.
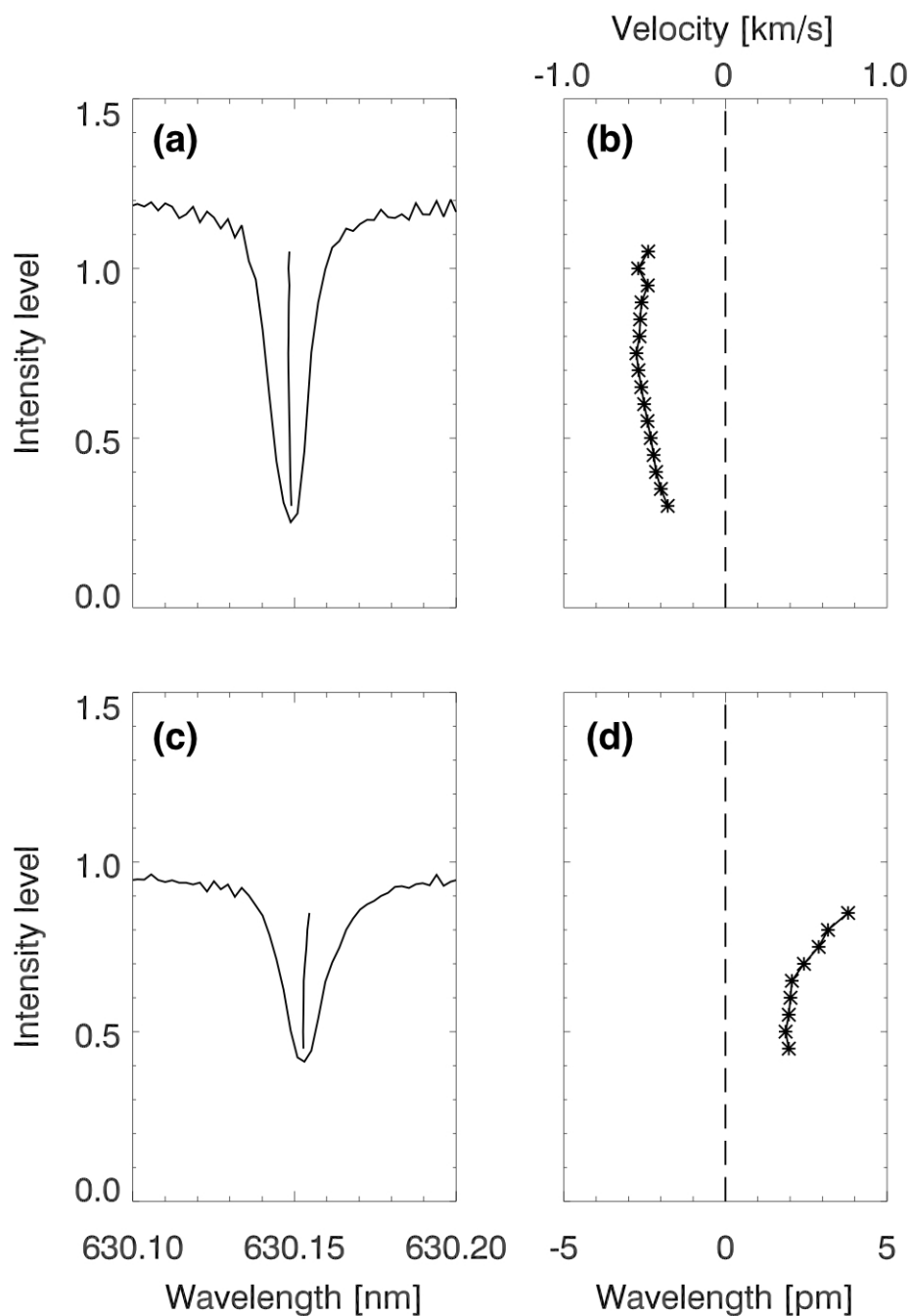
Figure 3.7: (a) Example of an absorption line (Fe I 630.15 nm) in a granule. The solid line drawn in the center of the absorption line is a bisector. (b) An enlarged view of (a). The vertical dashed line is a bisector without the influence of the Doppler shift caused by the moving parcel. The horizontal axis gives the wavelength offset from the absorption line without velocity. (c) Example of an absorption line (Fe I 630.15 nm) in an intergranular lane. (d) An enlarged view of (c).

3.4 Separating 5-min oscillations from spectral data

The 5-min oscillations consist of numerous numbers of eigenmodes, made with the solar stratification, and fluctuates in the photospheric velocity fields, as explained in section 1.2.1. A *subsonic filter* (Title et al. 1989; Rutten et al. 2004; Matsumoto & Kitai 2010) is the well-established technique to extract the convective velocity from a time series of velocity map by removing out the 5-min oscillations. This filtering is composed of three steps. First, we calculated the Fourier spectrum, so-called k_h-ω *diagram* (Fig.3.8), by transforming from real-space (x, y, t) to Fourier-space (k_h, ω), where $k_h = \sqrt{k_x^2 + k_y^2}$ under the assumption of no dependence on the horizontal directions. Second, we perform a filtering process to separate the convective motion from the 5-minute oscillations on the Fourier space. Their concentrated powers are discretely located to each other; the 5-min oscillations extends over 2-5 mHz, which corresponds roughly to 8-3 minutes, while the convection is located over low frequency domain (i.e., less than 1 mHz and 1 Mm^{-1}). We regard the 5-min oscillation as the frequency domain with $\omega/k_h > 7$ km/s, i.e., the phase velocity exceeds the sound speed in the photosphere (Stix 2004), and with $\omega >$1.5 mHz, which is the minimum frequency of the oscillation. The rest of the domain ($\omega <$ 1.5 mHz or $\omega/k_h < 7$ km/s) is included into the convection. This segmentation boundary, depicted with the distorted dashed line in Fig.3.8, seems to clearly discriminates their components from each other. Third, these two powers are transformed to real-space (x, y, t) again, thereby retrieving the convective motion and the 5-minute oscillations separately. Those sequential processes are performed for each bisector level independently.

Each dataset from the disk center to the limb undergoes the above filtering processing separately. In all the created $k_h - \omega$ diagrams, 5-min oscillatory powers appear in the same frequency domain as at the disk center, but the power decreases toward the limb due presumably to their predominant vertical fluctuations (Stix & Wöhl 1974).
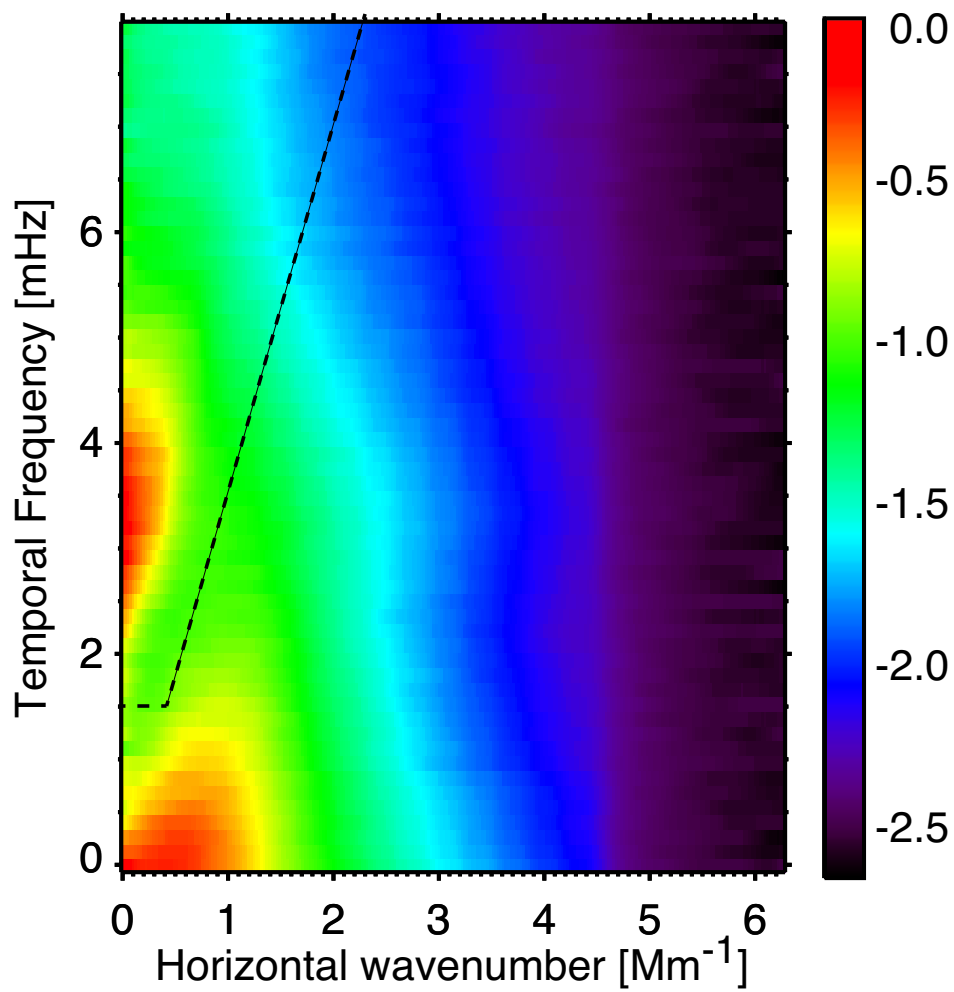
Figure 3.8: $k_h - \omega$ diagram. Dashed line is to separate the convective components from oscillatory motions. The color scale is normalized by the maximum power in $\log_{10}$.

3.5   Deriving the horizontal flow

Here we describe how to derive the horizontal flow from the LOS amplitude varia-
tion from the disk center to the limb. It is intrinsically impossible to directly obtain
the pure horizontal component as long as the sun forms a spherical stratification. Any
observed LOS flow field, except for at the disk center, consists of vertical and horizontal
components in accordance with the observer's angle, as shown in Fig.3.9 (a); the limb
observation records the horizontal flow (parallel to the solar surface) into a part of the
Doppler signal, whereas the just disk center purely does the vertical flow (perpendicular
to the surface). The *average* horizontal velocity fields can be obtained via the follow-
ing approach. Assuming that the granulation has no latitude/longitude-dependence and
both flows between vertical and horizontal directions are uncorrelated, we can apply the
following equation,

$$v_{los,rms}^2(\mu) = \mu^2 v_{ver,rms}^2 + (1 - \mu^2) v_{hor,rms}^2, \tag{3.7}$$

where $v_{los,rms}$ is observed convective velocity in RMS along the LOS, $v_{ver,rms}$ is for vertical
motion which can be derived at the disk center, and $v_{hor,rms}$ is for horizontal motion we
aim to derive (Keil & Canfield 1978). A fitting process may provide a reasonable value of
$v_{hor,rms}$ with minimum deviations between $v_{los,rms}$ in the observation of and those in this
model (equation 3.7).
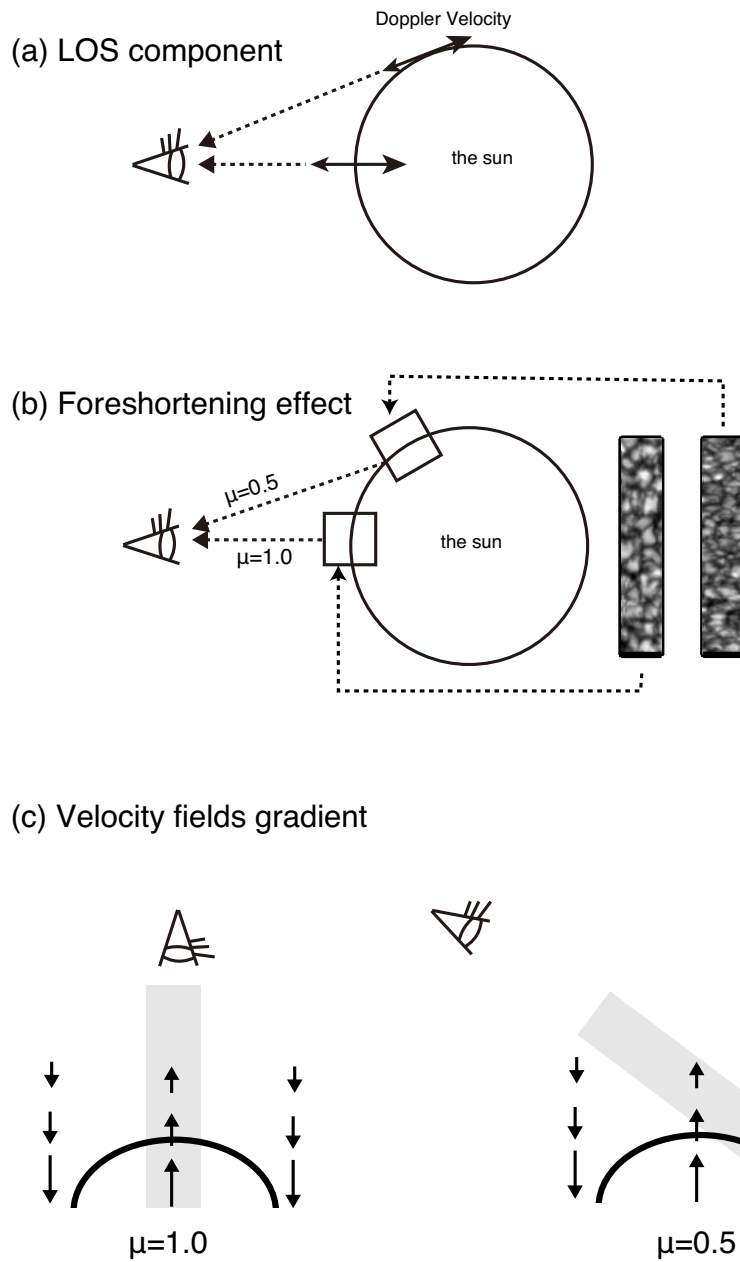
Figure 3.9: Several types of center-to-limb variation. (a) LOS component: at the disk center the LOS component purely reflects the vertical motion, whereas at the limb the LOS component partially reflects the horizontal motion in accordance with angular distance. (b) Foreshortening effect: at the limb the observer cannot resolve spatially the granulation because the angular resolution degrades at the lower angle, resulting in the compressed granular feature. (c) Velocity fields gradient: any observed intensity originates from cumulative optical path along the LOS direction. The retrieved Doppler signal is a net result of integration over its sensitive region (shown in grey color).

Chapter 4

Results

4.1 Vertical flows

The LOS direction at the solar disk center is aligned purely with the vertical direction of the solar surface. Here we treat only the disk center observation which undergoes the sequential analysis described in section 3.1-3.4 (except for the other analysis in section 3.5).

4.1.1 Spatial distribution of granulation

Figure 4.1 shows the snapshot of the continuum intensity, as well as the convective velocity and the 5-min oscillations at a bisector level of 0.70 corresponding to a geometrical height of 49 km. The top panels are derived from the observation without deconvolution, and the bottom panels represent the spatially deconvolved results. The continuum intensity contrast increases from 7.2% before the deconvolution process to 13.0% after it (see its detail in Appendix B). While we do not find notable differences in the shape of the granules, we found the presence of small-scale spatial variations inside them that are very poorly visible before deconvolution. One example can be found around [1.0,1.0] Mm: in the top panel before deconvolution, the granule is nearly monotonously bright; in the

bottom panel after deconvolution, the darkening of the inner part of the granule can be seen clearly.

The deconvolution process also improves the contrast of the convective velocity and changes its spatial distribution along with a much smaller enhancement of the 5-minute oscillation. Importantly, the downflows display a larger increase than the upflows; it can be seen immediately that the area occupied by downflows is larger in the deconvolved observation (bottom panel) than in the original observation (top panel). In more quantitative way, we define the area fraction of downflows as the ratio between the downflowing portions of the image area to the total area, and found that this value increases from 0.34 before deconvolution to 0.48 after it. These discriminated up- and downflows are beyond a threshold of ∓0.18 km/s, respectively, and this threshold value is the estimated error of the wavelength offset. This increase of the downflowing area fraction is because weak upflows at the edge of each granule transformed into downflows, which is seen at [0.8, 2.9] and [1.0, 0.5] Mm, and the narrow intergranular channels sandwiched between granules appeared to increase in width, which is seen at [0.9, 5.4] and [1.8, 2.8] Mm. Consequently, downflow channels after the deconvolution clearly separates intergranular lanes from granules, namely that upflows become isolated and downflows do connected with each other. Besides, broader intergranular lanes and junction of more than three channels have a strong downflow in their center, which is seen at [2.0, 5.6] and [1.4, 3.8] Mm, respectively, while before the deconvolution unispeed downflows pervade there. Fig.4.2 displays scatter plots before deconvolution versus after deconvolution for the continuum intensity (top panel) and the LOS convective velocity field (bottom panel). The slopes of the scatter plot for the continuum intensity and convective velocity field are 1.78 and 2.14, respectively, implying that these two values nearly/more than doubled by deconvolution, respectively. Whereas the scatter of the continuum intensity is uniform over the whole range, that of the LOS velocity has a large deviation particularly in stronger downflows, drifted toward even faster downflow than the linearly fitted solid line. It means that, as
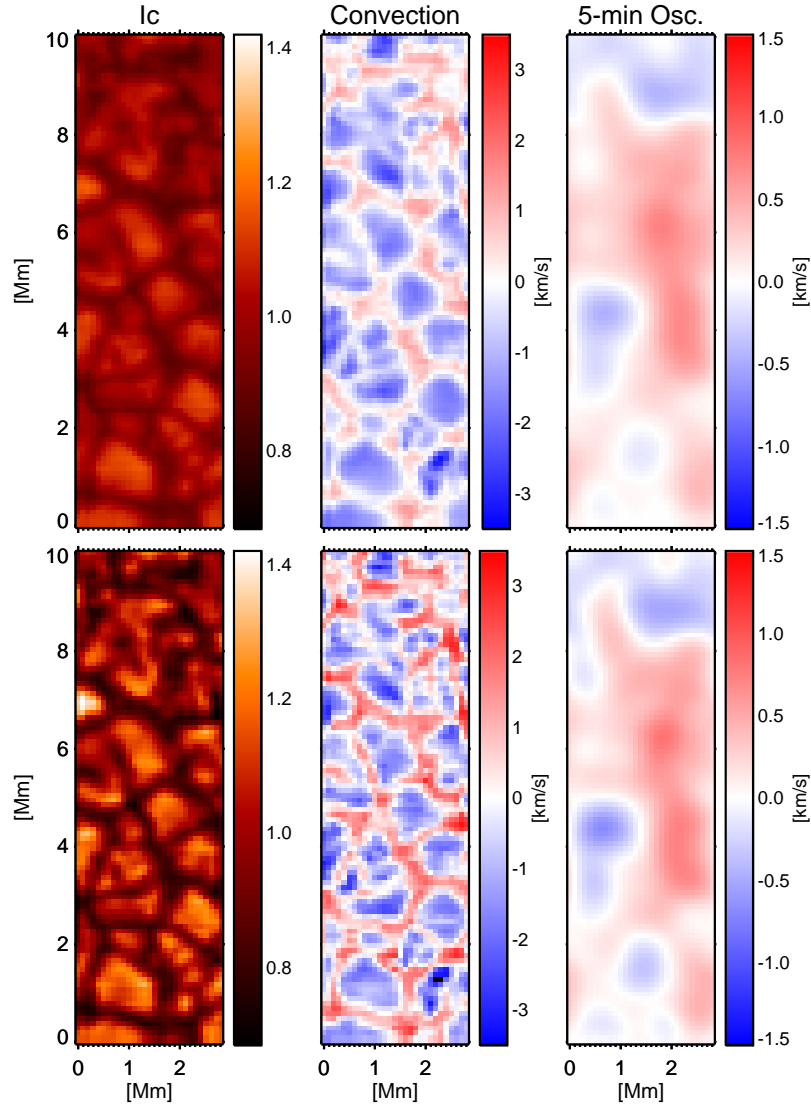
Figure 4.1: Granulation obtained from original and deconvolved *Hinode*/SP data. *The left column* shows the continuum intensity, *the center column* displays the convective velocity field at a bisector level of 0.70, and *the right column* depicts the 5-minute oscillation at the same level. *The top row* corresponds with the observations before the deconvolution, while *the bottom row* is the deconvolved ones. Positive velocity means a red-shift (downward), a negative one a blue-shift (upward).

downflow speed is higher, the deconvolution enhances the speed even more, which is seen in the broader intergranular lanes and the junctions of the lanes.

4.1.2 Magnitude of convective velocity field

Our deconvolution remarkably enhanced the convective velocity field, e.g., its RMS at a bisector level of 0.70 increases from 0.61 km/s before the deconvolution to 1.12 km/s after that. Besides, this technique also differently affects the magnitude of convective up- and downflow; calculated separately, the average speeds of up- and downflow are -0.64 km/s (upward) and +0.49 km/s (downward) before the deconvolution, but -1.14 km/s and +1.20 km/s after that. The distributions of the LOS amplitude are easily seen in their histograms of Fig.4.3. Before the deconvolution, at a bisector level of 0.70 (depicted by the black line in Fig.4.3), the distribution extends from -2.0 to +1.5 km/s, thus blue-shifted signals are typically stronger than red-shifted ones. After the deconvolution, the downflow reaches approximately the same magnitude as upflow with the distribution ranging from -3.0 to +3.0 km/s. The velocity histograms change their shape remarkably as the height decreases: in the highest layer (blue line), the deconvolution process broadens the velocity distribution without significantly shifting the peak; in the lowest layer (black line), the deconvolution not only broadens the distribution but also shifts the peak. The distribution has a long tail stretched toward downflow, representing spatially local existence of strong downflows in a tiny scale, e.g., such as junctions of intergranular channels explained in section 4.1.

The first-moment of the convective velocity distribution (i.e., averaged over all pixels in the FOV) is a rough indicator of how well up- and downflowing mass flux balance (Fig.4.4), although the density of gas also contributes and the difference in the formation heights between granules and intergranular lanes affects the results as well. Clearly, after the deconvolution, the first moment values lie closer to 0 km/s (fluctuate within ± 0.05 km/s), whereas prior to deconvolution the values exceeded -0.2 km/s. At lower intensity
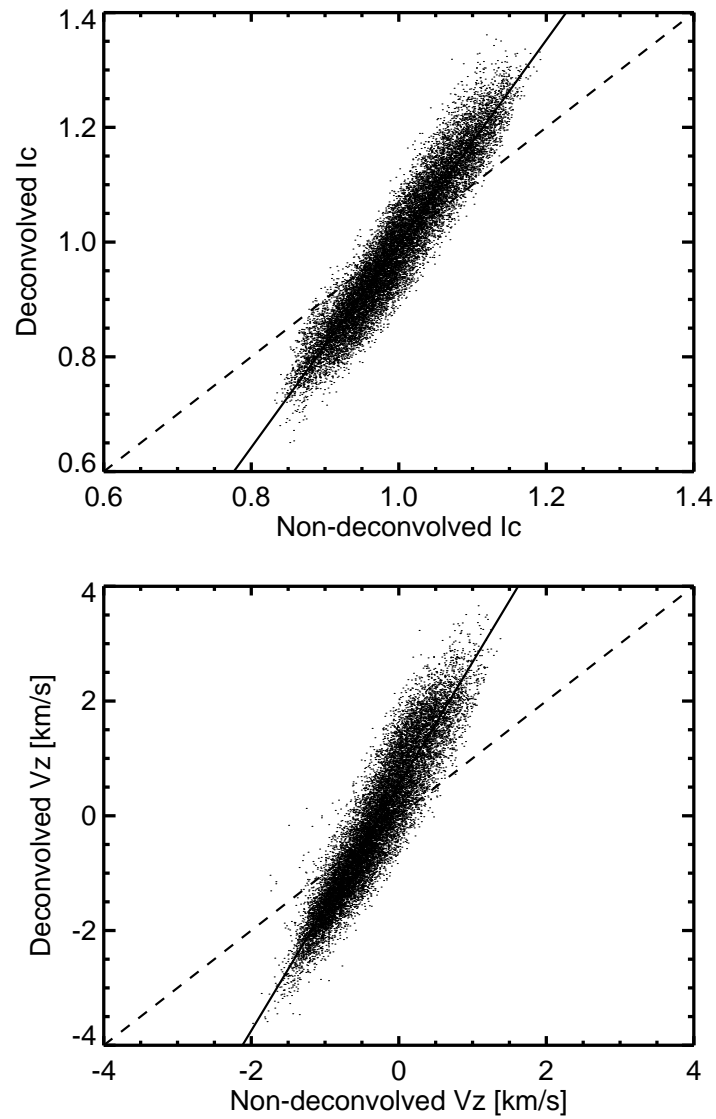
Figure 4.2: Upper panel: Scatter plot of the continuum intensity after deconvolution vs. that before deconvolution. Lower panel: the same for the LOS component of the convective velocity field at a bisector level of 0.70. Solid lines correspond to the best fitted line, and dashed lines indicate a slope of unity.

levels (geometrically higher layers), this shift by the deconvolution decreases, i.e., the first moments before and after the deconvolution are similar.

It should be noted that all the velocities are computed for the pixels in the center of the FOV, thus avoiding improperly deconvolved pixels close to the edges, as these need information outside the FOV.

4.1.3 Comparison with MHD simulations

For a direct comparison to the numerical simulations, we have to apply bisector analysis to the spectral profiles synthesized with the SPINOR code in the photospheric atmosphere computed by the MURaM code, because Doppler velocity fields obtained via bisector analysis are unavoidably smeared by the different atmospheric contribution along the LOS, previously described in Fig.3.9 (c), and thus the Doppler signals are smaller than the real velocity fields. Synthesized data with the rescaled spatial sampling to *Hinode* dataset ($\approx$100 km) and degraded data with the *Hinode*/SP PSF, correspond to the observation after and before the deconvolution, respectively. Fig.4.5 displays histograms of the resulting LOS velocity fields in the MHD simulation, facilitating us to compare the observational result of Fig.4.3. The amplitude of the convective velocity field in RMS at a bisector level of 0.70, decreases from 1.10 km/s before the convolution to 0.62 km/s after that, which is good agreement with the observational values of 1.12 km/s and 0.61 km/s, respectively. The LOS flows averaged over the entire FOV also indicate the same trend as the observations; the value goes from -0.11 km/s to -0.33 km/s. Note that these values are more blue-shifted than the observational values of -0.05 km/s and -0.21 km/s, respectively. The area fraction of downflows increases from 0.27 before the convolution to 0.46 after that; averaged speeds of up- and downflows are -1.06 km/s and +0.98 km/s before the convolution, getting reduced to -0.75 km/s and +0.51 km/s after that. These discriminated up- and downflow are defined in accordance with the same threshold ($\mp$0.18 km/s) as the observational one (see Section. 4.1). Thus, we conclude that numerical sim-
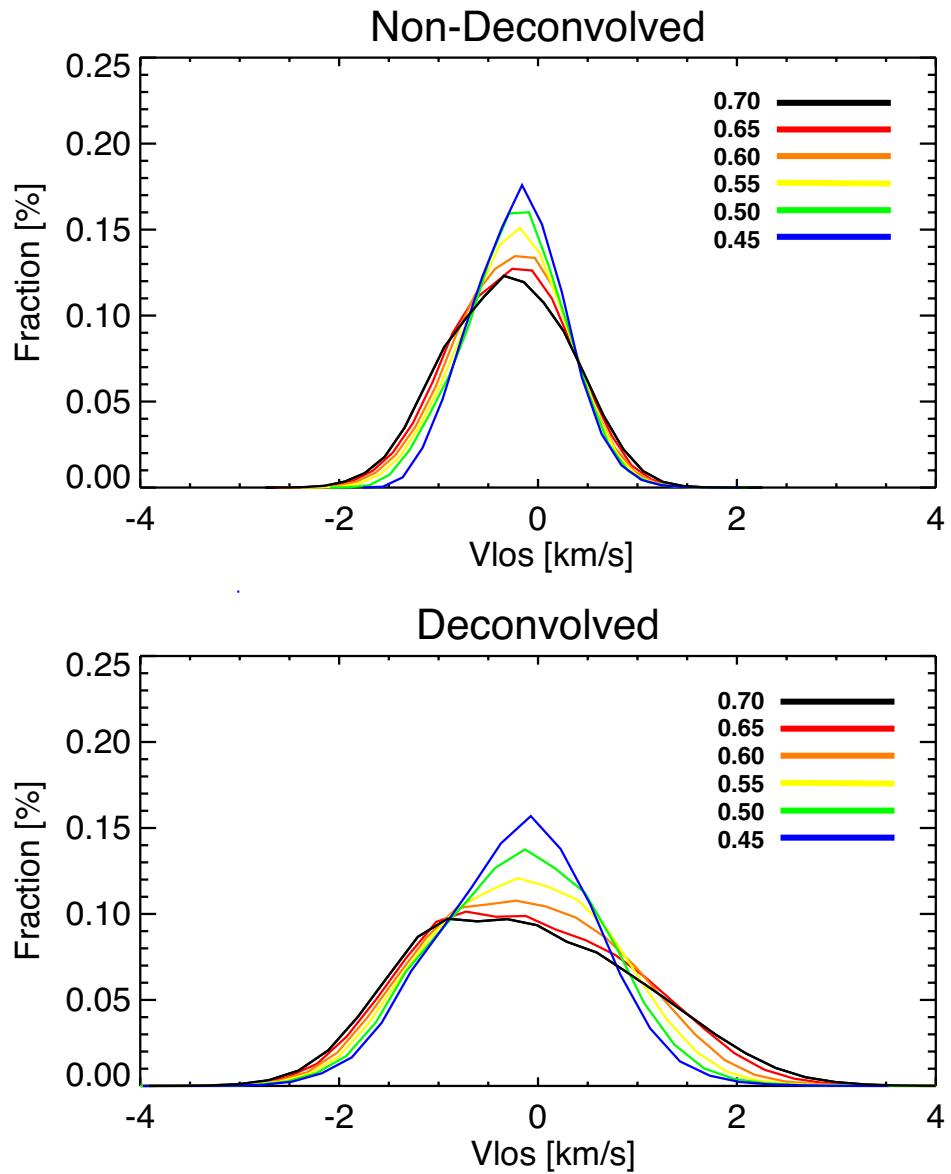
Figure 4.3: Histogram of the convective velocity field before the deconvolution (top) and after the deconvolution (bottom). The sign of the velocity has the same meaning as in Fig.4.2. The colors represent different bisector levels, listed in the upper right corners of the frames.
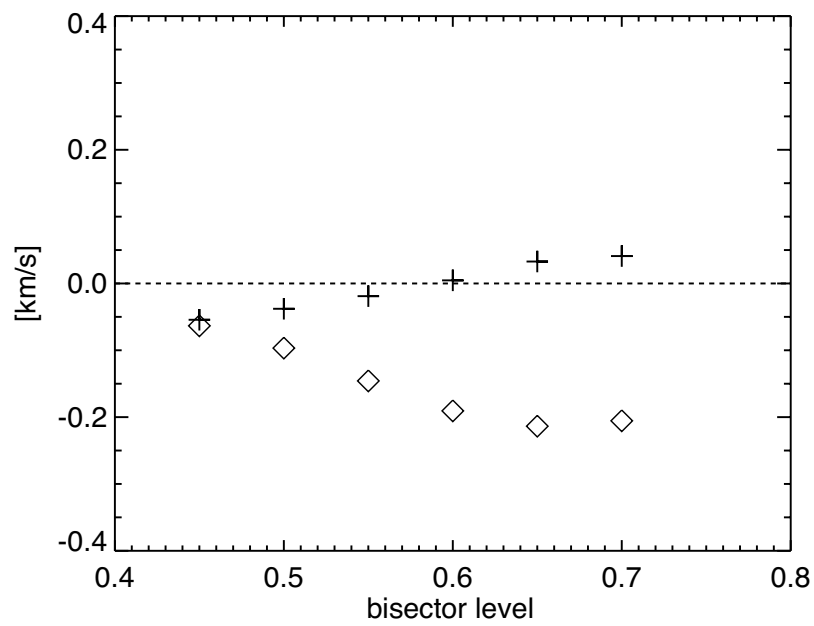
Figure 4.4: First moment of the convective velocity fields at the six bisector levels. Diamonds indicate the first-momentum of the velocity distribution before the deconvolution, whereas crosses represent it after the deconvolution.

ulation and the observation are good agreement in the up- and downflow relation and the amplitude, although slight differences still exist.
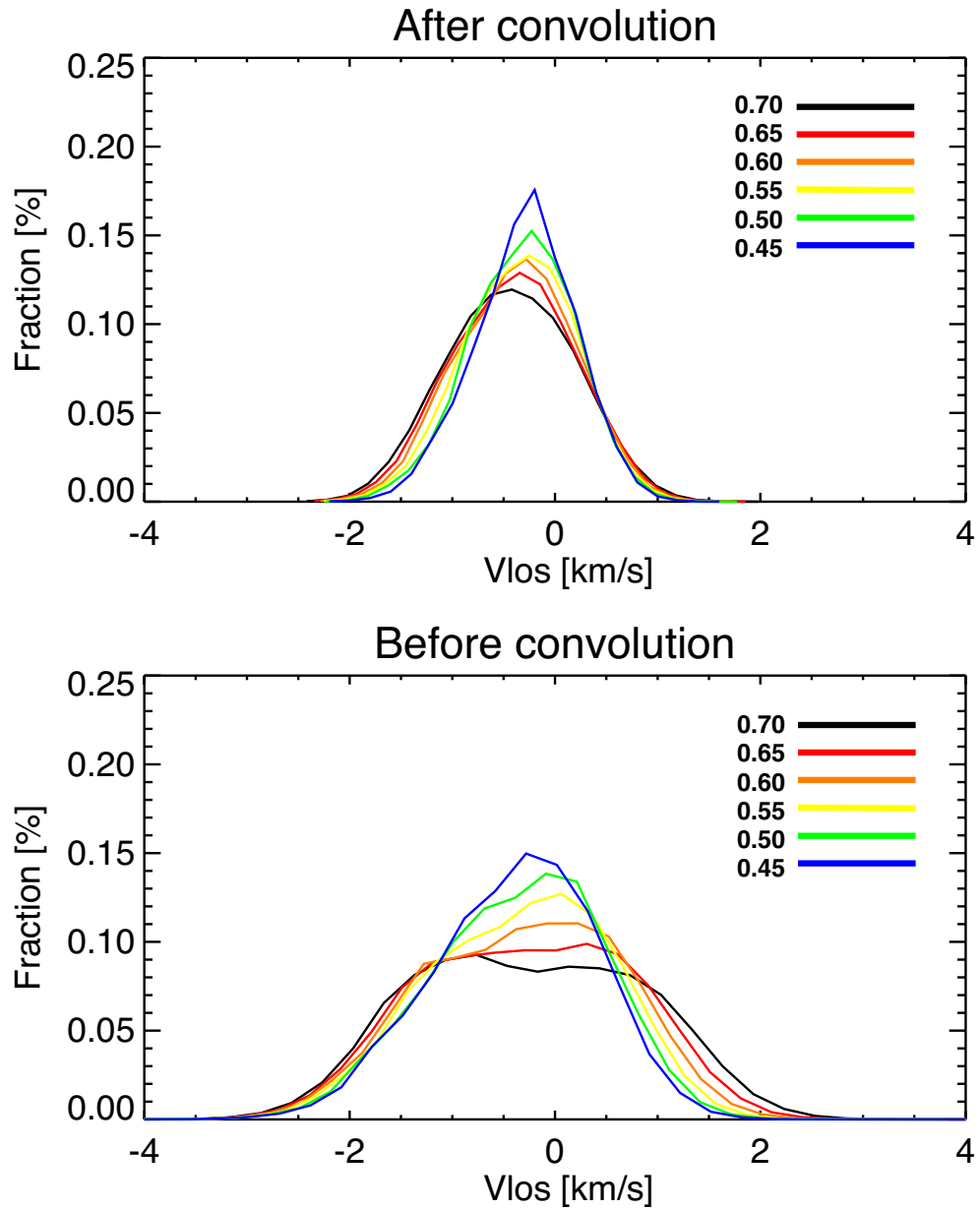
Figure 4.5: Histogram of the LOS velocity, derived via bisector analysis from spectral lines synthesized in the MHD simulation. Upper panel: after the convolution with the *Hinode* PSF. Bottom panel: before the convolution. Positive values correspond to downflows and negative values mean upflows. The colors depict the different bisector levels identified in the upper right corners of the frames. These levels are the same as in Fig.4.3.

4.2 Horizontal flows

First of all, we report the LOS velocity field variation from the solar center to limb. Fig. 4.6 represents snapshots of the continuum intensity (top panels) and the convective LOS velocity field at a bisector level of 0.45 (bottom panels), at the different angular distances of μ=1.0, 0.8, 0.6, 0.4 from left to right panels. The contrast of the LOS velocity fields is smallest at μ=1.0 and largest at μ=0.6, as seen in their RMS values of 0.79 and 1.09 km/s, respectively. As an angular distance μ decreases, the foreshortening effect conspicuously appears: granular shapes become compressed along the north-south direction while keeping a granular length along the east-west direction, leading to elliptical shapes in their appearance. In the LOS velocity fields map, we can find two characteristics along the south-north and east-west directions, respectively. Regarding the south-north direction, the front side of granules mostly displays strong blue-shifted signals, while the rear side does weak blue-shifted ones. This trend is seen in slices sandwiched by two arrows facing each other, indicated by a and b, plotted in the left panels in Fig.4.7. The continuum intensity is well-correlated with the LOS velocity fields, in accordance with the upflowing granule and downflowing intergranular lane. The peaks of the blue-shifted signals are offset from those of the continuum intensity toward the front side (i.e., the south side) of granules, particularly seen in 0.1-0.9 [Mm] and 1.4-2.0 [Mm] in *sample a*, particularly seen in 0.4-1.6 [Mm] *sample b*. The mentioned LOS difference between the south and north sides is good agreement with a granular radial flow (Fig.4.8a). From the inclined observer's angle, at the south side the LOS reflects horizontal flow directed toward an observer (i.e., blue-shifted), while at the north side it does horizontal flow directed toward the opposite side (i.e., red-shifted). Hence, the radial flowing produces the strong blue-shifted signal at the south side and the weak blue-shifted (or red-shifted) signal at the north side. On the other hand, the existence of azimuthal flow is implied by the spatial distribution of the LOS field along the east-west direction. In several parts of the FOV, adjoining granules along the east-west direction, the dark intergranular lane

sandwiched by these granules is filled with blue-shifted signal, as seen in the horizontal slices indicated by the arrows A and B in Fig.4.6, plotted in the right panels in Fig.4.7. The continuum intensity mismatches the LOS flow fields, e.g., 0.4-1.5 [Mm] in *sample A* and 1.5-2.0 [Mm] in *sample B*. This trend can be explained by granular azimuthal flow, because the LOS component at the west and east sides of a granule is perpendicular to the radial flow direction (Fig.4.8b). Other indications of the azimuthal flow are distributed over the FOV, e.g., blue-shifted patch around [1.3, 9.8] Mm in μ=0.8 map and [0.6, 5.6] Mm in μ=0.6 map. It is therefore from those spatial distributions that the LOS velocity fields in the granulation reflects not only radial flows but also azimuthal ones.

Fig.4.9 describes the obtained LOS velocity fields in RMS as a function of angular distance μ, identifying before deconvolution with blue and after it with red. From the disk center, the LOS amplitude monotonically increases (μ>0.6), and decreases toward the farther limb (μ<0.6). Recalling the explanation about the center-to-limb variation in section 3.5 facilitates us to understand this LOS amplitude variation, which is a net result of the following three factors: (a) different angle of the LOS component, (b) the foreshortening effect, and (c) the velocity field's gradient, see again Fig.3.9. Factor (a) is an essential to extract the horizontal flow component; Doppler signal at different angular distance μ reflects a gas motion along its own LOS to the solar surface, e.g., the horizontal flow appears at the limb and the vertical flow does at the disk center. Since the horizontal flows become faster than vertical ones as a consequence of the strong density stratification (Nordlund et al. 2009), larger Doppler shifts are expected at the limb observations. This effect can explain the increasing trend from the disk center toward the limb but until μ=0.6 in Fig.4.9. The other degradation factors (b) and (c) associated with limb observations become prominent enough to cancel the increasing trend by factor (a) at μ=0.6 and to overcome them in the farther limb (μ<0.6). These three factors characterize the curve variation of the LOS amplitude in Fig.4.9.

To derive the horizontal flow component, we have to carefully make a reasonable se-

Table 4.1: Best fitted horizontal flow amplitude in RMS [km/s]

bisector level (I/I_0)	angular distances (μ)			
	0.6-1.0	0.7-1.0	0.8-1.0	0.9-1.0
0.45	1.13	1.27	1.46	1.51
0.50	1.42	1.59	1.77	1.85
0.55	1.58	1.71	1.84	1.94
0.60	1.65	1.72	1.81	1.92
0.65	1.62	1.67	1.75	1.85
0.70	1.56	1.61	1.61	1.77

lection of which angular distances should be included into the model fitting (Eq.3.7). This fitted function should be applied to as many angular distances as possible but simultaneously under a large lack of the degradation factors (b) and (c). We accordingly use four different coverage of the angular distances, e.g., μ=0.6-1.0, 0.7-1.0, 0.8-1.0, and 0.9-1.0 by considering larger angular distances (μ>0.6) as being acceptable, because the decreasing trend toward the limb in the rest of distances (μ<0.6) are no longer subject to an increasing trend by factor (a). Fig.4.10 demonstrates one example of the reasonable fitting in the angular distances μ=0.6-1.0. With a combination of the six bisector levels and four fitted ranges, the resulting amplitudes are summarized in Table 4.1. When only higher angular coverage (e.g., μ=0.9-1.0) is processed into the fitting, then the amplitude typically results in higher value owing to less prominent degradations by the factors (b) and (c). The amplitude takes the maximum value of 1.94 km/s at a bisector level of 0.55, and it decreases monotically as a bisector level departs from that.

4.3 Three-dimensional structure of the convection

To construct the height structure of the velocity fields, horizontal and vertical flow amplitudes have to be derived at each spatial location from a granular center to an intergranular lane. The continuum intensity serves as a good proxy to reflect the granulation morphology, as identifying typically higher value with granules and lower one with intergranular
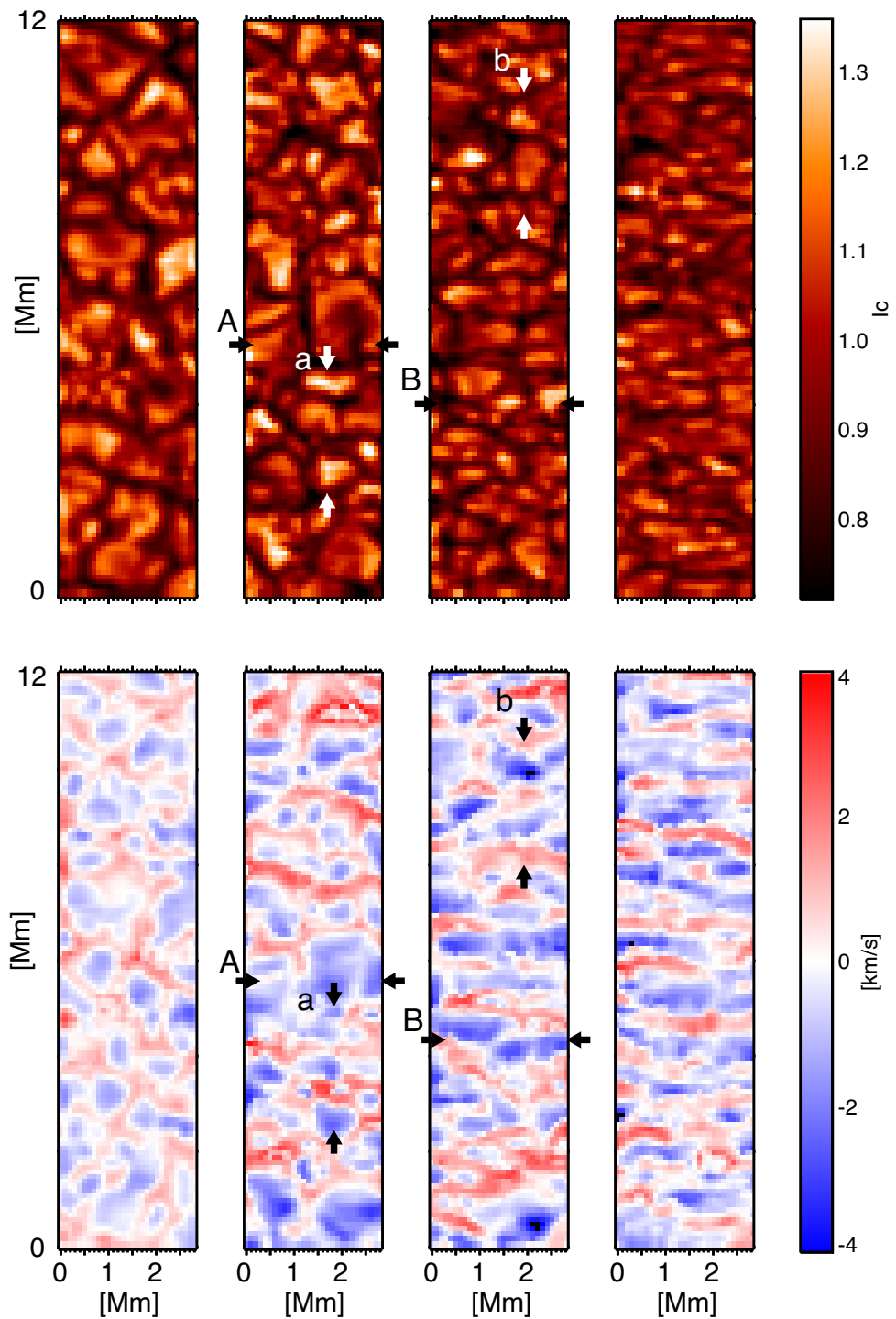
Figure 4.6: Snapshots of the continuum intensity (top panels) and the convective LOS velocity field at a bisector level of 0.45 (bottom panels), at the different angular distances of μ=1.0, 0.8, 0.6, and 0.4, from left to right panels. The two arrows facing each others mark the sample slice, shown later in Fig.4.7. Top and bottom panels are described with the identical color contrast, respectively.
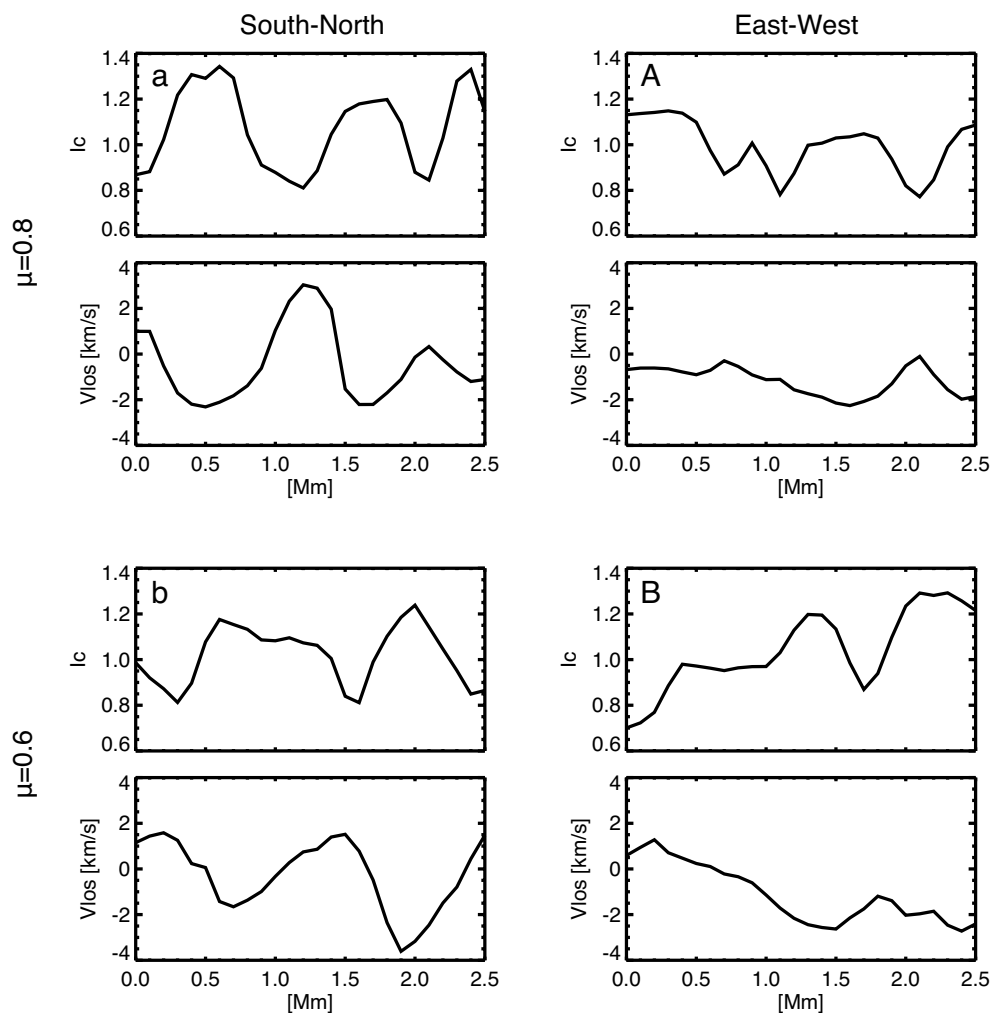
Figure 4.7: The continuum intensity and convective LOS velocity fields on the slices, indicated by two arrows facing each other in Fig.4.6 Those slices cut from south to north are plotted in *samples a* and *b* in the left panels, and from east to west are done in *samples A* and *B* in the right panels.
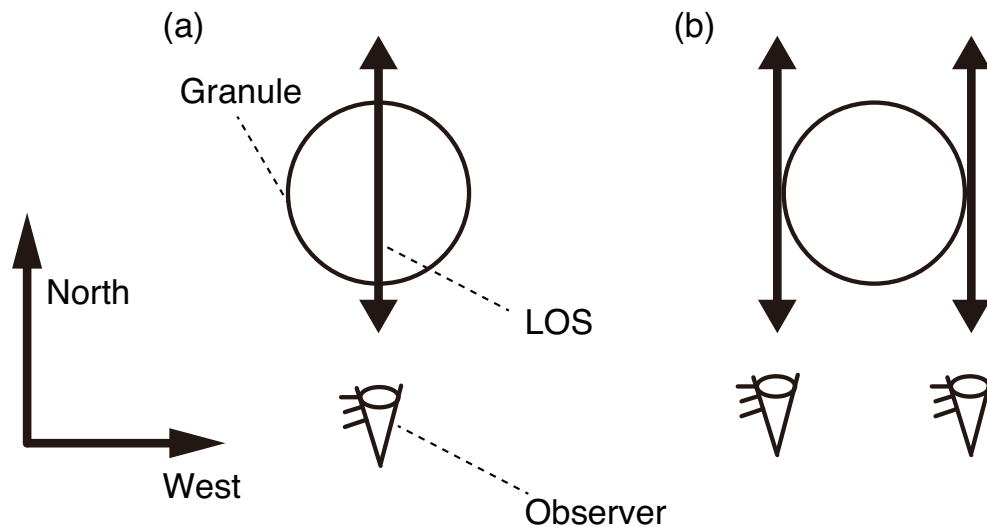
Figure 4.8: Simple cartoon for a better understanding of how radial and azimuthal flows are observed in a round-shaped granule at the north (or south) limb. (a) LOS direction at the granular center purely reflects a radial flow, which appears as blue-shifted signal at the front side and red-shifted signal at the rear side. (b) LOS direction at the east- and west-side edges of a granule is aligned with an azimuthal flow direction.

lanes. These spatial locations are segmented with a spacing of I_c=0.04 for the deconvolved continuum intensity. At each spatial location, for a derivation of the vertical flows, we simply sample the average LOS amplitudes in the disk center. For the horizontal flows, we follow the fitting approach in the same manner as introduced in section 4.2, but this fitting is applied to the center-to-limb variation at each spatial location. Fig.4.11 shows typical examples for a part of granular and intergranular regions, describing the LOS velocity fields as a function of heliocentric angle together with their own best-fitted curve. Intergranular lanes typically have larger LOS amplitude than granules, resulting in higher best-fitted values of v_h=1.47 km/s than granular one (1.21 km/s). Other center-to-limb variations at different spatial locations also behave like the aforementioned one including granules and intergranular lanes (Fig.4.9), in which the LOS amplitude increase until reaching μ=0.6. Hence we simply follow the same fitting process by adopting the four heliocentric angular coverage, e.g., μ=0.6-1.0, 0.7-1.0, 0.8-1.0, and 0.9-1.0. Finally, horizontal flow speed at each location is derived by averaging the four best-fitted values
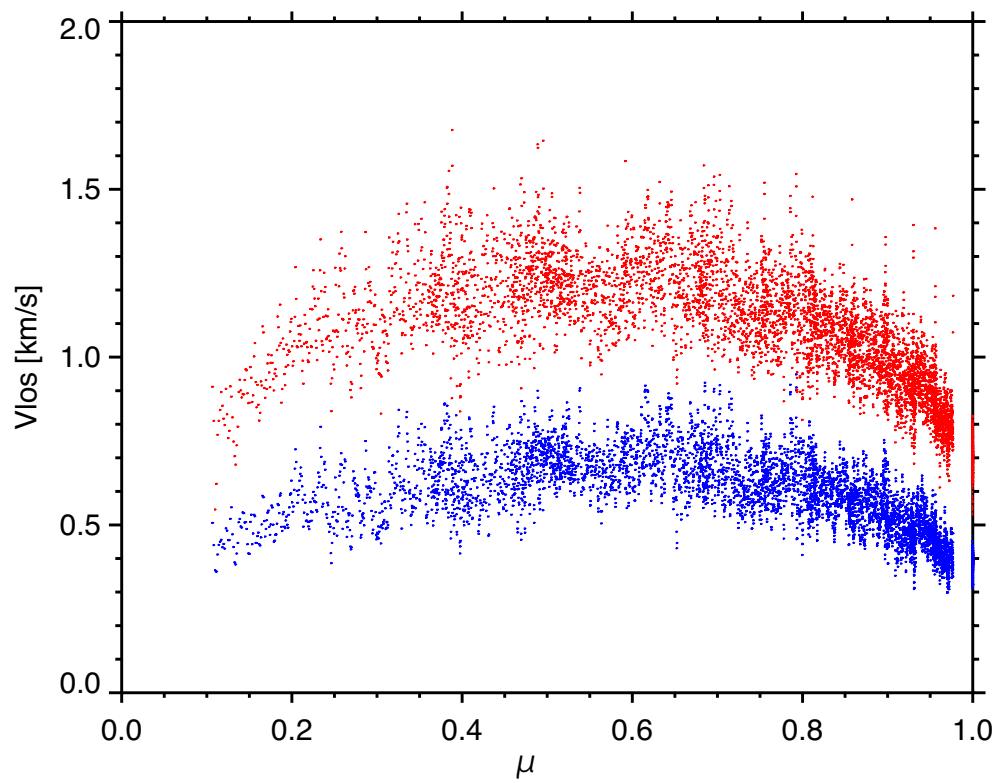
Figure 4.9: Center-to-limb variation of the LOS velocity fields in RMS at a bisector level of 0.70 (at the highest layer). Red color identifies the one after deconvolution, and blue does before deconvolution.
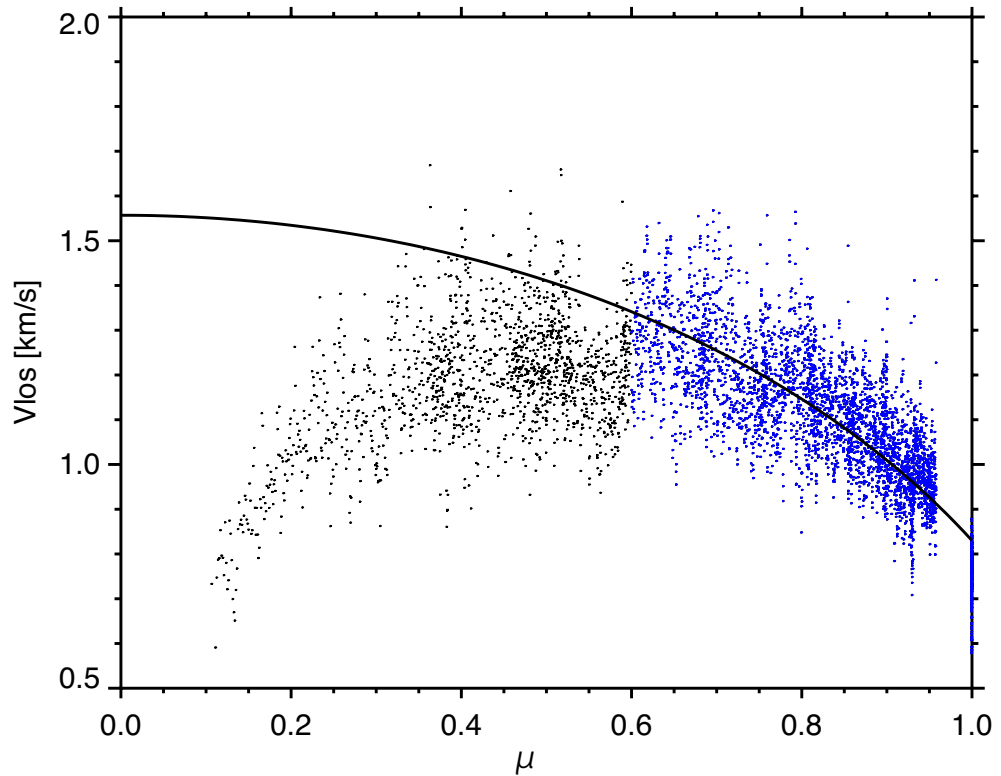
Figure 4.10: Center-to-limb variation of the LOS velocity fields at a bisector level of 0.70 (at the highest layer). The best-fitted one is shown as a black solid curve, adopting $v_{hor,rms}$ of 1.56 km/s. Note that the LOS velocity fields at less than μ=0.6 (depicted in black dot) are discarded for this fitting so that the model fairly accounts for the center-to-limb variation over the rest of angular distances (depicted in blue dot).

which results from the above heliocentric angular coverage. Fig.4.12 provides the obtained height structure of vertical and horizontal flow amplitudes. The maximum flow speed is located in I_c=0.88, and the amplitude decreases monotonically toward both sides of bright granules and dark intergranular lanes. In the outside locations (i.e., a particularly dark region of I_c <0.76 or bright region of I_c >1.22), the horizontal flow amplitude cannot be sampled. This is because the granulation contrast decreases with increasing geometrical height as proceeding toward the limb. Fig.4.12 depicts the samplings until relatively dark region I_c=0.74, but the samplings at a bisector level of 0.70 and I_c=0.74-0.86 are untrust-worthy owing to the same reason. Note that we normalize I_c by averaging over the entire FOV in each dataset, in order to correct for the monotonic decrease of the continuum intensity toward the solar limb, known as the *limb darkening effect* (Stix 2004).

To see how the derived velocity structure changes when inadequate spatial resolution adopted, the same processing is also applied to the observation before deconvolution, but with an I_c spacing changed from 0.04 to 0.022 (Fig.4.13). We derived the latter spacing value (0.022) from the original spacing 0.04 divided by 1.78 which is a slope of the scatter plot for the continuum intensity between before and after deconvolution (Fig.4.2) so that the segmented locations before and after it should be minimally departed from each other. As expected, the deconvolution processing significantly increases the amplitudes for both vertical and horizontal flows by a factor of roughly two. There is no remarkable shift of the boundary between up- and downflow before and after deconvolution, as located at I_c=0.96 and 0.98, respectively. The most striking change is that the location of the fastest horizontal flow is shifted toward darker intergranular lanes, from I_c=1.00 before deconvolution to I_c=0.88 after it. Irrespective of our selection of which μ range (e.g., μ=0.6-1.0, 0.7-1.0, 0.8-1.0, and 0.9-1.0) is adopted to the fitting, the resulting horizontal flows reaches the maximum speed at the same location (i.e., I_c=0.88).

In more facilitating way to envision the convective structure combined with the vertical and horizontal flows, Fig.4.14 depicts flow speeds with an arrow length by a square root
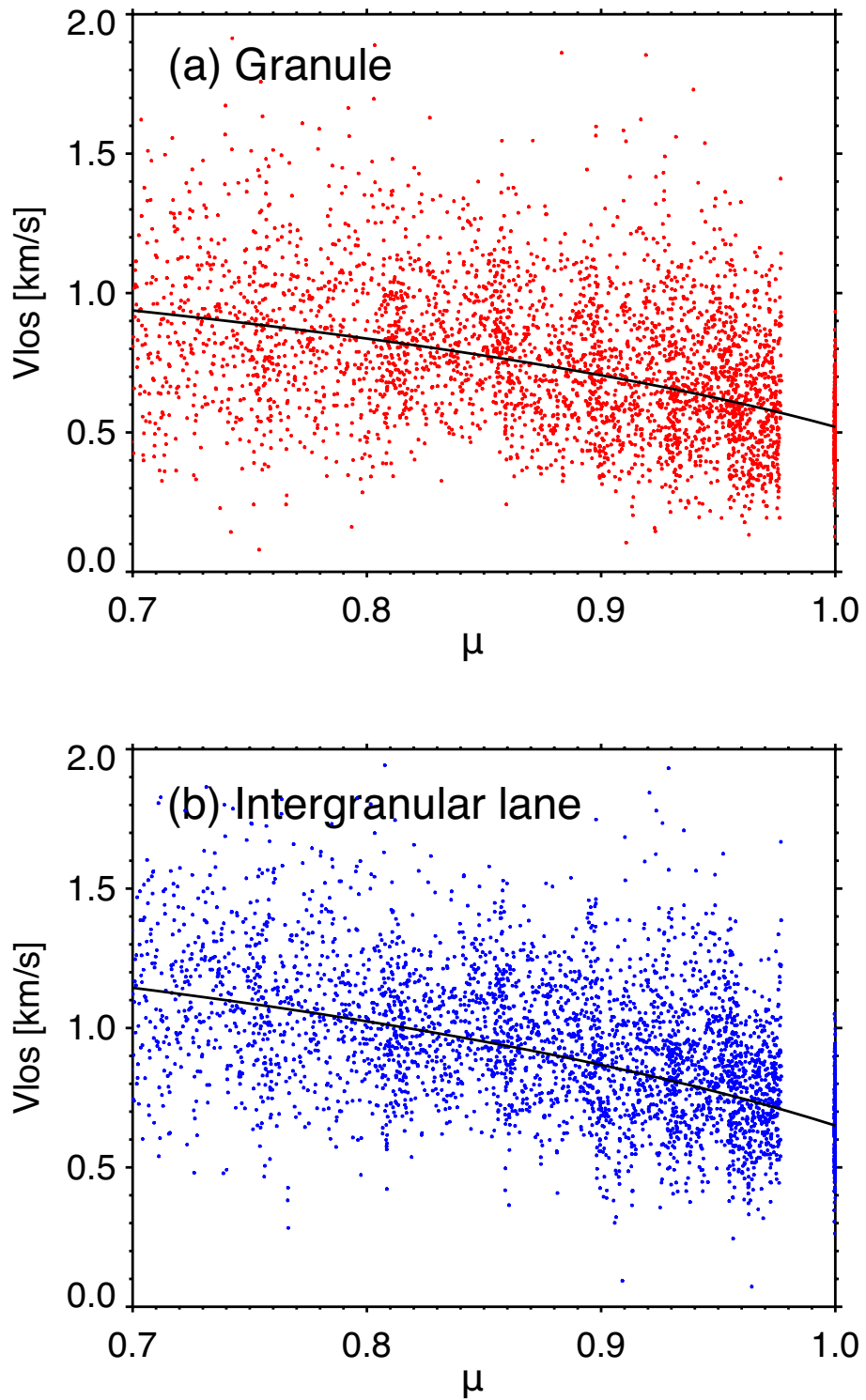
Figure 4.11: LOS velocity fields in RMS as a function of angular distance from μ=0.700 to μ=0.977 and discretely around μ=1.000, at a geometrical height of 62 km. Panel (a) represents a granular region (I_c=1.14-1.18) and a fitted solid curve with $v_h = 1.21$ km/s. Panel (b) shows a intergranular region (I_c=0.86-0.90) and the curve with $v_h = 1.47$ km/s.
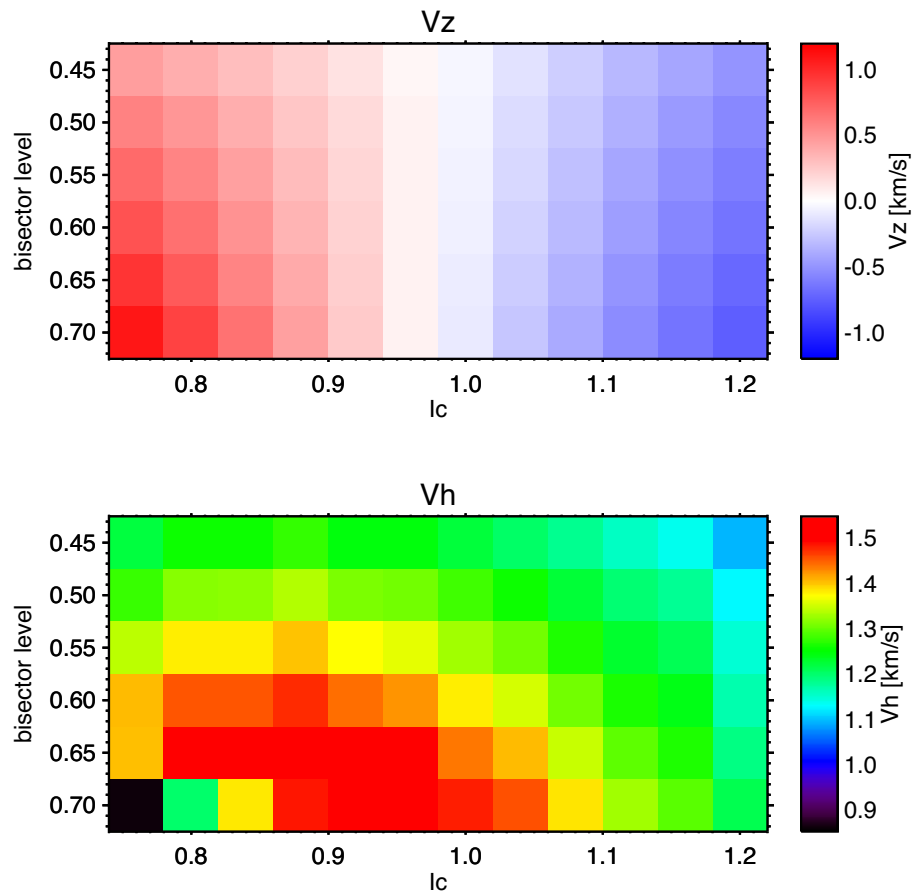
Figure 4.12: Height structure of the average vertical flow speed in top panel and of the horizontal one in RMS in bottom panel, derived with deconvolution. Samplings at a bisector level of 0.70 and I_c=0.74-0.86 are untrustworthy.
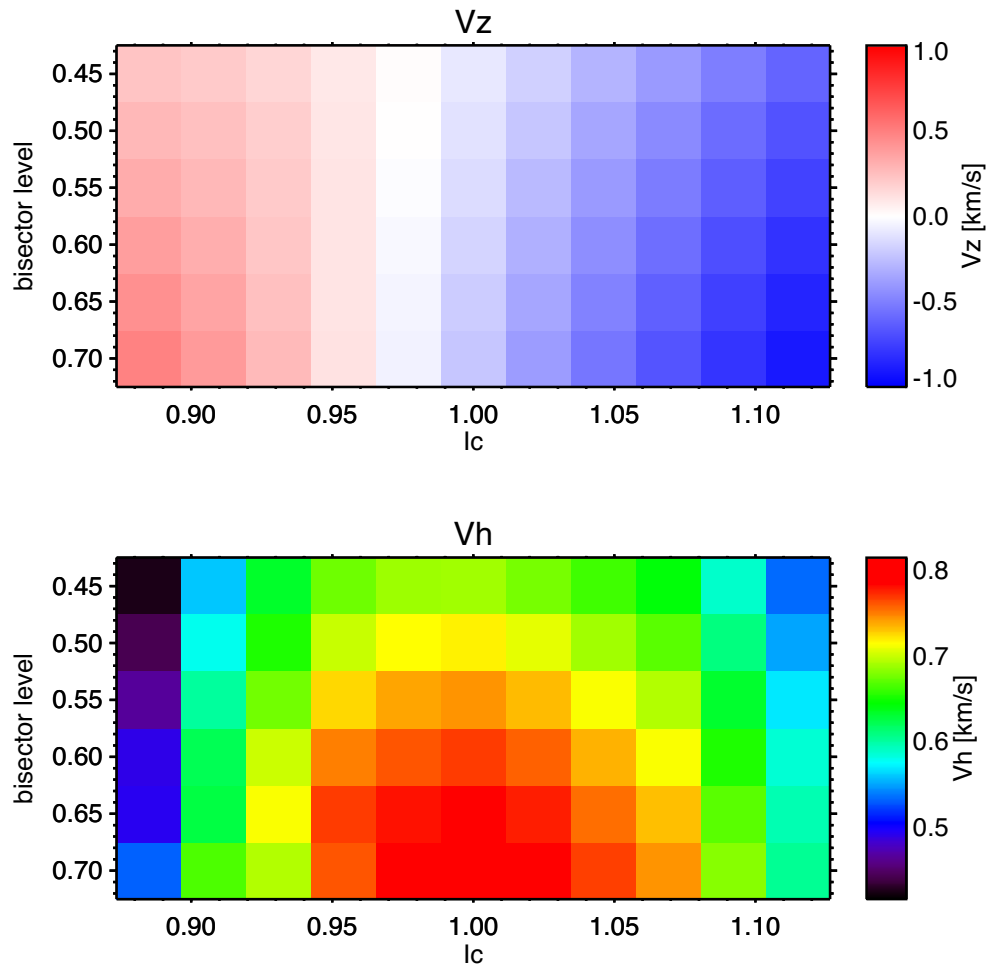
Figure 4.13: The same representation as Fig.4.12, except for those amplitudes derived without deconvolution. Sampling at the entire bisector levels with intergranular side of less than I_c=0.9 are untrustworthy.

of both horizontal and vertical flows, i.e., $\sqrt{v_h^2 + v_z^2}$, derived with the deconvolution processing. In this figure, as if observed from all the angles, we simply copied the half-side of the divergent flows into the other side, as we actually observed the radial divergent flow in Figs.4.6 and 4.7. As denoted at the top-edge of the panel in this figure, the segmentation boundary between the granular and intergranular regions, I_c=0.98, is based on the sign of the average vertical flow in each continuum intensity. Note that the LOS fields cannot be sampled at the core sides of intergranular lanes (I_c<0.76) and granules (I_c>1.22), and at a bisector level of 0.70 and I_c=0.74-0.86. It should be emphasized here that this view is compulsorily projected on the paper's plane as a two-dimensional cut of a granule, while some existence of azimuthal flows (i.e., a perpendicular direction to the paper surface) are indicated by Figs.4.6 and 4.7.
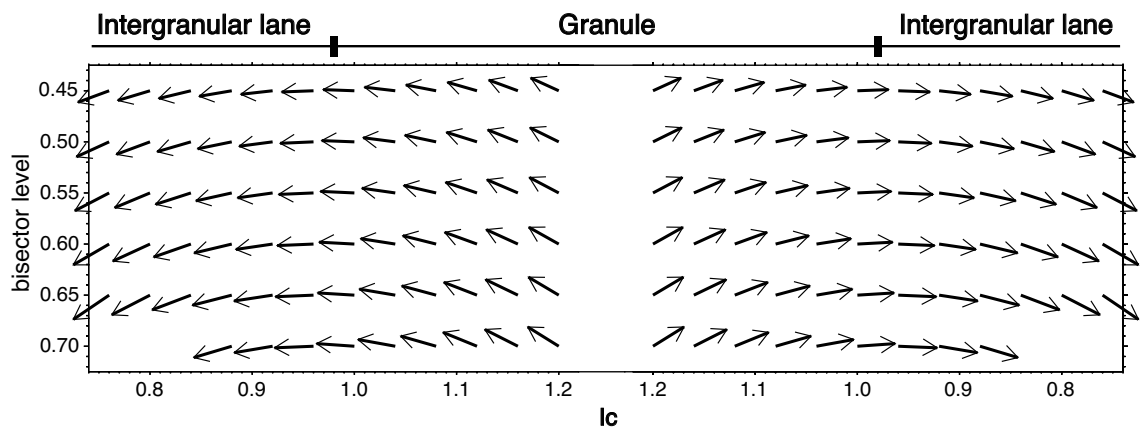
Figure 4.14: Three-dimensional convective velocity fields, derived with deconvolution. Horizontal axis represents the continuum intensity as a spatial location segmented with an I_c=0.04; the inner side (I_c>0.98) identifies granules and the outer side (I_c<0.98) does intergranular lanes, separated by the boundary between up- and downflow. Vertical axis means the bisector intensity level. The arrow length represents the flow speed defined as $\sqrt{v_h^2 + v_z^2}$, normalized by a maximum amplitude of 1.81 km/s.

Chapter 5

Discussions

On the bass of our results, we discuss implication on the photospheric convection in section 5.1. In more detail, this chapter divides the discussion about vertical flow derived from the disk center to section 5.1.1 and horizontal flow from the center-to-limb variation of the LOS velocity fields to section 5.1.2, and their three-dimensional structure to section 5.1.3. Beyond the discussion about the photospheric convection itself, possible applications to the coronal heating problem are discussed in section 5.2.

5.1 Photospheric convection

5.1.1 Vertical flow

Our main findings explained in section 4.1 are summarized as follows. The convective velocity amplitude ranges from -3.0 km/s to +3.0 km/s after the deconvolution while it does from -2.0 km/s to +1.5 km/s before it. The flow speeds averaged over the entire FOV after the deconvolution lay within ±0.05 km/s at all the bisector levels, compared with an offset of up to -0.2 km/s before it.

First of all, we discuss why downflows is preferentially enhanced through deconvolution.

This would be due to differences in the emergent intensity between granules and intergranular lanes. Convective blue- and red-shifted signals within a sub-arcsec spatial scale are unavoidably mixed because of the imperfection of the imaging performance of a telescope. Consequently, they partially cancel each other, leading to spatially degraded image. More light from brighter granules is scattered into darker intergranular lanes than the other way around. A spectral line profile from granule is blue-shifted, which reduces redshifted signal of intergranular lane. This effect is larger than the decrease in the blueshift coming from granules, due to the smaller amount of stray light from intergranules, so that finally the downflows are decreased more strongly than the upflows. Our deconvolution successfully compensates for both intrusions in granules and intergranular lanes each other, so that downflows are more strongly enhanced than upflows. The magnitude relation between up- and downflows is remarkably changed from the previously reported relation of stronger upflows and weaker downflows (Yu et al. 2011a; Jin et al. 2009; Oba et al. 2017) to almost comparable (the downflows speed on average is slightly faster).

Besides, we detected that the effect of the deconvolution process on the convective motions is height dependent; at the higher layers, the changes through the deconvolution process are less prominent. We believe that the reason behind this behavior is the photospheric temperature stratification, in which, towards higher layers, the intensity contrast of the granulation becomes smaller and eventually reverses, i.e., *reversed granulation* is seen. In this layer, dark blue-shifted granules are surrounded by bright red-shifted intergranular lanes (Kostik et al. 2009). The transition from the normal granulation to the reversed one occurs at 130-140 km found in the numerical simulation (Wedemeyer et al. 2004; Cheung et al. 2007) and at 140 km in an observational work (Ruiz Cobo et al. 1996). One of our bisector levels (i.e., a geometrical height of 135 km) corresponds to this transition height. At this height, the LOS speeds averaged over the entire FOV before and after the deconvolution show no significant difference (Fig.4.4), which is consistent with this temperature stratification because the intensity from granules and intergranular

lanes should be almost identical.

We found the effect of the deconvolution on the observational data is similar in magnitude as the changes introduced by convolving the data from the MHD simulations. In Fig.4.3 for the observation and Fig.4.5 for the numerical simulation, small differences, e.g., in the exact shape of the velocity histograms are present between simulations and observations, but these are minor compared with the surprisingly good agreement. This good agreement between the observation and the numerical simulation indicates that *Hinode* fairly resolves granular and intergranular tiny structures, and the MURaM simulation reproduces the realistic solar granulation.

The deconvolution either turns some weak upflows mainly at the boundaries of granules downflows, or brings to light usually narrow downflow lanes that are not visible before it. By revealing such a tiny scale of downflow structure, deconvolution technique will provide new insights into magneto-convection by allowing to observed the immediate surroundings of small flux tubes, preferentially located in intergranular lanes (Title et al. 1987; Grossmann-Doerth et al. 1988; Solanki 1989). This should enable the magnetic features to be better probed, e.g., as done by Domínguez Cerdeña et al. (2003) and Buehler et al. (2015) using complementary approaches. Possible future applications of deconvolution include catching the detailed process of *convective collapse*, which coincides with a downflow in magnetic flux tubes (Parker 1978), as observed by Nagata et al. (2008), Requerey et al. (2014), Bellot Rubio et al. (2001), and Fischer et al. (2009), and described using MHD simulations by Danilovic et al. (2010), or the magneto-acoustic waves generated intermittently in flux tubes (e.g., Stangalini et al. 2014), which are excited by the surrounding convective motions (Kato et al. 2016).

5.1.2   Horizontal flow

As explained in section 4.2, our deconvolution provides the remarkably enhanced amplitude of the LOS velocity fields over the solar center-to-limb. Here we take the highest amplitude result at the bisector level of 0.55, and the LOS amplitude in RMS monotonically increases from 0.9 km/s at μ=1.0 to 1.5 km/s at μ=0.6. Horizontal flow of 1.6 km/s matches the mentioned center-to-limb variation, while a reasonable speed increases as higher μ range is only considered, e.g., the maximum speed is 1.9 km/s for μ=0.9-1.0.

First of all, let us compare the LOS amplitude variation with those in the past works (Keil & Canfield 1978; Mattig et al. 1981; Nesis & Mattig 1989). As summarized in Fig.5.1, their highest amplitudes peak at μ=0.6-0.8, while their observations were performed at discrete angular distances. Our maximum amplitude (1.5 km/s at μ=0.6) highly exceeds their maximum ones (0.4-0.6 km/s). This fact implies that our spectral data reflects the fairly resolved granulation even far from the disk center, by relaxing the foreshortening degradation via the deconvolution process.

On the other hand, their estimations of the horizontal flow amplitude largely differ from each other, although their LOS amplitude variations are comparable among them as seen in Fig.5.1. Keil & Canfield (1978) reported $\approx$ 2.0 km/s, challengingly compensating for the foreshortening degradation. However, even with higher spatial resolution observed by the balloon-borne 30 cm telescope (Mehltretter 1978) under the almost lack of the atmospheric seeing degradation, Mattig et al. (1981) estimated the flow speed of being 0.5-0.7 km/s in RMS, and later Nesis & Mattig (1989) concluded a typical value of being 0.4 km/s. Thus, such an almost one order difference among their resulting amplitudes implies that the horizontal flow speed heavily depends on their own approach. Our results without any consideration for the foreshortening degradation, but with the spatially well-resolved data, strongly indicate the large amplitude (e.g., 1.6-1.9 km/s). If we appropriately corrected for the degradation effects, the horizontal flow amplitude would become still larger.
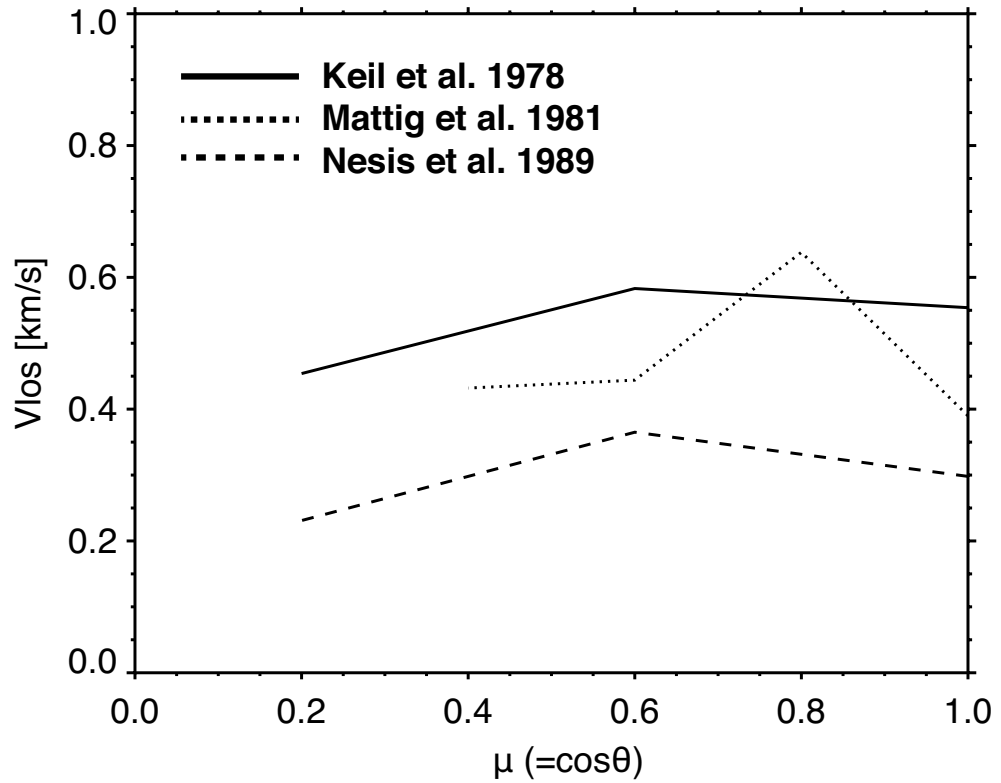
Figure 5.1: Convective velocity fields as a function of angular distance, reported in the past works (Keil & Canfield 1978; Mattig et al. 1981; Nesis & Mattig 1989). Used spectral lines for a Doppler calculation are chosen so that their corresponding geometrical heights are almost equivalent to that of our spectral line.

Next, we compare our estimation of the horizontal flow amplitude with those obtained by feature tracking techniques (Table 5.1). The amplitude values obtained in this work are the largest, sometimes by a factor of two. This means that the amplitude derived with feature tracking techniques is indeed underestimated, which is well compatible with the warning addressed by Verma et al. (2013). If our derivation also compensated for the foreshortening degradation, the resulting amplitude would approach three times larger values than those derived with a feature tracking technique, according to the estimation in Verma et al. (2013).

Therefore, our work imprints the importance of using the Doppler calculation with high spatial resolution in deriving the horizontal velocity field. During the last decade, a feature tracking technique has been used preferably thanks to its lower demand for

Table 5.1: Reported amplitudes of horizontal flows with feature tracking techniques and with our method

Paper	Reported amplitude
November & Simon (1988)	0.5-1.0 km/s
Brandt et al. (1988)	0.67 km/s
Title et al. (1989)	0.37 km/s
Berger et al. (1998)	1.1 km/s
Shine et al. (2000)	0.49 km/s
Müller et al. (2001)	0.6 km/s
Matsumoto & Kitai (2010)	1.1 km/s
Verma & Denker (2011)	0.54 km/s
Chitta et al. (2012)	1.3 km/s
Our result	1.6-1.9 km/s

the current observations. The resulting amplitudes have overcome those derived by the Doppler calculation with low spatial resolution. However, this technique can track only distinctive granular shapes, and is not sensitive to gas flowing in intergranular lanes. This limitation would prohibit the resulting amplitude from drastically increasing even with higher spatial resolution achieved in the future, as seen a minor improvement in the past literature (in Table 5.1). Our work could firstly led to larger amplitude than those with a feature tracking technique; it implies that our approach successfully extracts considerable amount of kinetic energy deposited in the intergranular flows that are elusive to the tracking techniques. Furthermore, the Doppler diagnosis becomes a more promising to investigate the horizontal flow, because higher spatial resolution directly improves the amplitude as a telescope aperture's diameter increases.

5.1.3   Three-dimensional structure of the convection

Our study describes the three-dimensional photospheric convection, derived with the Doppler calculation for the first time. Past observational works (Ichimoto et al. 1989 and Ruiz Cobo et al. 1996) similarly described the height structure of the horizontal flow fields, but derived indirectly from the vertical flow fields with mass balance held, i.e.,

div(ρv)=0. Fig.5.2 summarizes our findings noted in section 4.3. Our result not only improves the amplitude and provides the almost identical magnitude relation between up- and downflow (see section 5.1.2 and 5.1.3), but also incorporates new information about the spatial distribution of the horizontal flow into our understanding.

Here we discuss the sequential phases (a) and (b) in the bottom panel, where the boundary between granular upflow and intergranular downflow exists and the horizontal flow reaches the maximum speed, respectively. The phase (a) location (i.e., I_c= 0.96) in our study is almost compatible with the I_c=1.00 as the widespread use of a boundary to separate granules from intergranular lanes (e.g., Hanslmeier et al. 2000; Bello González et al. 2010; Abramenko et al. 2012). This boundary is considered as a bending location of vertical flow, where the material's flow changes their traveling direction from up- to downward (Khomenko et al. 2010). In this study, we separate intergranular lanes from granules by following a straightforward threshold with the up- and downflow boundary (i.e., I_c=0.96). The positional relation between the phases (a) and (b), i.e., at I_c= 0.96 and 0.88, respectively, indicates the following convection process: even after passing through that boundary (after turning into downflows), a flowing parcel still continues to experience a pressure gradient force directed from granules to intergranular lanes, leading to the fastest horizontal flows in intergranular lanes, and subsequently the parcel suddenly decelerates as it proceeds toward farther intergranular lanes. This pressure gradient force toward outside the granule would be created by the strong stratified atmosphere, made by radiative energy loss, which sweeps the upwelling gas into the horizontal directions (Nordlund et al. 2009).

This scenario is also supported by a fairly good agreement with a numerical simulation in Fig.5.3. Panel (a) is a continuum intensity map calculated under the same setup as Fig.3.4 (a). Panel (b) represents horizontal flow speeds calculated as a square root of both horizontal direction's ones, i.e., $\sqrt{v_x^2 + v_y^2}$, at a geometrical height of 62 km. Note that these horizontal flows are simulated value in the synthesized numerical cube (not the
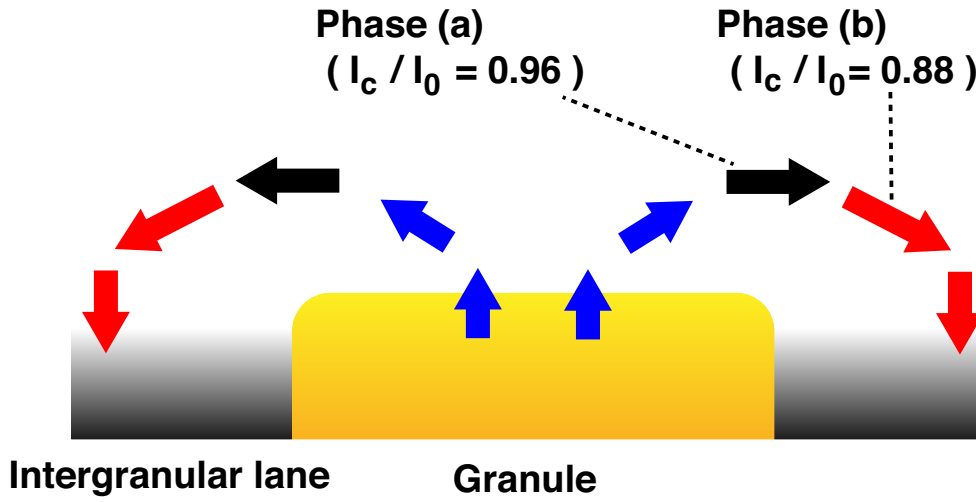
Figure 5.2: Schematic view of our comprehension of the granulation, where the arrow length means relative flow speed. The obtained view of the granulation. The amplitude relation of up- and downflows is changed to the almost comparable. The horizontal flow sequence is newly incorporated to the granulation scenario; after passing through the boundary between the granule and intergranular lane at $I_c = 0.96$ (phase:a), horizontal flow reaches the maximum speed at $I_c = 0.88$ (phase:b).

Doppler calculation). Panels (a) and (b) indicate that centers of a granule correspond to slower horizontal flows, while intergranular lanes favor the faster flows as well as slower ones. Panel (c) facilitates to confirm this spatial relation by representing a scatter plot between the continuum intensity and the horizontal flow speed. Panel (d) segments the flows speeds in RMS with a spacing of $I_c=0.04$ for a direct comparison with the observation. It is clear from Panel (d) that the horizontal flow attains the maximum speed at $I_c=0.92$. The locations of this maximum speed are identical at all the other heights from 49 km to 135 km. This location is well consistent with our observational result ($I_c=0.88$).

It should be reemphasized here that our view of the slice of the granulation (Fig.4.14 and 5.2) is compulsorily projected on the two-dimensional plane at the paper's convenience, while some existence of azimuthal flows (i.e., a perpendicular direction to the paper surface) are indicated by Figs.4.6 and 4.7. In the actual granulation, intricate flowing gas in junctions interacts with each other, thereby possibly yielding an azimuthal stream as seen

in Figs.4.6 and 4.7. In contrast to the limited observational approach, the numerical sim-
ulation can be a rough indication to confirm the existence of the azimuthal flows, as seen
in Fig.5.4. Panels (a) and (b) show the continuum intensity (I_c), and overplot the vectors
of horizontal flow field, v_h, and gradient of I_c, $grad(I_c)$, respectively. Panels (c) depicts a
scatter plot of I_c versus a direction deviation, defined by $\Delta\phi = \phi_{v_h} - \phi_{grad(I_c)}$, where ϕ_{v_h}
and $\phi_{grad(I_c)}$ are vector directions of v_h and $grad(I_c)$, respectively. The distribution of $\Delta\phi$
are concentrated around 0 degree, indicating that the horizontal flow is well-aligned with
a gradient of the continuum intensity. The deviation direction are conspicuously scattered
in the lower and higher continuum intensity. This spatial dependence is clearly seen in
panel (d), where the deviation $\Delta\phi$ is plotted in RMS as a function of I_c segmented with
a spacing of 0.05. Thus, the numerical simulation indicates that horizontal flow direction
is typically aligned with the radial direction from a granular center while azimuthal flow
is also distributed, especially dark intergranular lanes and bright granules. This is a sup-
portive result of the existence of azimuthal flows in the actual granulation, some of which
would appear in the limb observation (Figs.4.6 and 4.7).

   In deriving the three dimensional convective velocity fields, one caution is should be
stressed here that our amplitude consists of not only the granulation flow, but also the
advected motion by the larger scale convection, e.g., *supergranulation* with a typical scale
of 30 Mm. This advected flow is reported to have 0.3 km/s in RMS (Hathaway et al.
2002; Rieutord & Rincon 2010), which should not be completely negligible but signifi-
cantly smaller than the granulation flow. Thus, the supergranulation would be one of
the causes of the scatter in the LOS amplitude variation along the center-to-limb (e.g.,
Fig. 4.9). Our derivation uses the wide fitting range, e.g., μ=0.6-1.0, corresponding to a
spatial scale of 300 Mm, which is ten times larger than that of the supergranulation. As a
result, the averaging over a few to tens of the supergranulation suppresses the fluctuation
in the derived horizontal flow amplitude.

   It should be stressed here that the mentioned findings are thanks to using the Doppler

diagnostic approach with the instrumental scattered light corrected. As an alternative approach, a feature tracking technique works well in deriving large scale flows of granules but it is insensitivity to small scale flows of intergranular lanes (Verma et al. 2013; Yelles Chaouche et al. 2014; Louis et al. 2015). Neither, if the spatial resolution is not adequate, the Doppler diagnostic cannot lead to our discovery about the horizontal flow sequence in intergranular lane. This is evident from the other result without the deconvolution (Fig.4.13), in which the fastest horizontal flow happens inside a granule. Therefore, our approach is a straightforward diagnostic tool by recording purely gas motion into the LOS component, and successfully extracts this spatial distribution of the horizontal flow.

In summary, while intergranular lanes have been simply thought to be a downflow region owing to a lack of a suitable diagnostic tool to see the horizontal flow there, we discovered the highly dynamic horizontal flow sequence in intergranular lanes, where the flow reaches the fastest speed and subsequently experiences a sudden breaking.

5.2 Energy transfer to the upper atmosphere

The coronal heating is one of the biggest problems in the astrophysics (see Parnell & De Moortel 2012 for a review). Here we describe implications for the heating problem, on the basis of our findings.

First of all, we compare our horizontal amplitude with those required as a photospheric footpoint motion for many of the preexisting heating models (Kudoh & Shibata 1999; Moriyasu et al. 2004; Suzuki & Inutsuka 2006; Antolin et al. 2008; van Ballegooijen et al. 2011; Asgari-Targhi & van Ballegooijen 2012), in which the amplitude is served as a boundary condition. Table 5.2 summarizes the required values in each model for heating the corona onto one-million degree. Reported prior to our study as summarized in Table 5.1, the horizontal amplitudes support or refuse some of the heating models, and cannot exceed the highest requirement of 1.5 km/s in RMS by van Ballegooijen et al. (2011) and Asgari-Targhi & van Ballegooijen (2012). Our finding value ($\approx$1.9 km/s) highly exceeds
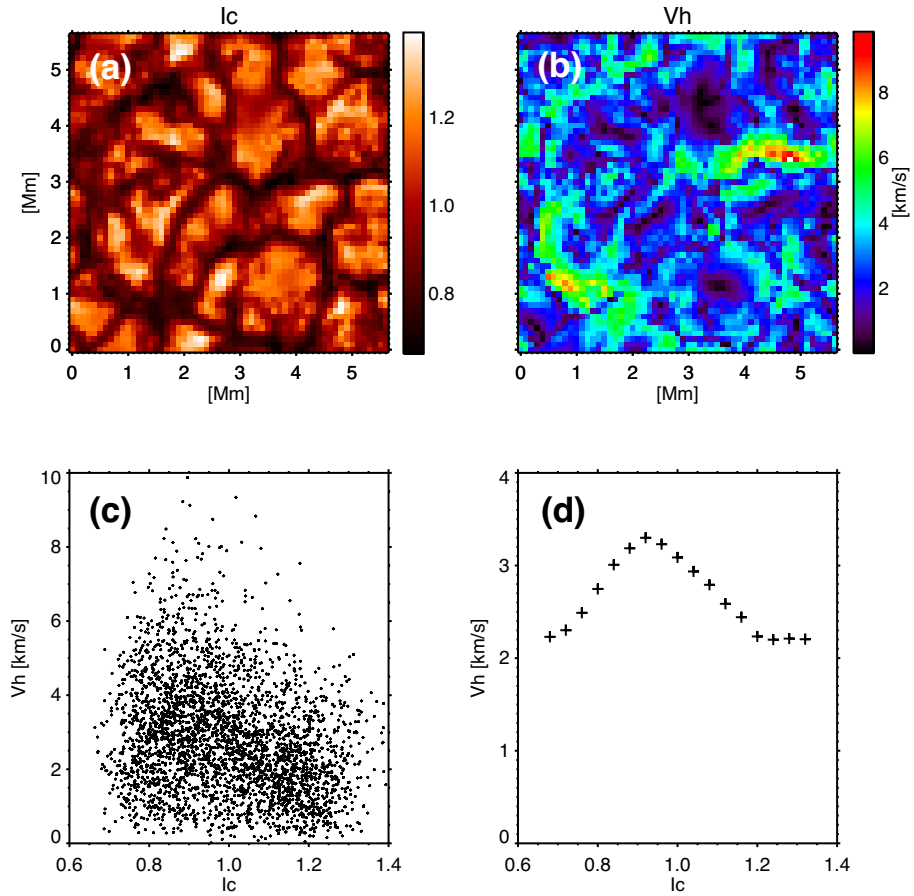
Figure 5.3: Relation between the continuum intensity and horizontal velocity fields in the numerical simulation. Panel (a): Snapshot of the continuum intensity calculated by the SPINOR code. Panel (b): Corresponding snapshot of the horizontal velocity fields, defined as $\sqrt{v_x^2 + v_y^2}$, at a geometrical height of 62 km. Panel (c): Scatter plot between the continuum intensity and horizontal velocity field. Panel (d): Horizontal flow speeds in RMS segmented with a spacing of I_c=0.04.
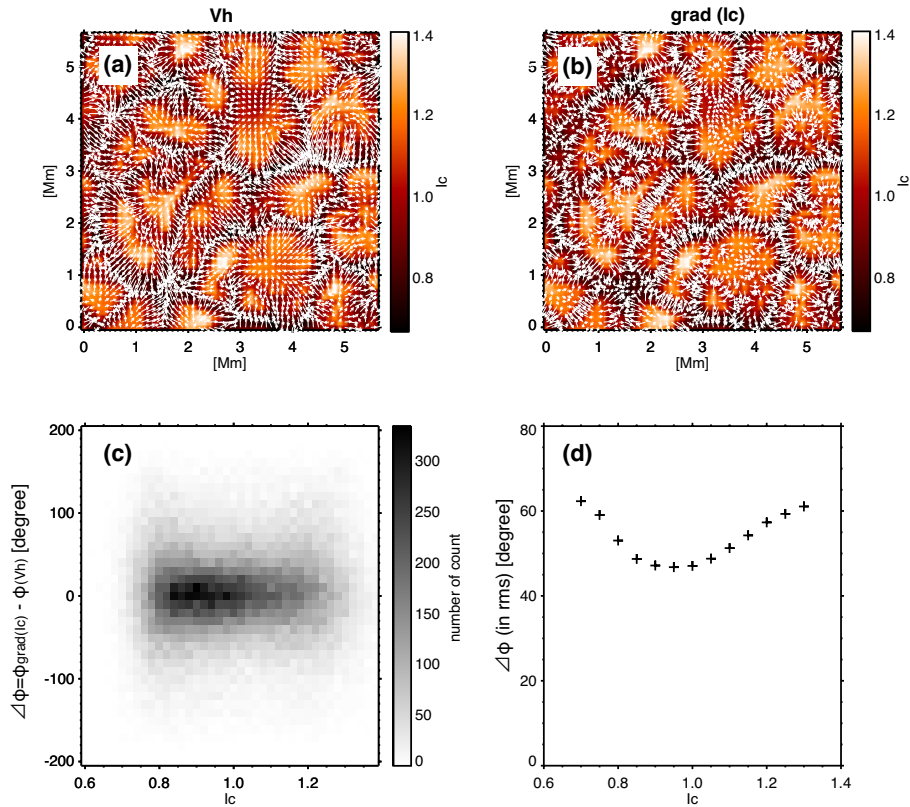
Figure 5.4: Panel (a): Snapshot of the continuum intensity (I_c) with horizontal flow vector (v_h) overploted in white arrow. Panel (b): Same snapshot and its gradient direction, $grad(I_c)$. Panel (c): Scatter plot of the continuum intensity (I_c) versus the deviation directions between those two vectors (see the text for details). Panel (d): The deviation $\Delta\phi$ in RMS as a function of the continuum intensity I_c, segmented with a spacing of I_c=0.05.

the requirement in all the preexisting coronal heating models (to the best of the author's knowledge). Suzuki & Inutsuka (2006) surveyed a temperature response of the corona by adopting different amplitudes of horizontal flow into the boundary condition. If we adopt our amplitude (1.9 km/s) into their model, the coronal temperature results in a few millions degree and the solar wind mass flux becomes roughly one hundred times as larger as the observed value.

While the above discussion focuses only the flow amplitude, it should be noted here the importance of the time evolution of the granulation. The efficiency of the wave dissipation critically depends on perturbation frequency of the photospheric buffeting motion. Antolin et al. (2008) found that the heating model with a photospheric perturbation at the particular temporal frequency cannot maintain the coronal temperature through the effective waves's non-linear dissipation or wave cutoff, even incorporating amplitude of more than 1 km/s. While the most favorable frequency range is around 100-300 sec, the power spectrum observed with a feature tracking technique has more concentration on this frequency than the randomly white noise (Matsumoto & Shibata 2010). Our derivation is merely average flow amplitude, totally lacking of the temporal power spectrum. On the other hand, this study implies that any temporal power distribution should satisfy 1.9 km/s in the integrated power. Our future interest is to derive the temporal power spectrum with a Doppler diagnostic.

Regarding the spatial distribution of the horizontal flow, our finding of its maximum speed occurring in intergranular lanes lead to an important implication that MHD waves should be vigorously driven in intergranular lanes. Although magnetic flux tubes have been well-known to be preferably located in intergranular lanes (Title et al. 1987), the spatial distribution of the lateral flows remains unknown. The retrieved spatial distribution confirms that the lateral flows surrounding magnetic flux tube can inject their kinetic energy efficiently. Next important work is a determination of which MHD waves are likely to driven, as categorized into *torsional, kink*, and *sausage* types. The incom-

pressible waves (torsional and kink types) are a good candidate for the coronal heating because these waves are immune to dissipation even at a highly steep density gradient from the chromosphere to the corona (Jess & Verth 2016). The compressible wave (sausage type) dissipates at the chromosphere because this wave is likely to be reflected by the strong atmospheric stratification. Which MHD wave is driven is determined by different flow patterns, such as rotation, shear, and convergent motions surrounding magnetic flux tubes. Turbulent and swirling flows similar to those flow patterns were detected with a feature tracking technique (Bonet et al. 2008; Manso Sainz et al. 2011). To identify which flow pattern actually drives the MHD waves, our future interest is on the time evolution of the photospheric lateral flows and their effect on magnetic flux tube. However, this analysis requires even higher spatial resolution. In the current observational instrument, the maximum access to the limb with the well-resolved Doppler signals is μ=0.6, where the observed LOS component still dominantly reflects the vertical flow. Higher spatial resolution can relax the foreshortening degradation, thereby allowing a farther limb exploration e.g., μ<0.5, so that the LOS component reflects dominantly horizontal flow. This LOS component with a majority of the horizontal flow signal included enables to analyze their time evolution, because we need not rely on the average derivation such as our current study.

This study would be realized by the future solar observatories with a huge aperture, e.g., 4-meter diameter's one attached to ground-based telescope in DKIST (Elmore et al. 2014) and EST (Collados et al. 2013). In the forthcoming era, the balloon-borne solar observatory SUNRISE (Solanki et al. 2010, 2017; Barthol et al. 2011) equipped with the 1-meter aperture telescope (two times lager than *Hinode*) is scheduled to be launched in 2021 (Solanki 2017). This ballon is planning to fly at 35 km above the sea level, and thus this instrument will not suffer from a main concern of the atmospheric seeing degradation. Installed to the SUNRISE balloon, a Japan-led spectropolarimeter aims to observe two optimized bands (770 nm and 850 nm) so that more than ten spectral lines

Table 5.2: Required amplitude as a boundary condition of the preexisting heating models

Paper	Required amplitude	Time
Kudoh & Shibata (1999)	1.0 km/s	randomly white noise
Moriyasu et al. (2004)	1.0 km/s	randomly white noise
Suzuki & Inutsuka (2006)	0.7 km/s	randomly white noise
Antolin et al. (2008)	1.3 km/s	randomly white noise
van Ballegooijen et al. (2011)	1.5 km/s	60-200 sec
Asgari-Targhi & van Ballegooijen (2012)	1.5 km/s	60 sec
Woolsey & Cranmer (2015)	1.5 km/s	60 sec

covers seamlessly from the photosphere to the chromosphere ($\approx$1,000 km) (Quintero Noda et al. 2017a,b), highly exceeding our current height extent (50-150 km). This instrument therefore would achieve approximately two times higher spatial resolution than that of *Hinode*/SP, hopefully allowing the farther limb exploration (μ<0.5) with a combination of our deconvolution process. Besides, the instrument adds totally new physical information, namely the chromospheric response, e.g., temperature, and LOS velocity fields, and magnetic field, which is a great advance in revealing the connection between the photospheric driver and its energy dissipation in the upper layer with a seamless height-extent observation.

Chapter 6

Summary and future prospects

6.1 Summary of our study

We have studied the solar photospheric convection, on the basis of spectral data observed by the *Hinode* spacecraft. The scattered light contamination due to the instrumental imaging performance was removed by the deconvolution processing. To avoid a general risk of noise enhancement in deconvolution processing, we newly incorporated a regularization term into the algorithm of the conventional deconvolution. We drew the following results regarding the vertical flows:

- The convective velocity amplitude ranges from approximately -3.0 km/s (upflow) to +3.0 km/s (downflow) after deconvolution, while from -2.0 km/s to +1.5 km/s before it.

- Whereas the raw data derived without deconvolution shows a global upflow (i.e., net LOS velocity averaged over the entire FOV pixels) of up to -0.2 km/s, this value derived with deconvolution drops to within ±0.05 km/s.

- The deconvolution also changes the spatial distribution of the velocity field, such that the upflowing area at the granular edges is trimmed by downflows pertaining

to the intergranular lanes.

- The observed LOS velocities in both cases with/without deconvolution match well those derived from the numerical simulation, in which bisector analysis is applied to the synthesized spectral profiles with/without convolution with the *Hinode*'s PSF.

The above results indicate that the downflows are preferentially increased by deconvolution, while the upflows are moderately enhanced. Thus, the spatial deconvolution allows us to investigate details of the convective dynamics, e.g., narrow intergranular lanes, precluded in the instrumentally blurred images. The agreement with MHD simulations suggests that the current simulations provide a relatively good description of the solar granulation. To sum up, our deconvolution processing successfully corrects for the spatial degradation by the instrumental imaging performance, and considerably reconciles the discrepancies between observation and numerical simulation.

We drew the following results about the horizontal flows:

- The LOS amplitude in RMS monotonically increases from 0.9 km/s at μ=1.0 to 1.5 km/s at μ=0.6.

- The estimated horizontal amplitude including granules and intergranular lanes is 1.6-1.9 km/s.

That LOS amplitude reaches the highest value ever reported before, achieving almost two times larger than the past works. The amplitude of the horizontal flows is strong enough to maintain the typical coronal temperature for all the preexisting coronal heating models (to the best of the author's knowledge).

Finally, combining vertical and horizontal flow amplitudes into the three-dimensional convective model, we drew the following results:

- The granulation generally represents a radial divergent flow from a granular center, and some part of the flow streams along the azimuthal direction.

- The horizontal flow reaches the maximum speed in intergranular lane side, near the boundary between granule and intergranular lane.

It is the first time with a Doppler calculation to directly describe the three-dimensional convective flows. This depiction indicates that the horizontal flow accelerates from granule and reaches the maximum speed in intergranular side, while our conventional understanding considers intergranular lanes as simply downflowing region. This scenario is also supported by a fairly good agreement with a numerical simulation, in which the location of the maximum horizontal flow is also found in intergranular lane. It suggests that a vigorous dynamics happens in intergranular lanes, where buffeting motions affects magnetic flux tubes stronger than expected before.

6.2   Future prospects

Our scope of this study is limited to a derivation of the *average* three-dimensional convective velocity structure, but its application would be greatly helpful for astrophysical phenomena driven by the granulation. Here are lists for the future projects extending my current work:

Reversed granulation

This phenomena happens in the upper photospheric layer (geometrical height of 140 km: Ruiz Cobo et al. 1996; Wedemeyer et al. 2004), which is one of the mysterious phenomena. The *reverse* is named after an opposite intensity distribution, i.e., *bright* intergranular lanes and *dark* granules. The gas temperature in the upper intergranuar lanes increases as if unknown energy injection mechanism overcomes a radiative energy loss. Several physical processes could explain this phenomenon, e.g., gas compression, p-mode oscillations, and radiative reheating (Rutten et al. 2004). Our limb observation

could identify the cause of the reversed granulation by recording spatially well-resolved flows surrounding the bright intergranular lane, and both sides of the lanes would be an indication of the gas compression. The schematic view of this approach is described in Fig.6.1 (a), where the region of interest corresponds to the bright intergranuar lane. Our bisector analysis would cover enough height-range, since it reaches up to 135 km, which is almost identical to the height where the reversed granulation starts. One of the future works is to discriminate those possible causes of this phenomenon, by either supporting the gas compressional cause or removing out it.

Supersonic flows

Historically, many turbulent signals have been noticed (Nesis et al. 1993; Rybák et al. 2004), seen as an extensively broaden line profile in the limb observations. At present, *Hinode*'s spectral data only can resolve this broaden profile into two distinctive lines, one of which has a typical Doppler shift of a few km/s, and the other largely departs from the usual wavelength and even reaches (or exceeds) the photospheric sound speed (≈ 7 km/s) (Bellot Rubio 2009; Quintero Noda et al. 2016). This extremely high speed signal is also recorded in the LOS flow fields in our limb observations. However, a mechanism to intermittently generate the supersonic flows still remains unidentified. In my opinion, the supersonic flows may be linked to the most dynamic phenomena of the granulation, i.e., *exploding granule*, which is a transient granular disintegration into 2-5 pieces of fragment. In comparison to the past works, our approach has several observational advantages by attaining high spatial resolution with the deconvolution and fairly high temporal resolution (≈ 1 min) enough to follow their exploding sequence. Our future work is to clarify this possible cause of the supersonic flows.

Magneto-convection

This interactive action has been thought to drive lots of physical phenomena in the photo-

sphere, and extensively even in the upper layers (e.g., the chromosphere and the corona). To know these layers' connectivity, the time evolution of the interaction between magnetic and kinetic energy is a topic of vigorous debate. One of the important works is to determine the MHD wave mode as wave's different restring force (through a compressible or incompressible process) leads to a different heating regime, as explained in section 5.2. Compressible waves are thought to be driven in photospheric compressible motions (Kato et al. 2011), and incompressible ones are triggered by sheer or rotational flows (Vögler et al. 2005), while there is another possibility for an independence of the photospheric flows because of mode conversions from compressible to incompressible one and vice versa in the upper layers (Khomenko & Cally 2012). A feature tracking technique detected the rotational motions in intergranular lanes, which behaves like *sink* that makes gas and magnetic field rotate with their submerging movements (Bonet et al. 2008; Requerey et al. 2017). However, Morton et al. (2013) reported different time evolution between these rotational motions in the photosphere and the chromospheric response. Removing out the uncertainty with a tracking technique in such a tiny spatial scale phenomena, our approach with Doppler signals would confirm such a rotational (and compressional) motions near magnetic field. A schematic view of this approach is described in Fig.6.1 (a) and (b), where the region of interest corresponds to the magnetic flux tube. Therefore, we can directly extend our current investigation of velocity fields with co-spatial magnetic field strength and its orientation simultaneously acquired by the *Hinode*/SP, serving to determine which MHD wave mode is likely to be driven.

Stellar physics

At present, the stellar physics field has an observational consensus viewpoint that spatially averaged line profile generally forms *C-shape* in late-type star's bisectors (Gray 2008), while the tiny shapes differ from each other. This might be true as long as the stellar photosphere maintains the general granulation, in which blue-shifted profiles in granules
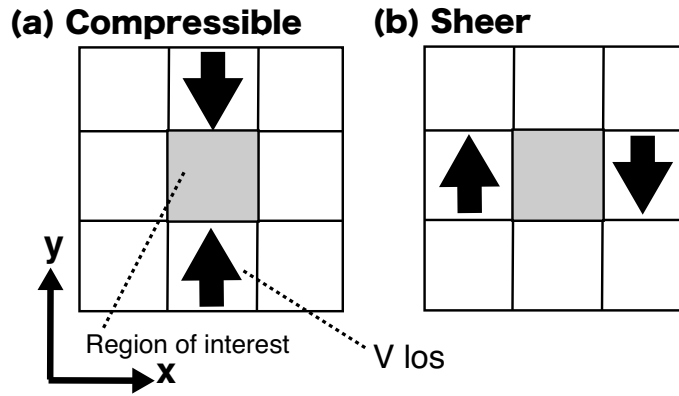
Figure 6.1: Schematic views of the observation at near the North or South pole. (a) compressive indicator: the difference of the LOS velocity fields between the northern and southern pixels against the region of interest (in grey color). (b) sheer indicator: the difference between the eastern and western pixels against the region of interest.

and red-shifted ones in intergranular lanes. The solar photospheric lines also represent C-shape (Dravins et al. 1981), and hence the solar photosphere would be a good indication of how to form C-shape, and hopefully extracting information of the stellar granulation. In spatially but moderately resolved line profiles in granules and intergranular lanes, their bisectors represent typically C-shape and /-*shape*, respectively (Hanslmeier et al. 2000; Maltagliati & Righini 2003), which was confirmed to be the same results as *Hinode*'s observations by our quick look. In a conventional interpretation, the major contribution of granular profiles originally having C-shape retains the shape even in the averaged profile, while the other contribution of intergranular /-shape hardly affects them. However, we have confirmed that the deconvolution drastically changes granular bisector from C-shape to \-*shape*, which is not shown because it is beyond our scope of the current study. Hence, we propose that the formation of C-shape results from an indispensable contribution of intergranular line profiles. More careful investigation is to estimate the solar limb contribution having a different bisector shape (Brandt & Schroeter 1982), since the mean line profile integrates over the whole solar surface.

Appendix A

Numerical simulation

Here we describe the numerical simulation code used in this study, which significantly contributes to the test calculation for the newly developed RL algorithm in a regularized form and many of comparisons with the observations. While several solar atmospheric synthesis codes have been developed as described in section 1.3, the employed MURaM code (Vögler et al. 2005) is highly sophisticated to reproduce a photospheric convection with a high spatial sampling, e.g., it achieved the finest spatial sampling of 2 km, which has never been performed before (Rempel 2014). The chosen setup was the same as that used in Riethmüller et al. (2014). The calculation ran for 1 hour of solar time and we stored a snapshot containing the physical parameters needed for the spectrum computation every 30 seconds, thus producing 120 snapshots. Each snapshot had a size of 6 × 6 Mm with a spatial sampling in the horizontal directions of 10.42 km. The vertical extension of the simulation box was 1.4 Mm and its grid size was constant at 14 km. The average height where the continuum optical depth (τ_{500}) is unity was at 0.5 Mm below the top boundary of the computational box. The simulation was performed without any initial magnetic flux, and therefore, we focused only on the pure hydrodynamics in the photosphere.

To synthesize the spectral profiles for the computational atmospheric box, several types of calculation codes that solve radiative energy transfer have been developed (Ruiz Cobo
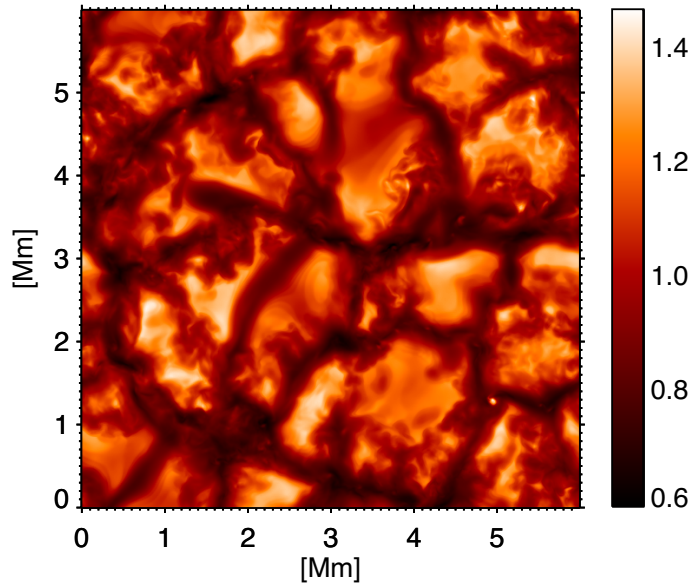
Figure A.1: One snapshot of the emergent continuum intensity map for the numerical simulation.

& del Toro Iniesta 1992; Frutiger et al. 2000; Socas-Navarro et al. 2015; Riethmüller et al. 2017). We employed the SPINOR code (Frutiger et al. 2000) to produce a series of snapshots taken from a radiative MHD simulation generated by the MURaM code, in which the LTE assumed for saving computational cost is mostly satisfied in the photosphere. Figure A.1 shows an example of the spatial distribution of the intensity signals at the continuum wavelength $\lambda = 630.1$ nm for a selected snapshot. Several authors confirmed that the intensity contrast of snapshots created with a combination of the MURaM and SPINOR codes fairly matches *Hinode*'s observation, when applied with *Hinode*'s spatial degradation (Danilovic et al. 2008; Afram et al. 2011). Our granulation has a non-magnetic bright point located at [4.9, 1.3] Mm frequently reproduced in recent numerical simulations, which is also a good indication of fairness in theoretical point of view (Calvo et al. 2016).

Appendix B

Contrast of the granulation

We may need to confirm whether the continuum intensity contrast after the deconvolution is realistic, avoiding an excess iteration in the deconvolution algorithm. This process would be achieved by comparing our contrast with the results obtained using the hydrodynamic simulation. The continuum contrast of *Hinode*/SP is 7.2% without deconvolution and 13.0 % with it. The contrast of the numerically synthesized image in the original pixel sampling ($\approx$10 km), the summed sampling ($\approx$100 km), and the summed sampling after the convolution with the instrument's PSF shows 16.8%, 16.1%, and 8.2%, respectively. The third one (8.2%) is similar to the one observed by our *Hinode*/SP, i.e., 7.2%, although the *Hinode* value is somewhat lower. The contrast value of 13.0% in the deconvolved observation is lower than 16.1% in the original simulation. This suggests that the image would be not over-restored, so that the deconvolution provided a realistic image in terms of the contrast. Moreover, these values are consistent with the previous work in Danilovic et al. (2008), who found RMS contrasts of 14.4%, 7.5%, and 7.0% in the original pixel sampling ($\approx$10 km), the summed sampling ($\approx$100 km) with spatial convolution, and the *Hinode*/SP observation used in their work, respectively.

Their contrast values (14.4% and 7.5%) are slightly lower than ours (16.8% and 8.2%) because their simulation included magnetic flux, which hinders the granulation and, hence, reduces the intensity contrast (Biermann 1941; Riethmüller et al. 2014). The contrast of

13.0% found in our work is also consistent with the value of 12.8% estimated by the observational approach in Mathew et al. (2009), who derived the PSF of the *Hinode*/SOT using the images during the Mercury transit, and deconvolved them. Thus, our deocnvolution technique does not produce an over-restored data because ours are fairly in compatible with the past works.

Bibliography

Abramenko, V. I., Yurchyshyn, V. B., Goode, P. R., Kitiashvili, I. N., & Kosovichev, A. G. 2012, ApJ, 756, L27

Afram, N., Unruh, Y. C., Solanki, S. K., et al. 2011, A&A, 526, A120

Allende Prieto, C., & Garcia Lopez, R. J. 1998, A&AS, 131, 431

Antolin, P., Shibata, K., Kudoh, T., Shiota, D., & Brooks, D. 2008, ApJ, 688, 669

Asgari-Targhi, M., & van Ballegooijen, A. A. 2012, ApJ, 746, 81

Asplund, M., Nordlund, Å., Trampedach, R., Allende Prieto, C., & Stein, R. F. 2000, A&A, 359, 729

Balthasar, H. 1985, Sol. Phys., 99, 31

Baran, O. A., & Stodilka, M. I. 2010, Kinematics and Physics of Celestial Bodies, 26, 117

Barthol, P., Gandorfer, A., Solanki, S. K., et al. 2011, Sol. Phys., 268, 1

Beckers, J. M., & Nelson, G. D. 1978, Sol. Phys., 58, 243

Beeck, B., Cameron, R. H., Reiners, A., & Schüssler, M. 2013, A&A, 558, A49

Beeck, B., Collet, R., Steffen, M., et al. 2012, A&A, 539, A121

Bello González, N., Franz, M., Martínez Pillet, V., et al. 2010, ApJ, 723, L134

Bellot Rubio, L. R. 2009, ApJ, 700, 284

Bellot Rubio, L. R., Rodríguez Hidalgo, I., Collados, M., Khomenko, E., & Ruiz Cobo, B. 2001, ApJ, 560, 1010

Bellot Rubio, L. R., Ruiz Cobo, B., & Collados, M. 1999, A&A, 341, L31

Berger, T. E., Löfdahl, M. G., Shine, R. S., & Title, A. M. 1998, ApJ, 495, 973

Berrilli, F., Florio, A., Consolini, G., et al. 1999, in ESA Special Publication, Vol. 448, Magnetic Fields and Solar Processes, ed. A. Wilson & et al., 229

Biermann, L. 1941, Vierteljahresschrift der Astronomischen Gesellschaft, 76, 194

Bonet, J. A., Márquez, I., Sánchez Almeida, J., Cabello, I., & Domingo, V. 2008, ApJ, 687, L131

Borrero, J. M., & Bellot Rubio, L. R. 2002, A&A, 385, 1056

Brandt, P. N., Scharmer, G. B., Ferguson, S., Shine, R. A., & Tarbell, T. D. 1988, Nature, 335, 238

Brandt, P. N., & Schroeter, E. H. 1982, Sol. Phys., 79, 3

Bray, R. J., Loughhead, R. E., & Durrant, C. J. 2009, The Solar Granulation (Cambridge: Cambridge Univ. Press)

Buehler, D., Lagg, A., Solanki, S. K., & van Noort, M. 2015, A&A, 576, A27

Calvo, F., Steiner, O., & Freytag, B. 2016, A&A, 596, A43

Cheung, M. C. M., Schüssler, M., & Moreno-Insertis, F. 2007, A&A, 461, 1163

Chitta, L. P., van Ballegooijen, A. A., Rouppe van der Voort, L., DeLuca, E. E., & Kariyappa, R. 2012, ApJ, 752, 48

Collados, M., Bettonvil, F., Cavaller, L., et al. 2013, Mem. Soc. Astron. Italiana, 84, 379

Culhane, J. L., Harra, L. K., James, A. M., et al. 2007, Sol. Phys., 243, 19

Danilovic, S., Gandorfer, A., Lagg, A., et al. 2008, A&A, 484, L17

Danilovic, S., Schüssler, M., & Solanki, S. K. 2010, A&A, 509, A76

Danilovic, S., van Noort, M., & Rempel, M. 2016, A&A, 593, A93

De Pontieu, B., McIntosh, S. W., Carlsson, M., et al. 2007, Science, 318, 1574

Del Moro, D. 2004, A&A, 428, 1007

Deubner, F.-L. 1974, Sol. Phys., 39, 31

Dey, N., Blanc-Féraud, L., Zimmer, C., et al. 2004, 3D Microscopy Deconvolution using Richardson-Lucy Algorithm with Total Variation Regularization, Research Report 5272, INRIA, France

Dialetis, D., Macris, C., Prokakis, T., & Sarris, E. 1986, A&A, 168, 330

Domínguez Cerdeña, I., Sánchez Almeida, J., & Kneer, F. 2003, A&A, 407, 741

Dravins, D., Lindegren, L., & Nordlund, A. 1981, A&A, 96, 345

Elmore, D. F., Rimmele, T., Casini, R., et al. 2014, in Proc. SPIE, Vol. 9147, Ground-based and Airborne Instrumentation for Astronomy V, 914707

Fischer, C. E., de Wijn, A. G., Centeno, R., Lites, B. W., & Keller, C. U. 2009, A&A, 504, 583

Freytag, B., Steffen, M., & Dorch, B. 2002, Astronomische Nachrichten, 323, 213

Frutiger, C. 2000, Ph.D. Thesis, Institute of Astronomy, ETH Zürich

Frutiger, C., Solanki, S. K., Fligge, M., & Bruls, J. H. M. J. 2000, A&A, 358, 1109

Fujimura, D., & Tsuneta, S. 2009, ApJ, 702, 1443

Gadun, A. S., Hanslmeier, A., Pikalov, K. N., et al. 2000, A&AS, 146, 267

Galsgaard, K., & Nordlund, Å. 1996, J. Geophys. Res., 101, 13445

Golub, L., Deluca, E., Austin, G., et al. 2007, Sol. Phys., 243, 63

Gray, D. F. 2008, The Observation and Analysis of Stellar Photospheres (Cambridge
    University Press)

Grossmann-Doerth, U., Schuessler, M., & Solanki, S. K. 1988, A&A, 206, L37

Gudiksen, B. V., Carlsson, M., Hansteen, V. H., et al. 2011, A&A, 531, A154

Hanslmeier, A., Kučera, A., Rybák, J., Neunteufel, B., & Wöhl, H. 2000, A&A, 356, 308

Hathaway, D. H., Beck, J. G., Han, S., & Raymond, J. 2002, Sol. Phys., 205, 25

Hirzberger, J. 2002, A&A, 392, 1105

Hirzberger, J., Bonet, J. A., Vázquez, M., & Hanslmeier, A. 1999a, ApJ, 515, 441

—. 1999b, ApJ, 527, 405

Hirzberger, J., Vázquez, M., Bonet, J. A., Hanslmeier, A., & Sobotka, M. 1997, ApJ, 480,
    406

Hurlburt, N. E., Toomre, J., & Massaguer, J. M. 1984, ApJ, 282, 557

Ichimoto, K., Hiei, E., & Nakagomi, Y. 1989, PASJ, 41, 333

Ichimoto, K., Lites, B., Elmore, D., et al. 2008, Sol. Phys., 249, 233

Isobe, H., Proctor, M. R. E., & Weiss, N. O. 2008, ApJ, 679, L57

Janssen, K., & Cauzzi, G. 2006, A&A, 450, 365

Jansson, P. A. 1997, Deconvolution of images and spectra. (Dover Publications, Inc., United States)

Jess, D., & Verth, G. 2016, Ultra-High-Resolution Observations of MHD Waves in Photospheric Magnetic Structures, ed. A. Keiling, D.-H. Lee, & V. Nakariakov, Geophysical Monograph Series (John Wiley & Sons, Inc.), 449–465

Jess, D. B., Mathioudakis, M., Erdélyi, R., et al. 2009, Science, 323, 1582

Jin, C., Wang, J., & Zhao, M. 2009, ApJ, 690, 279

Kato, Y., Steiner, O., Hansteen, V., et al. 2016, ApJ, 827, 7

Kato, Y., Steiner, O., Steffen, M., & Suematsu, Y. 2011, ApJL, 730, L24

Keil, S. L., & Canfield, R. C. 1978, A&A, 70, 169

Keys, P. H., Mathioudakis, M., Jess, D. B., et al. 2011, ApJ, 740, L40

Khomenko, E., & Cally, P. S. 2012, ApJ, 746, 68

Khomenko, E., Martínez Pillet, V., Solanki, S. K., et al. 2010, ApJ, 723, L159

Khomenko, E. V., Kostik, R. I., & Shchukina, N. G. 2001, A&A, 369, 660

Kostik, R., Khomenko, E., & Shchukina, N. 2009, A&A, 506, 1405

Kostik, R. I., & Khomenko, E. V. 2007, A&A, 476, 341

Kosugi, T., Matsuzaki, K., Sakao, T., et al. 2007, Sol. Phys., 243, 3

Kudoh, T., & Shibata, K. 1999, ApJ, 514, 493

Leenaarts, J., & Wedemeyer-Böhm, S. 2005, A&A, 431, 687

Leighton, R. B., Noyes, R. W., & Simon, G. W. 1962, ApJ, 135, 474

Lemmerer, B., Hanslmeier, A., Muthsam, H., & Piantschitsch, I. 2017, A&A, 598, A126

Lemmerer, B., Utz, D., Hanslmeier, A., et al. 2014, A&A, 563, A107

Lites, B. W., & Ichimoto, K. 2013, Sol. Phys., 283, 601

Lites, B. W., Akin, D. L., Card, G., et al. 2013, Sol. Phys., 283, 579

Loève, M. M. 1955, Probability Theory (Princeton: Van Nostrand Company)

Louis, R. E., Ravindra, B., Georgoulis, M. K., & Küker, M. 2015, Sol. Phys., 290, 1135

Lucy, L. B. 1974, AJ, 79, 745

Magic, Z., Collet, R., Asplund, M., et al. 2013, A&A, 557, A26

Maltagliati, L., & Righini, A. 2003, memsai, 74, 599

Manso Sainz, R., Martínez González, M. J., & Asensio Ramos, A. 2011, A&A, 531, L9

Martínez Pillet, V., Del Toro Iniesta, J. C., Álvarez-Herrero, A., et al. 2011, Sol. Phys., 268, 57

Mathew, S. K., Zakharov, V., & Solanki, S. K. 2009, A&A, 501, L19

Matloch, Ł., Cameron, R., Shelyag, S., Schmitt, D., & Schüssler, M. 2010, A&A, 519, A52

Matsumoto, T., & Kitai, R. 2010, ApJ, 716, L19

Matsumoto, T., & Shibata, K. 2010, ApJ, 710, 1857

Mattig, W., Mehltretter, J. P., & Nesis, A. 1981, A&A, 96, 96

Mehltretter, J. P. 1978, A&A, 62, 311

Mihalas, D. 1978, Stellar atmospheres (2nd ed.; San Francisco, CA: W. H. Freeman and Co.)

Moriyasu, S., Kudoh, T., Yokoyama, T., & Shibata, K. 2004, ApJ, 601, L107

Morton, R. J., Verth, G., Fedun, V., Shelyag, S., & Erdélyi, R. 2013, ApJ, 768, 17

Müller, D. A. N., Steiner, O., Schlichenmaier, R., & Brandt, P. N. 2001, Sol. Phys., 203, 211

Muthsam, H. J., Kupka, F., Löw-Baselli, B., et al. 2010, New A, 15, 460

Nagata, S., Tsuneta, S., Suematsu, Y., et al. 2008, ApJ, 677, L145

Nesis, A., Hammer, R., Roth, M., & Schleicher, H. 2001, A&A, 373, 307

Nesis, A., Hanslmeier, A., Hammer, R., et al. 1993, A&A, 279, 599

Nesis, A., & Mattig, W. 1989, A&A, 221, 130

Nieminen, T. A. 2017, ArXiv e-prints, arXiv:1708.06408

Nordlund, Å., Stein, R. F., & Asplund, M. 2009, Living Reviews in Solar Physics, 6, doi:10.12942/lrsp-2009-2

November, L. J., & Simon, G. W. 1988, ApJ, 333, 427

Oba, T., Iida, Y., & Shimizu, T. 2017, ApJ, 836, 40

Okamoto, T. J., Tsuneta, S., Berger, T. E., et al. 2007, Science, 318, 1577

Parker, E. N. 1978, ApJ, 221, 368

Parnell, C. E., & De Moortel, I. 2012, Philosophical Transactions of the Royal Society of London Series A, 370, 3217

Poetzi, W., Hanslmeier, A., & Brandt, P. N. 2000, in ESA Special Publication, Vol. 463, The Solar Cycle and Terrestrial Climate, Solar and Space weather, ed. A. Wilson, 407

Puschmann, K., Vázquez, M., Bonet, J. A., Ruiz Cobo, B., & Hanslmeier, A. 2003, A&A, 408, 363

Quintero Noda, C., Asensio Ramos, A., Orozco Suárez, D., & Ruiz Cobo, B. 2015, A&A, 579, A3

Quintero Noda, C., Shimizu, T., & Suematsu, Y. 2016, MNRAS, 457, 1703

Quintero Noda, C., Shimizu, T., Katsukawa, Y., et al. 2017a, MNRAS, 464, 4534

Quintero Noda, C., Uitenbroek, H., Katsukawa, Y., et al. 2017b, MNRAS, 470, 1453

Ramírez, I., Allende Prieto, C., Koesterke, L., Lambert, D. L., & Asplund, M. 2009, A&A, 501, 1087

Rast, M. P. 1995, ApJ, 443, 863

Rast, M. P., Ortiz, A., & Meisner, R. W. 2008, ApJ, 673, 1209

Rempel, M. 2014, ApJ, 789, 132

Rempel, M., Schüssler, M., & Knölker, M. 2009, ApJ, 691, 640

Requerey, I. S., Del Toro Iniesta, J. C., Bellot Rubio, L. R., et al. 2014, ApJ, 789, 6

—. 2017, ApJS, 229, 14

Richardson, W. H. 1972, Journal of the Optical Society of America (1917-1983), 62, 55

Riethmüller, T. L., Solanki, S. K., Berdyugina, S. V., et al. 2014, A&A, 568, A13

Riethmüller, T. L., Solanki, S. K., van Noort, M., & Tiwari, S. K. 2013, A&A, 554, A53

Riethmüller, T. L., Solanki, S. K., Barthol, P., et al. 2017, ApJS, 229, 16

Rieutord, M., & Rincon, F. 2010, Living Reviews in Solar Physics, 7, 2

Rieutord, M., Roudier, T., Ludwig, H.-G., Nordlund, Å., & Stein, R. 2001, A&A, 377, L14

Rieutord, M., Roudier, T., Malherbe, J. M., & Rincon, F. 2000, A&A, 357, 1063

Rimmele, T. R. 2000, in Proc. SPIE, Vol. 4007, Adaptive Optical Systems Technology, ed. P. L. Wizinowich, 218–231

Ruiz Cobo, B., & Asensio Ramos, A. 2013, A&A, 549, L4

Ruiz Cobo, B., & del Toro Iniesta, J. C. 1992, ApJ, 398, 375

Ruiz Cobo, B., del Toro Iniesta, J. C., Rodriguez Hidalgo, I., Collados, M., & Sanchez Almeida, J. 1996, in Astronomical Society of the Pacific Conference Series, Vol. 109, Cool Stars, Stellar Systems, and the Sun, ed. R. Pallavicini & A. K. Dupree, 155

Rutten, R. J., de Wijn, A. G., & Sütterlin, P. 2004, A&A, 416, 333

Rutten, R. J., & Krijger, J. M. 2003, A&A, 407, 735

Rybák, J., Wöhl, H., Kučera, A., Hanslmeier, A., & Steiner, O. 2004, A&A, 420, 1141

Schroeder, D. J., ed. 2000, Astronomical optics

Schwarzschild, K. 1906, Nachrichten von der Königlichen Gesellschaft der Wissenschaften zu Göttingen. Math.-phys. Klasse, 195, p. 41-53, 195, 41

Shimizu, T., Nagata, S., Tsuneta, S., et al. 2008, Sol. Phys., 249, 221

Shine, R. A., Simon, G. W., & Hurlburt, N. E. 2000, Sol. Phys., 193, 313

Socas-Navarro, H., de la Cruz Rodríguez, J., Asensio Ramos, A., Trujillo Bueno, J., & Ruiz Cobo, B. 2015, A&A, 577, A7

Solanki, S. K. 1989, A&A, 224, 225

Solanki, S. K. 2017, in AAS/Solar Physics Division Meeting, Vol. 48, AAS/Solar Physics Division Meeting, 105.07

Solanki, S. K., Rueedi, I., Bianda, M., & Steffen, M. 1996, A&A, 308, 623

Solanki, S. K., Barthol, P., Danilovic, S., et al. 2010, ApJ, 723, L127

Solanki, S. K., Riethmüller, T. L., Barthol, P., et al. 2017, ApJS, 229, 2

Stangalini, M., Consolini, G., Berrilli, F., De Michelis, P., & Tozzi, R. 2014, A&A, 569, A102

Stein, R. F., & Nordlund, Å. 1998, ApJ, 499, 914

Steiner, O., Grossmann-Doerth, U., Knölker, M., & Schüssler, M. 1998, ApJ, 495, 468

Steiner, O., Franz, M., Bello González, N., et al. 2010, ApJ, 723, L180

Stix, M. 2004, The sun : an introduction (2nd ed., Astronomy and astrophysics library, Berlin: Springer)

Stix, M., & Wöhl, H. 1974, Sol. Phys., 37, 63

Suematsu, Y., Tsuneta, S., Ichimoto, K., et al. 2008, Sol. Phys., 249, 197

Suzuki, T. K., & Inutsuka, S.-I. 2006, Journal of Geophysical Research (Space Physics), 111, A06101

Title, A. M., Tarbell, T. D., Acton, L., Duncan, D., & Simon, G. W. 1986, Advances in Space Research, 6, 253

Title, A. M., Tarbell, T. D., & Topka, K. P. 1987, ApJ, 317, 892

Title, A. M., Tarbell, T. D., Topka, K. P., et al. 1989, ApJ, 336, 475

Tiwari, S. K., van Noort, M., Lagg, A., & Solanki, S. K. 2013, A&A, 557, A25

Tomczyk, S., McIntosh, S. W., Keil, S. L., et al. 2007, Science, 317, 1192

Tsuneta, S., Ichimoto, K., Katsukawa, Y., et al. 2008, Sol. Phys., 249, 167

Ulrich, R. K. 1970, ApJ, 162, 993

Unsöld, A. 1930, ZAp, 1, 138

van Ballegooijen, A. A., Asgari-Targhi, M., Cranmer, S. R., & DeLuca, E. E. 2011, ApJ, 736, 3

van Noort, M. 2012, A&A, 548, A5

van Noort, M., Lagg, A., Tiwari, S. K., & Solanki, S. K. 2013, A&A, 557, A24

van Noort, M., Rouppe van der Voort, L., & Löfdahl, M. G. 2005, Sol. Phys., 228, 191

Verma, M., & Denker, C. 2011, A&A, 529, A153

Verma, M., Steffen, M., & Denker, C. 2013, A&A, 555, A136

Vernazza, J. E., Avrett, E. H., & Loeser, R. 1981, ApJS, 45, 635

Vitas, N., Fischer, C. E., Vögler, A., & Keller, C. U. 2011, A&A, 532, A110

Vögler, A., Shelyag, S., Schüssler, M., et al. 2005, A&A, 429, 335

Wedemeyer, S., Freytag, B., Steffen, M., Ludwig, H.-G., & Holweger, H. 2004, A&A, 414, 1121

Wedemeyer-Böhm, S., & Rouppe van der Voort, L. 2009, A&A, 503, 225

Withbroe, G. L., & Noyes, R. W. 1977, ARA&A, 15, 363

Woolsey, L. N., & Cranmer, S. R. 2015, ApJ, 811, 136

Yelles Chaouche, L., Moreno-Insertis, F., & Bonet, J. A. 2014, A&A, 563, A93

Yu, D., Xie, Z., Hu, Q., Yang, S., & Jin, C. 2011a, Sol. Phys., 273, 1

Yu, D., Xie, Z., Hu, Q., et al. 2011b, ApJ, 743, 58